2007-03-19

Characterizing the Frictional Interface in Friction Stir Welding

Daryl A. Stratton
Brigham Young University - Provo

CHARACTERIZING THE FRICTIONAL INTERFACE IN FRICTION STIR WELDING

by

Daryl Alan Stratton

A thesis submitted to the faculty of

Brigham Young University

in partial fulfillment of the requirements for the degree of

Master of Science

Department of Mechanical Engineering

Brigham Young University

April 2007

BRIGHAM YOUNG UNIVERSITY

GRADUATE COMMITTEE APPROVAL

of a thesis submitted by

Daryl Alan Stratton

This thesis has been read by each member of the following graduate committee and by majority vote has been found to be satisfactory.

Date	Carl D. Sorensen, Chair
Date	Tracy W. Nelson
Date	Jonathan D. Blotter

BRIGHAM YOUNG UNIVERSITY

As chair of the candidate's graduate committee, I have read the thesis of Daryl Alan Stratton in its final form and have found that (1) its format, citations, and bibliographical style are consistent and acceptable and fulfill university and department style requirements; (2) its illustrative materials including figures, tables, and charts are in place; and (3) the final manuscript is satisfactory to the graduate committee and is ready for submission to the university library.

Date

Carl D. Sorensen
Chair, Graduate Committee

Accepted for the Department

Matthew R. Jones
Graduate Coordinator

Accepted for the College

Alan R. Parkinson
Dean, Ira A. Fulton College of Engineering and Technology

ABSTRACT

CHARACTERIZING THE FRICTIONAL INTERFACE IN FRICTION STIR WELDING

Daryl Alan Stratton

Department of Mechanical Engineering

Master of Science

Quantitative understanding of frictional phenomena between the tool and the workpiece is essential for accurate modeling of the Friction Stir Welding (FSW) process. Two methods of measuring the tool-workpiece interface are proposed that allow frictional measurements to be made under extreme conditions. The first method uses a cylindrically curved surface in contact with a flat plate. The ranges of temperature, velocity, and normal force used in this method are 100–600^{o}C, 0.38–2.0 m/s (75–400 surface feet per minute (SFM)), and 450–2700 N (100–600 lbf), respectively. Data are gathered at different parameter level combinations to provide enough data to create an empirical model representing the data. Two friction modes with distinct characteristics are observed. One mode, Coulomb-Amonton's friction, has frictional force proportional to normal force, while the other mode, plastic shear

deformation friction, has frictional force independent of normal force. A linear statistical model has been developed to characterize each of the frictional modes for the polycrystalline cubic boron nitride (PCBN) tool and 1018 steel work piece interface as functions of temperature, velocity, and normal force. Two linear models were chosen. A statistical method called membership function regression was used to determine the coefficients of these two models. The resulting model has a correlation of *(Predicted Force) = 1.0445(Measured Force)* with an R^2 value of 0.83.

The second method was an attempt to measure friction with a measurable contact area at a range of temperatures, velocities, and normal pressures. This method rubs the end of a cylindrical rod with a concentric cylindrical pocket against a flat plate. This method caused precessions of the tool on the workpiece. As a result of this precession, plastic shear deformation friction measurements are invalid. However, Coulomb-Amonton's friction is still valid. The experiments of the PCBN-stainless steel interface found that Coulomb-Amonton's friction did not depend on temperature and velocity. In addition, no plastic shear deformation friction was identified using this method and this interface combination.

ACKNOWLEDGMENTS

I would like to thank all of those who have been influential during this thesis: first, Carl Sorensen for guidance and direction; second, Tracy Nelson for making this work possible; third, Nathan Stephens and Dennis Eggett for their countless hours of support.

Financial support for this work was provided by the Office of Naval Research, contract No. N00014-05-1-0511, Dr. Julie Christodoulou, Program Manager.

Table of Contents

List of Tables

List of Figures

1 Introduction

Friction Stir Welding (FSW) is a solid-state joining process where a nonconsumable tool deforms two workpieces along the interface to form a union between the two workpieces. This welding process has gained popularity over the past decade due to the superior material properties it produces compared to traditional welding processes. The advantages of this process include the following: no filler material, no fumes, no solidification cracks, low porosity, low weld distortion, the ability to weld dissimilar metals, and greater strength and corrosion properties [1, 2].

The FSW process uses a tool that consists of a pin and a shoulder. The pin plunges into the seam between two workpieces until the shoulder reaches the workpiece surface. The tool dwells in place until sufficient heat is produced to traverse along the seam, between the workpieces. As the tool traverses along the seam a weld is produced. The weld is completed by extracting the tool from the workpiece. Figure 1.1 shows a schematic of the welding.

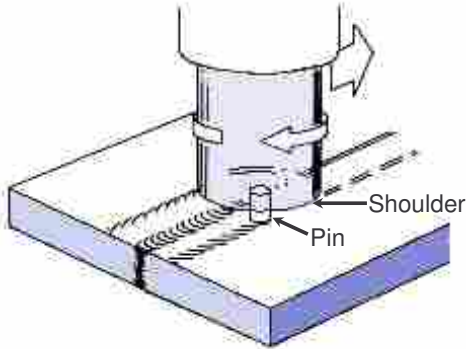

Figure 1.1: Friction stir welding schematic [3].

FSW was invented in 1991 by TWI (The Welding Institute). As such, this process is relatively young and our understanding of it is still developing.

1.1 FSW Analytical Models

In some situations analytical models of complex processes provide greater understanding than experimental measurement alone. If an accurate FSW model could be developed, it could be used to improve process understanding and to further process development. One important physical phenomenon, the frictional interface between the tool and the workpiece during FSW, has not been adequately characterized for implementation in an FSW model.

Current FSW models have either made simple assumptions about the frictional interface or neglected the interface all together. Khandkar et al. and many others [4] assumed a constant coefficient of friction. Seidel et al. [5] assumed there was zero relative velocity between the pin and the workpiece. Song et al. [6] recognized that the coefficient of friction could change during a friction stir weld, but they did not have data, so they assumed an effective coefficient of friction. Frigaard et al. [7] used an effective coefficient of friction that changed during the simulation. Only when the conditions for local melting were met did the algorithm reduce the coefficient of friction to keep the temperature from exceeding the melting temperature; all other times the effective coefficient of friction was held constant. Doug et al. and Chen et al. [8, 9] recognized that the coefficient of friction depended on temperature; however, they did not specify the friction model used.

1.2 Objectives

The objective of this research is to create develop methods of measuring the frictional interface between friction stir welding workpieces and tools. An additional objective is to develop an empirical model that could be implemented into a numerical model of the process.

1.3 About This Thesis

This thesis is a collection of three papers prepared for publication. The first paper uses a cylindrical surface against a flat plate method of measuring friction. In this frictional study friction statistical model is presented for the PCBN and 1018 steel interface. The second paper describes the development of statistical models and techniques to properly analyze the data. The third paper evaluates the use of a cylinder on plate method to study the frictional interface between PCBN and stainless steel. Finally, the thesis concludes by recommending future work.

2 Characterizing the Frictional Interface between PCBN and 1018 Steel in Friction Stir Welding

2.1 Abstract

Quantitative understanding of frictional phenomena between the tool and the workpiece is essential for accurate modeling of the Friction Stir Welding (FSW) process. A method of measuring the tool-workpiece interface is proposed that allows frictional measurements to be made in a non-oxidizing environment under extreme conditions. The ranges of temperature, velocity, and normal force are 100–600^{o}C, 0.38–2.0 m/s (75–400 surface feet per minute), and 450–2700 N (100–600 lbf) respectively. Data is gathered at different parameter level combinations to provide enough data to create an empirical model representing the data. Two friction modes with distinct characteristics are observed. One mode, Coulomb-Amonton's friction, has frictional force proportional to normal force, while the other mode, plastic shear deformation friction, has frictional force independent of normal force. A linear statistical model has been developed to characterize each of the frictional modes for the polycrystalline cubic boron nitride (PCBN) tool and 1018 steel workpiece interface as functions of temperature, velocity, and normal force. The model consists of two linear statistical models, one statistical model for each type of friction.

2.2 Introduction

Friction Stir Welding is a solid-state joining process where a non-consumable tool deforms two workpieces along the interface to form a union between the two work-

pieces. This welding process has gained popularity over the past decade. However, this process is relatively new and our understanding of it is insufficient.

Analytical models of complex processes provide greater understanding than experimental measurement alone. If an accurate FSW model could be developed, it could be used to improve process understanding and further process development. One important physical phenomenon, the frictional interface between the tool and the workpiece during FSW, has not been adequately characterized for implementation in an FSW model. Current FSW models have either made simple assumptions about the frictional interface or neglected the interface all together. Khandkar et al. and many others [4] assumed a constant coefficient of friction. Seidel et al. [5] assumed that there was zero relative velocity between the pin and the workpiece. Song et al. [6] recognized that the coefficient of friction could change during friction stir welding but did not have data, so they assumed an effective coefficient of friction. Frigaard et al. [7] used an effective coefficient of friction that changed during the simulation. Only when the conditions for local melting were met did the algorithm reduce the coefficient of friction to keep the temperature from exceeding the melting temperature; all other times the effective coefficient of friction was held constant. Doug et al. [8] and Chen et al. [9] recognized that the coefficient of friction depended on temperature; however, they did not specify the friction model used.

There is some work that has been done to explore the frictional interface over high normal loads. According to Shaw [10], at the sliding frictional interface, plastic regions form at asperity junctions. For Amonton's law to apply, only the asperities are plastically deformed. Amonton's law is shown in Figure 2.1 as region I. As loads increase, the plastic region also increases. When loads are high enough, plastic de-

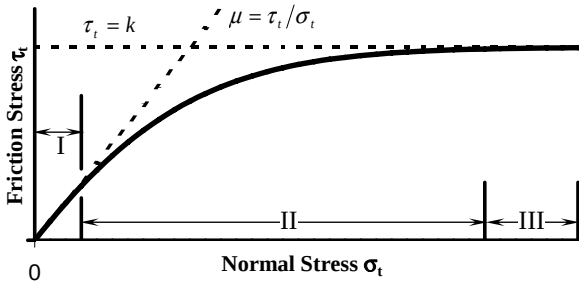

Figure 2.1: Schematic of the three friction regimes [11].

formation of the bulk material occurs. As the loads continue to increase, eventually the frictional force is defined completely by material properties. This is shown in figure 2.1 as region III. Three different friction regions are formed depending on the plasticity state. The two extreme regions are characterized by either Amonton's law or bulk material characteristics. The other friction region is a transition between these two opposing frictional characteristics. Figure 2.1 is a schematic representation of these three friction regimes.

Maekawa et al. [11] developed a frictional model for free-machining steels. This model preserved the characteristics of Amonton's law and the plateau defined by material characteristics. This model is shown in equation (2.1). The normal stress and friction shear stress are represented in equation (2.1) as σ_t and τ_t respectively where n' is a constant.

$$\tau_t = R \cdot k \cdot [1 - e^{\{-(\frac{\mu\sigma_t}{k})^{n'}\}}]^{\frac{1}{n'}}. \tag{2.1}$$

This model has three adjustable parameters: R, a proportional constant that relates the material to the reference material; μ, the coefficient of Coulomb-Amonton's friction; and k, the shear flow stress of the material.

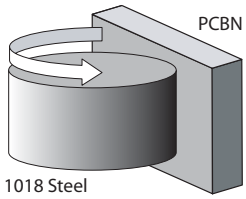

Figure 2.2. The type of frictional measurement for this experiment is a rotating cylinder on a stationary flat plate.

However, this friction model is insufficient for FSW modelling, because it does not include dependence on temperature or surface velocity, which may be significant factors determining frictional force.

The present paper describes the experimental investigation of the PCBN–1018 steel frictional interface for a range of temperatures, velocities, and normal forces. The experimental setup and procedure are described. In addition, significant variables and observations along with a statistical friction model are presented.

2.3 Experimental Procedure

The goal of this experiment is to measure frictional force data at a variety of temperatures, velocities, and normal forces. This is done by rotating a cylindrical steel tool such that the curved surface rubs against a flat PCBN surface. Figure 2.2 shows the type of frictional measurement performed in this study. While the cylindrical 1018 steel surface is rotating against the flat PCBN surface, the temperature of the interface, the frictional force, and the normal force are measured.

The experimental equipment used to measure the data consists of a three axis mill, a friction measuring mechanism, a force transducer, some thermocouples, A/D equipment, and a LabVIEW program.

A 1018 steel cylindrical tool, shown in Figure 2.3, was mounted in the spindle of the mill. The tool has a length of about 114 mm (4.5 inches). The portion of

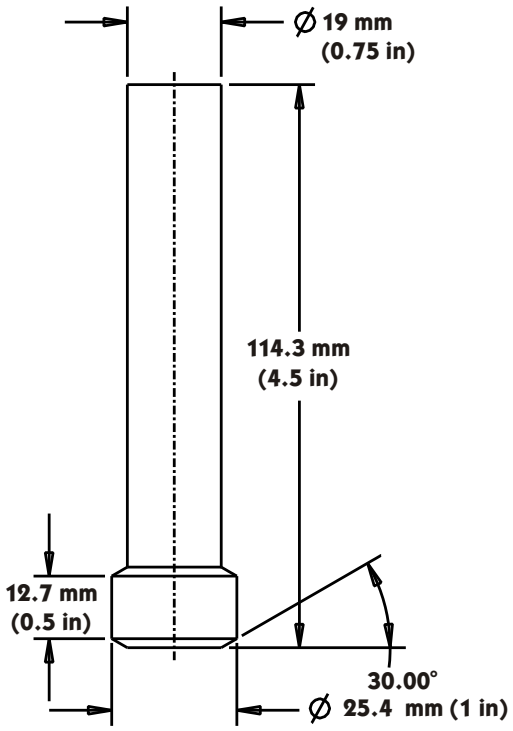

Figure 2.3: Drawing of the friction tool; tool made of 1018 steel.

the tool that contacts the PCBN is one inch in diameter by one-half inch in length. The PCBN MN100 grade blank is one inch in diameter.

The PCBN holder, Figure 2.4, is a stainless steel rectangular fixture where the PCBN is mounted flush to the the PCBN holder's surface. Thermocouples are located at the interface between the PCBN and the surface of the holder. These thermocouples are mounted such that there is good thermal contact with the PCBN. Figure 2.5 shows the mechanism used to measure friction. This mechanism allows the PCBN holder to move in the direction of the spring that is placed behind the PCBN holder in the friction mechanism. The friction mechanism is attached rigidly to a force transducer. This force transducer is capable of measuring forces in each of the Cartesian directions as well as moments about each of these axes. This force

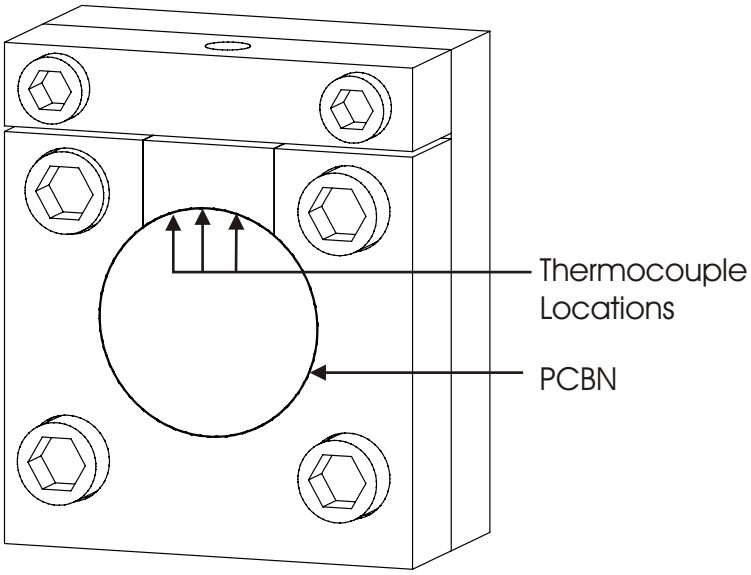

Figure 2.4: The PCBN holder.

transducer is mounted rigidly to the mill table. A plastic oven bag filled with argon surrounds the friction mechanism and PCBN holder such that the tool and the mechanism are enclosed.

This allows the effects of temperature, surface velocity, and normal force on friction to be studied. A typical run is conducted by setting the RPM of the machine and adjusting the normal force by displacing the PCBN blank against the rotating steel tool. Temperature, frictional force, and normal force are measured twice per second throughout an experimental run. For example, a run where a high temperature, low velocity, and low normal force conditions are desired, this experiment begins by setting the RPM on the machine to low. Initially, the tool is not in contact with the PCBN. Then, the mill table position is adjusted so that the tool exerts a force onto the PCBN. The spring behind the PCBN deflects producing a normal force. As the tool rotates in contact with the PCBN surface, frictional heating occurs. To raise the temperature, the normal force is increased beyond the

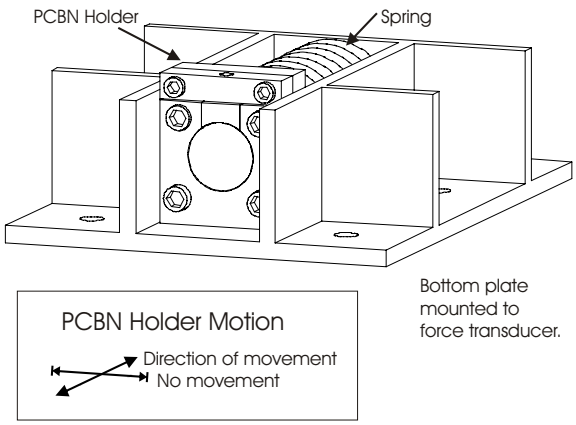

Figure 2.5: Friction mechanism.

desired normal force, which increases the heat generation rate and achieves a higher temperature. Once the temperature is achieved, the position of the table is backed off to reduce the normal force to the desired value. An example of the data gathered during a run is shown in Figure 2.6.

A full factorial experimental plan was made with two measurement levels for each of the three experimental variables. These variables and the associated levels are shown in Table 2.1. The standard order of the experimental runs is shown in Table 2.2. Each of these runs was performed twice, along with two center points, in random order for a total of eighteen initial runs. After analyzing data from these eighteen initial runs, ten additional runs were conducted to gather more information for model development and to repeat unexpected observations.

There is some difficulty in achieving each of these measurement levels, because experimental variables are measured and not controlled. The position of the table and the spindle RPM are the only parameters that can be controlled. These variables are not the variables of choice in modelling the frictional interface.

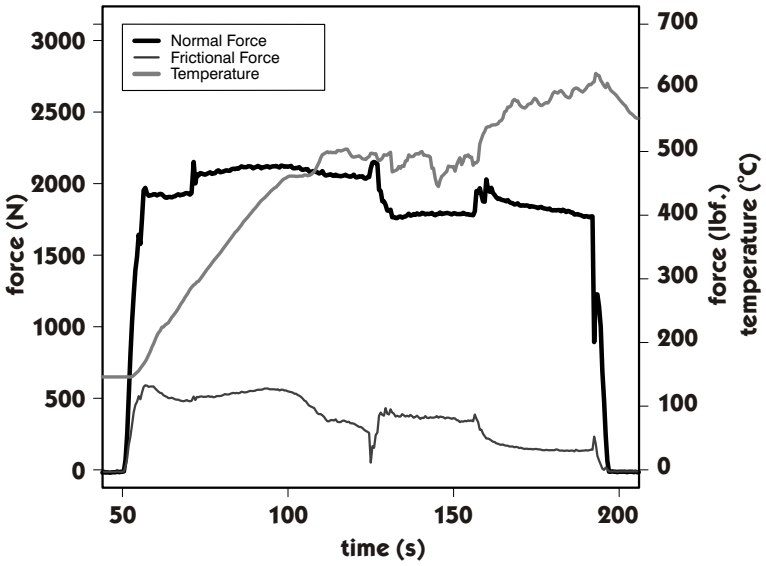

Figure 2.6: Time series data from a typical high temperature run.

Table 2.1: Experimental variable levels.

	Low	High
Velocity	0.40 m/s (78 SFM)	1.93 m/s (380 SFM)
Temperature	150^{o}C	550^{o}C
Normal Force	667 N (150 lbf)	2224 N (500 lbf)

In addition to the difficulty in achieving variable levels, there was some imprecision in measuring the values of velocity and temperature. Spindle speed was the only variable that could be directly set. However, during the course of a run the diameter of the tool decreased due to material deformation. In the extreme case the diameter changed from 25.4 mm (1 inch) to 19.0 mm (0.75 inches). This corresponds to a change of 0.10 m/s (20 SFM) and 0.5 m/s (100 SFM) at the low and high velocity levels respectively. This is about a 25% change in velocity. In order

to account for this decreasing velocity, the tool diameter was measured before and after the run. The diameter of each data point is estimated by a linear interpolation of the diameter based on the progress of the run.

The interface temperature was measured by thermocouples attached to the side of the PCBN blank near the front surface. The thermal conductivity of PCBN is relatively high, $2 \cdot 10^3 \frac{W}{m \cdot K}$. Because the thermal conductivity is high, it is reasonable to assume the temperature measured on the side of the PCBN is close to the interface temperature. However, there is some error associated with the temperature measurement because of this approximation.

2.4 Results and Discussion of Results

2.4.1 Significant Factors of Modeling Friction

The first phase of this experiment was to determine significant factors influencing the coefficient of friction. The second phase was to develop a model to describe observations. It was necessary to determine the significant factors that influence frictional force to further develop a valid model of the phenomenon. The coefficient of friction results for the factorial experiment design are shown in Table 2.2. The numbers in the $\overline{\mu}$ column are averages for the coefficient of friction calculated at each time step found within a range of 220 N (50 lbf), 50 ^{o}C, and at the RPM level. The coefficient of friction was calculated at each time step. An ANOVA analysis showed that normal force, velocity, and temperature all have significant effects on the coefficient of friction, μ. For this initial analysis, μ is defined as frictional force divided by normal force.

Table 2.2. Coefficients of friction at experimental variable level combinations. The average coefficient of friction is $\overline{\mu_{eff}}$ and the sample deviation of the coefficient of friction is $\sigma_{\mu_{eff}}$.

F_n	T	V	$\overline{\mu_{eff}}$	$\sigma_{\mu_{eff}}$
H	H	H	0.219	0.005
H	H	L	0.482	0.026
H	L	H	0.476	0.005
H	L	L	0.336	0.012
L	H	H	0.411	0.047
L	H	L	0.649	0.138
L	L	H	0.323	0.054
L	L	L	0.382	0.023

Another important observation about these data is a portion of the data that has decreasing slope. This decreasing slope can be seen in Figure 2.7. This data shows similar trends observed by Shaw [10] and Maekawa [11].

2.4.2 Statistical Model

Initially it was believed that each of the coefficients of the Maekawa [11] model could be made a function of temperature and velocity to produce a more valid model. This model is shown in Equations 2.2 through 2.5. Equation 3.11 is a model of the coefficient of friction as a function of temperature (T) and velocity (V). Equation 2.4 is a model of the shear flow stress. Equation 2.5 is a model fit parameter that could change depending on the temperature and velocity.

$$\tau_t = k(T,V) \cdot [1 - e^{\{-(\frac{\mu(T,V)\sigma_t}{k(T,V)})^{n'(T,V)}\}}]^{\frac{1}{n'(T,V)}}. \tag{2.2}$$

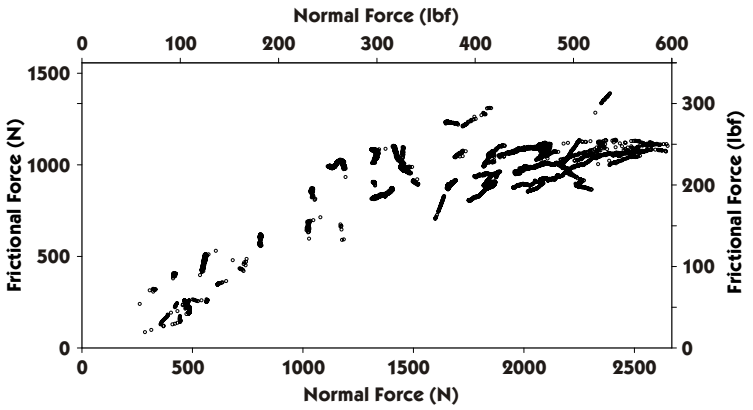

Figure 2.7. Frictional force vs. normal force at temperatures between 500 and 600 ^{o}C and velocities of 0.40 m/s (78 SFM).

$$\mu(T,V) = \beta_{11} + \beta_{12}T + \beta_{13}V + \beta_{14}TV. \tag{2.3}$$

$$k(T,V) = \beta_{21} + \beta_{22}T + \beta_{23}V + \beta_{24}TV. \tag{2.4}$$

$$n'(T,V) = \beta_{31} + \beta_{32}T + \beta_{33}V + \beta_{34}TV. \tag{2.5}$$

The iterative curve fitting technique used could not converge on values for various β parameters. model did not converge. Therefore, a different type of model was needed. Appendix A describes a number of models that were tested and found to be ineffective. These models either failed to converge or made no physical not make sense.

A simpler model that approximates the two opposing types of friction would consist of individual linear statistical models for each of the two types of friction modes. One model represents the Coulomb-Amonton's friction, while the other model represents plastic shear deformation friction. Coulomb-Amonton's friction, F_c, and plastic shear deformation friction, F_p, are shown here as Equations 2.6 and 2.7 respectively. The frictional force is the minimum of F_c and F_p. This is shown in Equation 2.8.

Table 2.3: Betas for each statistical model.

Coulomb-Amonton's Friction

$\beta_{c1}[1]$	β_{c2}	β_{c3}	$\beta_{c4}[\frac{s}{ft\cdot^oC}]$
0.2561	$1.266e-03[\frac{1}{^oC}]$	$9.716e-2[\frac{sec}{m}]$	$-3.238e-2[\frac{s}{m\cdot^oC}]$
0.2561	$1.266e-03[\frac{1}{^oC}]$	$1.617e-04[\frac{sec}{ft}]$	$-3.981e-06[\frac{s}{ft\cdot^oC}]$

Plastic Shear Deformation Friction

β_{p1}	β_{p2}	β_{p3}	β_{p4}
$84.20[N]$	$7.324[\frac{lbf}{^oC}]$	$6.4801[\frac{N\cdot s}{m}]$	$-8.726e-1[\frac{N\cdot s}{m\cdot^oC}]$
$18.93[lbf]$	$4.476e-01[\frac{lbf}{^oC}]$	$1.207e-01[\frac{lbf\cdot s}{ft}]$	$-1.201e-03[\frac{lbf\cdot s}{ft\cdot^oC}]$

$$F_c = (\beta_{c1} + \beta_{c2}T + \beta_{c3}V + \beta_{c4}TV)F_n. \tag{2.6}$$

$$F_p = \beta_{p1} + \beta_{p2}T + \beta_{p3}V + \beta_{p4}TV. \tag{2.7}$$

$$F_f = min(F_c, F_p). \tag{2.8}$$

In these equations the βs are the respective coefficients of each variable or combination of variables. The variables T, V, and F_n are temperature, velocity, and normal force, respectively. Table 2.3 shows the magnitudes of each β for the two models in both International System of units (SI) and Imperial system of units.

Figure 2.8 plots model predicted frictional force versus actual measured force for 33,487 data points obtained experimentally. The linear model that best fits the data is (Predicted Force) = 1.045(Measured Force) with an R^2 value of 0.83. These values show that the model is relatively good.

Figure 2.9 shows the Coulomb-Amonton's friction and plastic shear deformation model values at each of the experimental conditions. The model shows a coefficient of friction at low temperatures is at 0.3 and 0.4 depending on the velocity level. At high temperature level of 550 ^{o}C, the coefficient of friction increases to 0.8 for at low velocities, 0.40 m/s (78 SFM), and decreases to 0.2 for high velocities, 1.93 m/s (380 SFM). The model also shows that the plastic shear deformation friction is around 1300 N (300 lbf) for low temperature conditions. The plastic shear deformation friction is 979 N (220 lbf) at the high temperature and low velocity condition. While the plastic shear deformation friction is 222 N (50 lbf) at 550^{o}C and 1.93 m/s (380 SFM).

Figures 2.10 and 2.11 show the results of the model in a surface plot. Figure 2.10 shows the coefficient of friction as it relates to temperature and velocity. At low temperatures the coefficient of friction remains fairly constat for velocity. At high temperatures and low velocities the coefficient of friction becomes very large. At high velocities the coefficient of friction becomes very low.

Figure 2.11 shows the a surface plot of the plastic shear deformation frictional force. A surface similar to the shape of Figure 2.10 is found. At low temperatures the plastic shear deformation frictional force is relatively constant. At high temperatures the plastic shear deformation frictional force increases at low velocities and decreases at high velocities.

After creating the model, there were some trends that did not seem intuitive. For example, according to the model, plastic shear deformation friction increases with temperature at low velocities. One would expect that with this temperature increase, the material would soften. This material softening would reduce the fric-

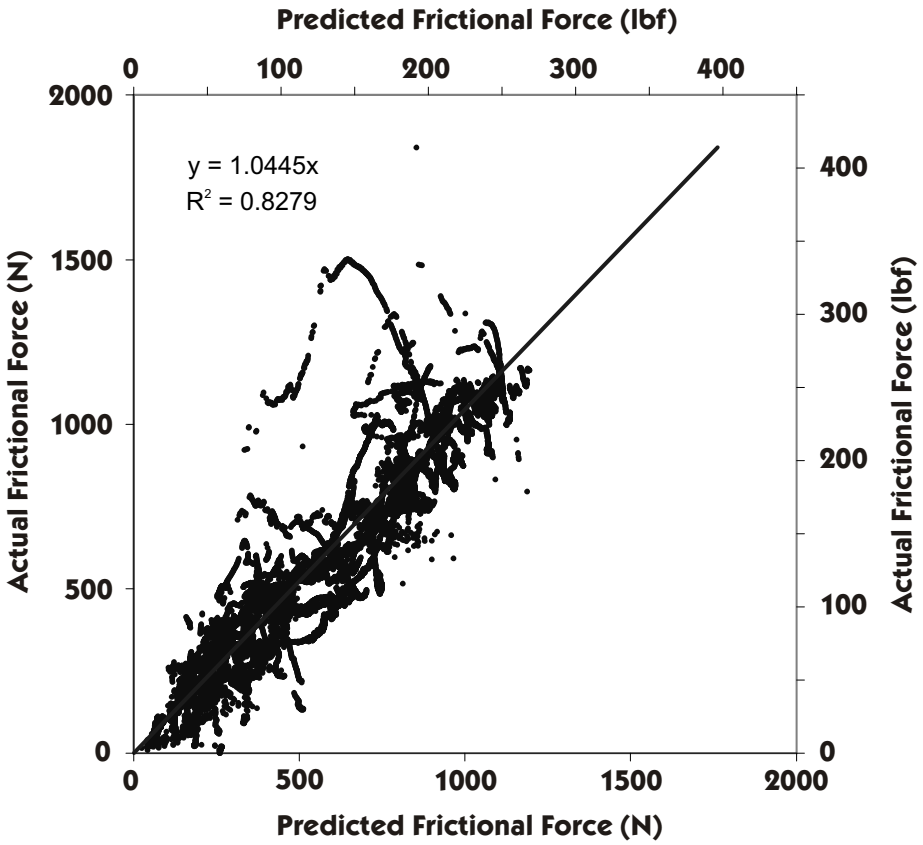

Figure 2.8: Model correlation and goodness of fit.

tion force. Figure 2.12 shows the increase of frictional force with temperature for low velocities.

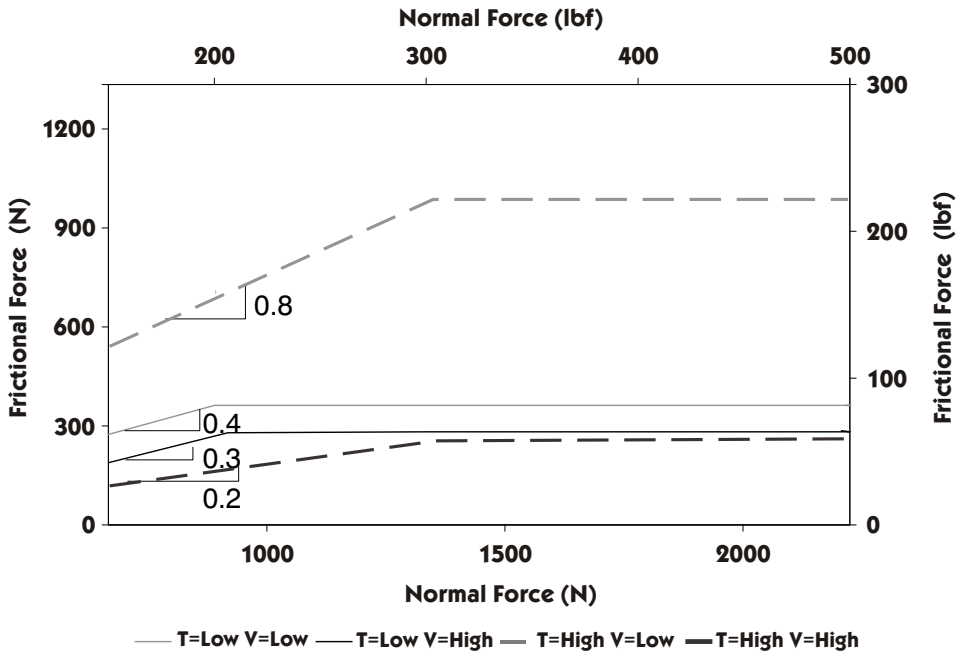

Figure 2.9. Coulomb-Amonton's and plastic shear statistical model results at the experimental variable level combinations.

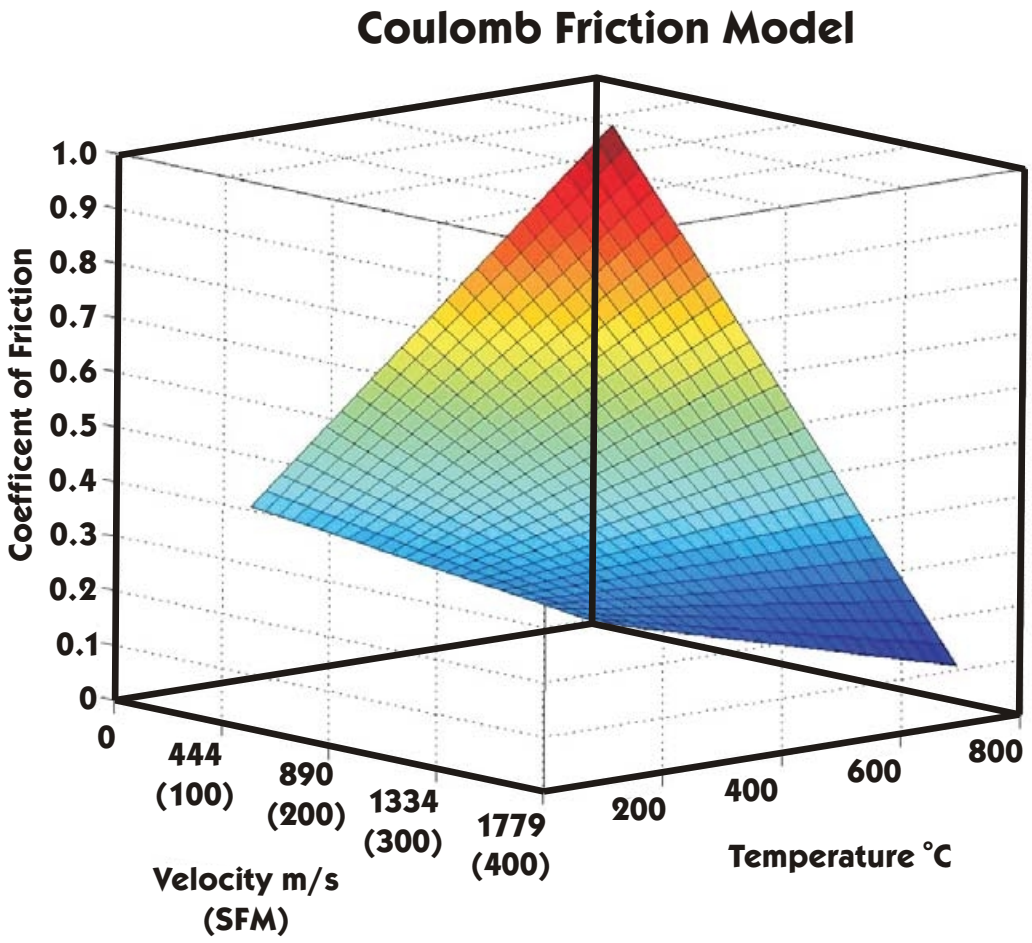

Figure 2.10: Coulomb-Amonton's friction statistical model surface plot.

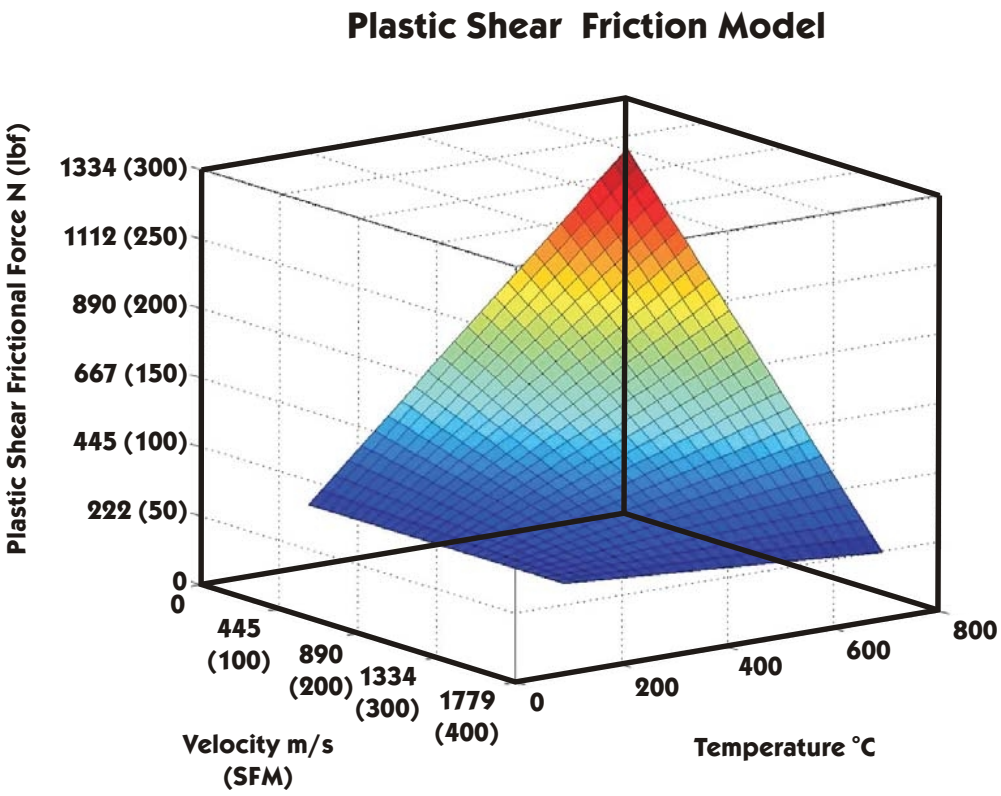

Figure 2.11: Plastic shear statistical model surface plot.

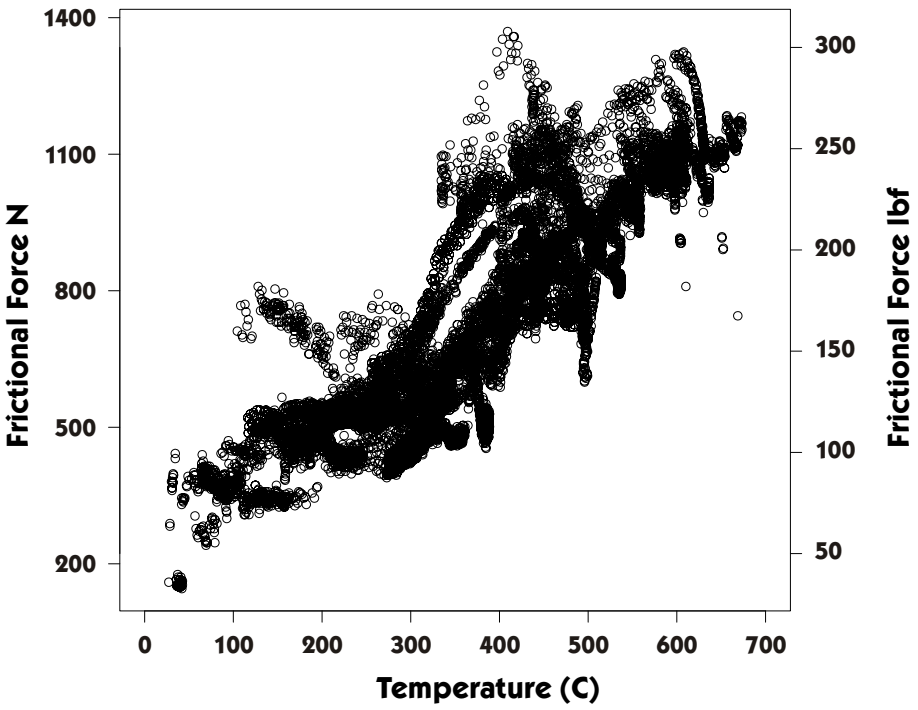

Figure 2.12. The plastic shear deformation frictional force increasing with temperature at low velocities.

2.5 Suggestions for Future Work

Future work needs to normalize the forces by apparent contact area. These experiments were not able to be normalized because the apparent contact area was unmeasurable. Coulomb-Amonton's friction is independent of apparent area. However, plastic shear deformation friction is dependent on apparent area. The main improvement to this work would be to have a measurable contact area during frictional measurement. This would allow stresses to be defined, rather than forces, which would be more useful in modelling the FSW process.

Also, these experiments are noisy. Future work should attempt to decrease noise. One method of reducing noise is to include only steady state frictional measurements. However, this is not possible when a range of values is needed for each experimental variable. Achieving steady state temperatures should be a goal. Some transient data will be needed to get data for the entire experimental range.

In addition, future work should gather more data at low temperatures where the data shows a plastic shear deformation friction characteristic. At low temperatures the coefficient of friction is predominantly Coulomb-Amonton's friction for the entire normal force range studied in this experiment. This produced a model that is not accurate for plastic shear deformation friction at low temperatures.

2.6 Conclusion

A friction-measuring mechanism is used to measure the frictional force at a variety of temperatures, velocities, and normal forces. Significant factors influencing the frictional force are identified. Temperature, velocity, and normal force are all significant factors. A statistical model describing the frictional behavior of the PCBN–1018 steel interface is developed that has a correlation is close to one. The coefficient

of friction between these materials is about 0.35 at temperatures less than 200^{o}C. The coefficient of friction decreases to about 0.2 around 550^{o}C and 1.93 m/s (380 SFM). The coefficient of friction around 550^{o}C and 1.93 m/s (78 SFM) is about 0.8. The plastic shear deformation plateau is about 979 N (220 lbf) at 550^{o}C and 0.40 m/s (78 SFM), while it is 222 N (50 lbf) at 550^{o}C and 1.93 m/s (380 SFM). Improvements are needed to produce a model suitable for a numerical model of the FSW process.

3 Using a Membership Function and Regression to Determine Frictional Model Coefficients

3.1 Introduction

Friction over a large range of normal loads shows two main characteristics. One characteristic it that the frictional force is proportional to the normal force by a constant μ. This is often referred to as Coulomb or Amonton friction. The other characteristics is that an increase in the normal force does not increase the frictional force. This is called plastic shear deformation friction.

One investigator, Shaw [10], described this phenomenon. For Amonton's laws to apply, only the asperities are plastically deformed. As loads increase, the plastic region also increases. When loads are high enough, plastic deformation of the bulk material occurs. As the loads continue to increase, eventually, the frictional force is defined completely by material properties. Depending on the plasticity state, three different friction regions are formed. The two extreme regions are characterized by either Amonton's laws or bulk material characteristics. The other friction region is a transition between these two opposing frictional characteristics. Figure 3.1 is a schematic representation of these three friction regions.

These friction regions cannot be represented by one linear model. Maekawa et al. [11] developed a frictional model for free-machining steels. This model preserved the characteristics of Amonton's laws and the plateau defined by material characteristics. The measured data parameters, normal stress, and friction shear stress

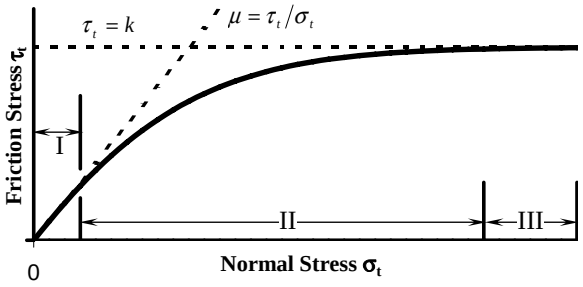

Figure 3.1: Schematic of the three friction regimes [11].

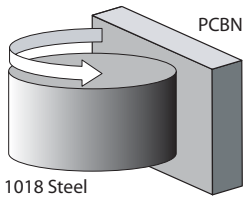

Figure 3.2. The type of frictional measurement for this experiment is a rotating cylinder on a stationary flat plate.

are represented in Equation 3.1 as σ_t and τ_t respectively, and n' is a set variable.

$$\tau_t = R \cdot k \cdot [1 - e^{\{-(\frac{\mu\sigma_t}{k})^{n'}\}}]^{\frac{1}{n'}}. \tag{3.1}$$

This model is shown in Equation 3.1. The model has three model fit parameters: a proportional constant that relates the material to the reference material (R), the coefficient of Coulomb-Amonton's friction (μ), and the shear flow stress of the material (k).

Stratton et al. [12] studied the frictional interface between PCBN and 1018 steel rotating a cylindrical surface on a stationary flat plate. A schematic of the type of measurement geometry is shown in Figure 3.2. They found similar results to those of Shaw [10] and Maekawa et al. [11] in that they observed both Coulomb-Amonton's and plastic shear deformation friction. They also showed that temperature and velocity influence the Coulomb-Amonton's and plastic shear deformation friction. The plastic shear deformation friction is the friction that is determined by bulk material

characteristics. Since Coulomb-Amonton's and plastic shear deformation friction depend on temperature and velocity, Equation 3.1 is not sufficient to describe the interface. This paper proposes a different model and discusses the regression technique.

3.2 Characteristics of the Data

The data gathered in the experiment described by Stratton et al. [12] displayed two distinct patterns. For some data the frictional force increases with normal force (Coulomb-Amonton's friction). For the other data there is no additional increase in frictional force with the increasing normal force (plastic shear deformation friction). Both the sloped line and the horizontal line describing this data is also influenced by temperature and velocity. Figure 3.3 shows both portions of the data at about 550^{o}C and 0.40 m/s (78 SFM). In addition, both of Coulomb-Amonton's and plastic shear deformation friction regions are influenced by temperature and velocity.

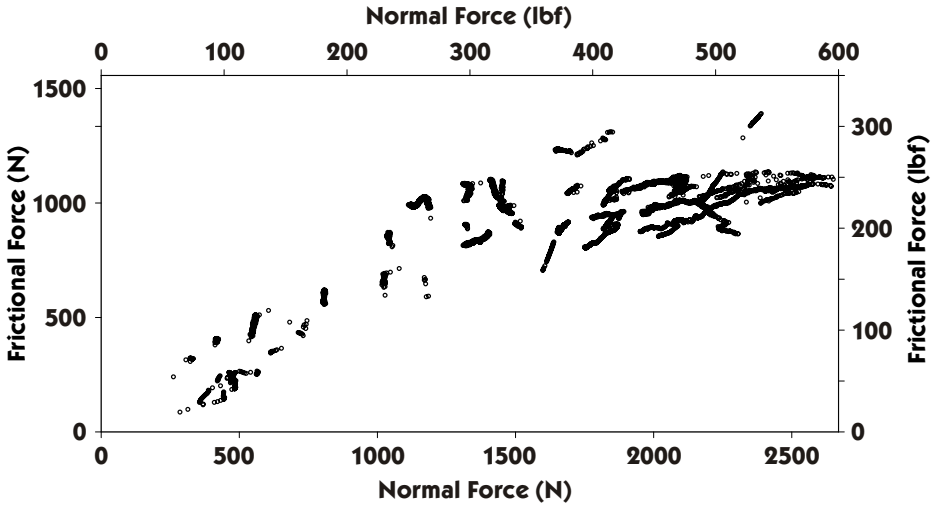

Figure 3.3. Frictional force vs. normal force at temperatures between 500 and 600 ^{o}C and velocities of 0.40 m/s (78 SFM).

3.3 Model Development

The obvious model choice would be to take the Maekawa et al. [11] model and add temperature and velocity terms to each of the terms that could be dependent on temperature and velocity. Equation 3.2 shows the resulting model.

$$\tau_t = k(T,V) \cdot [1 - e^{\{-(\frac{\mu(T,V)\sigma_t(T,V)}{k(T,V)})^{n'(T,V)}\}}]^{\frac{1}{n'(T,V)}}. \tag{3.2}$$

However, this model did not converge. Various models were considered and can be found in Appendix A. The model that was selected was a combination of the two linear statistical models shown in Equations 3.3 and 3.4. These models were proposed by Stratton [13]. The frictional force would be the minimum of the two models shown in Equation 3.5.

$$F_c = (\beta_{c1} + \beta_{c2}T + \beta_{c3}V + \beta_{c4}TV)F_n. \tag{3.3}$$

$$F_p = \beta_{p1} + \beta_{p2}T + \beta_{p3}V + \beta_{p4}TV. \tag{3.4}$$

$$F_f = min(F_c, F_p). \tag{3.5}$$

The model shown in Equation 3.3 represents a Coulomb-Amonton's frictional model (Region I). Equation 3.4 represents a plastic shear deformation model (Region III). Unlike the theory presented by Shaw et al. [10], this model does not include a transition region. Neglecting the transition region is necessary to get a model to converge and analyze the overall trends. In addition, future work could use these models as a basis for a model that has curvature and represents all the regions.

Traditional linear regression methods would result in a poor fit because all the data would be used when only a portion of the data applies. No meaningful information can be gathered from the data when traditional regression methods are used. Dividing the results into two different groups manually makes the regression

an qualitative problem and prone to human error. A quantitative approach to dividing the data into groups is desirable. A new method called membership function regression was developed to solve this problem. Membership function regression combines a concept used in fuzzy logic with a linear regression technique. It creates a quantitative method of assigning the influence a particular data point has on the regression. In addition, this method fits the model to the data points and determines the influence of each individual data point on the model fit.

3.4 Membership Function Regression

3.4.1 Membership Function

Membership function regression is based on the idea of a membership function, a concept used in fuzzy logic, and is applied to weighted regression. A membership function is a measure of the degree that the properties of one element could be described by the properties attributed to a set or membership of that set. Membership functions have a domain of all possible elements and a range from zero to one. Zero means that the element does not belong or does not share the properties of the set. One means that the element belongs completely to the set or has all the properties of the set. Any number in between zero and one means that the element has a portion of membership.

It is also important to note that this is not a probability, and opposing sets are not mutually exclusive. An element can have a membership of one for two opposing sets if the properties attributed to that element are the properties that make it eligible for membership in both sets. An element may also belong to neither of the opposing sets.

3.4.2 Regression Algorithm

The key characteristics of the model functions are identified bases on observations of the data. Based on these criteria, membership functions were developed for each of the friction type models.

This characteristics are described using two statistical models, Coulomb-Amonton's frictional force (F_c) and plastic shear deformation frictional force (F_p), shown here as Equations 3.6 and 3.7. These models have different structures. F_c is proportional to normal force (F_n), and F_p is independent of F_n. These equations intersect so the functional form of the model is the minimum of F_c and F_p and the specified conditions shown in Equation 3.8.

$$F_c = \beta_{11} \cdot F_n + \beta_{12} \cdot F_n \cdot V + \beta_{13} \cdot F_n \cdot T + \beta_{14} \cdot F_n \cdot V \cdot T \tag{3.6}$$

$$F_p = \beta_{21} + \beta_{22} \cdot V + \beta_{23} \cdot T + \beta_{24} \cdot V \cdot T \tag{3.7}$$

$$F_f = min(F_c, F_p) \tag{3.8}$$

Initially, all the data points are considered a full member of both sets and regression produces the initial estimate of the coefficients.

Analytic functions are created to make quantitative comparisons between the model, which embodies the main characteristics of interest and the data. The quantitative comparisons are the perpendicular distance of the data point to the model in the F_f-F_n plane and distance from the transition point between the models. These quantitative comparisons are shown in Figures 3.4. Figure 3.4 is a representation of a frictional data measured at a specific value of temperature and velocity. Data points close to the sloping line are likely to reflect Coulomb-Amonton's friction and data close to the horizontal line and to the right of the intersection point are likely to be plastic shear deformation friction.

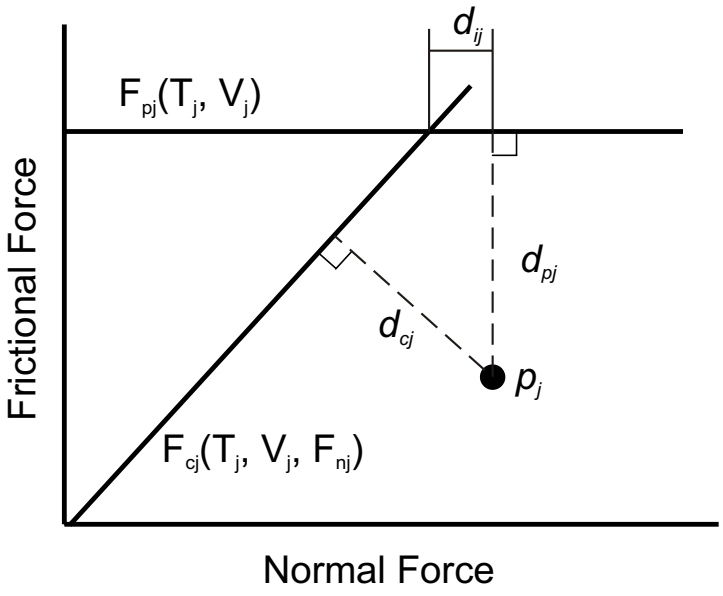

Figure 3.4: Characteristics quantitative comparisons.

The perpendicular distance from a point, p_j, to a line, F_{kj} is d_{kj}. The variable p_j is the point at a specific temperature velocity, frictional force, and normal force shown in Equation 3.9.

$$p_j = (T_j, V_j, F_{nj}, F_{f_j}) \tag{3.9}$$

The line is shown in Equation 3.10, where μ_j is the slope of the line in the F_f-F_n plane. The equation for μ_j is shown in Equation 3.11. Figure 3.5 shows a graphical representation of this equation and the variable associated with that equation.

$$d_{cj} = \frac{F_{nj} \cdot (\mu_j) - F_{fj}}{(1 + (\mu_j)^2)^{\frac{1}{2}}} \tag{3.10}$$

$$\mu_j = \beta_{11} + \beta_{12} \cdot V_j + \beta_{13} \cdot T_j + \beta_{14} \cdot T_j \cdot V_j \tag{3.11}$$

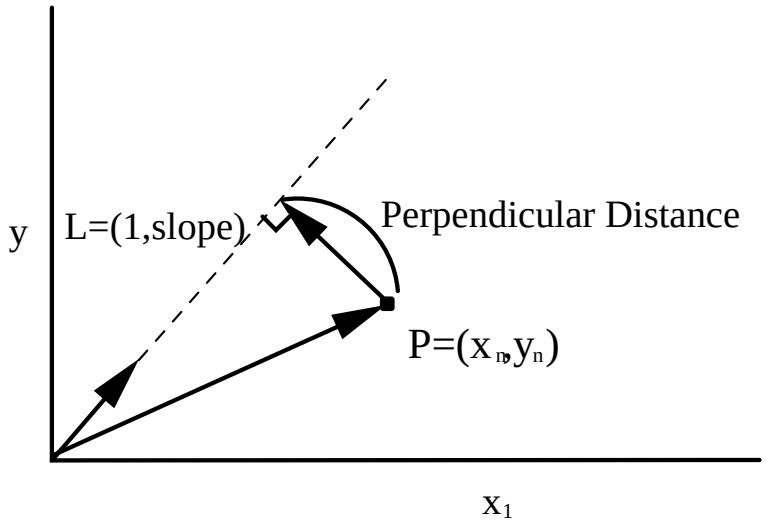

Figure 3.5. Variable definition schematic for perpendicular distance shown in Equation 3.10.

Quantitative comparison between the data and the F_p model is shown in Equation 3.12.

$$d_{pj} = F_{pj} - F_{fj} \tag{3.12}$$

Since it is desirable that the model be a function, another quantitative measure is based on the transition point, or intersection point, between the two models. This measure is the magnitude between F_{nj} and the intersection point, F_{Ij}, at T_j, and V_j. The distance between data and F_{Ij} is given by Equation 3.13. Where the intersection force is given by Equation 3.14.

$$d_{Ij} = F_{nj} - F_{Ij} \tag{3.13}$$

$$F_{Ij} = \frac{\beta_{21} + \beta_{22} \cdot V_j + \beta_{23} \cdot T_j + \beta_{24} \cdot V_j \cdot T_j}{\beta_{11} + \beta_{12} \cdot V_j + \beta_{13} \cdot T_j + \beta_{14} \cdot V_j \cdot T_j} \tag{3.14}$$

The distances are transformed by a normalization function to bring these distances into a range of (0,1). The normalization function used is based on cumulative normal distribution function, $\phi(X, Mean, StandardDeviation)$. The Equations

3.10, 3.13, and 3.12 are each transformed by Equation 3.15, 3.16, and 3.17.

$$N_{cj} = 1 - \phi(d_{cj}, MV_c, \frac{SV_c}{6}) \tag{3.15}$$

$$N_{pj} = 1 - \phi(d_{pj}, MV_p, \frac{SV_p}{6}) \tag{3.16}$$

$$N_{Ij} = \phi(d_{Ij}, MV_p, \frac{SV_I}{6}) \tag{3.17}$$

Figure 3.6 shows a normal cumulative distribution curve along with a graphical representation of the parameters.

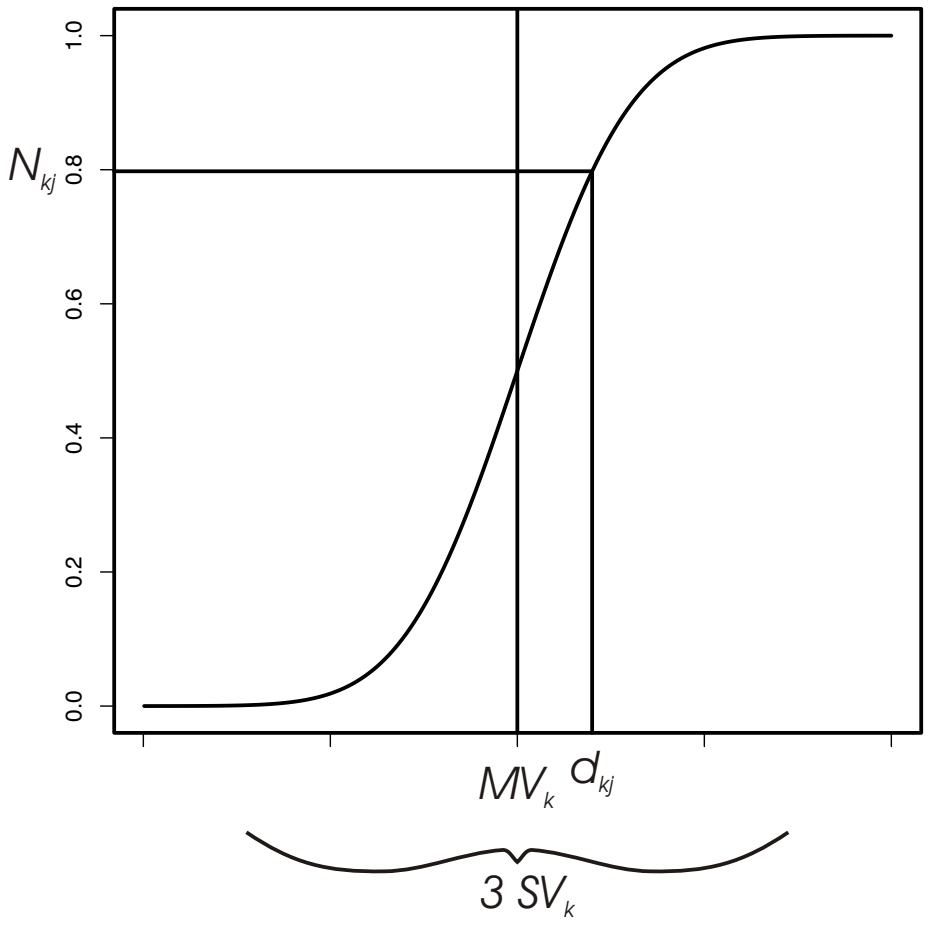

Figure 3.6: Normal cumulative distribution curve.

The normal distribution cumulative function has desirable characteristics. The cumulative normal distribution function makes values above the mean value (MV)

closer to one while those values below MV are closer to zero. MV is a value that determines at what point the transition will occur. The sharpness value (SV) is a value that represents the sharpness of the transition region between sets. The smaller the SV value is, the sharper the transition.

A subset of the data that shows entirely one characteristics and around a specific small range of temperatures and velocities is used to estimate the sample deviation, s. The MV_c and MV_p are estimated by Equations 3.18 and 3.18.

$$MV_c = 3s_c \tag{3.18}$$

$$MV_p = 3s_p \tag{3.19}$$

Experiments with values of SV showed very little effect over a wide range of SV. The variable SV was chosen to be small for all three functions, this makes the normalization functions approximate a step function.

A hypothetical two dimensional model was created to explain these equations. This hypothetical model has a coefficient of friction equal to 1 and a plastic shear deformation friction equal to 350. Based on these values, the model intersection normal force is 350. An MV was chosen of 40 for both MV_c and MV_p. An SV was chosen of 0.025 for both SV_c and SV_p. Values for MV_I and SV_I were chosen as 0.0 and 0.025 respectively. These are values used for demonstration purposes and are not the values used in the regression technique. In addition, force units are arbitrary. Figures 3.7 through 3.9 are a pictorial representations of the normalization function in Equation 3.15 through 3.17 for each of the normalization functions. Equations 3.15, 3.16, and 3.17 are the Coulomb-Amonton's friction, plastic shear deformation friction and intersection force normalization functions. The dark black line on each of the figures is a representation of the model. Isolines of the normalization function value are shown on the figure. The Coulomb-Amonton's normalization function, N_c,

contour plot in Figure 3.7 shows the normalization function values calculated at each frictional force and normal force combination. The N_c is 0.5 for force values 40 offset below the model line. Above that offset, the normalization function values increase to one, while below that offset the normalization function decrease to zero.

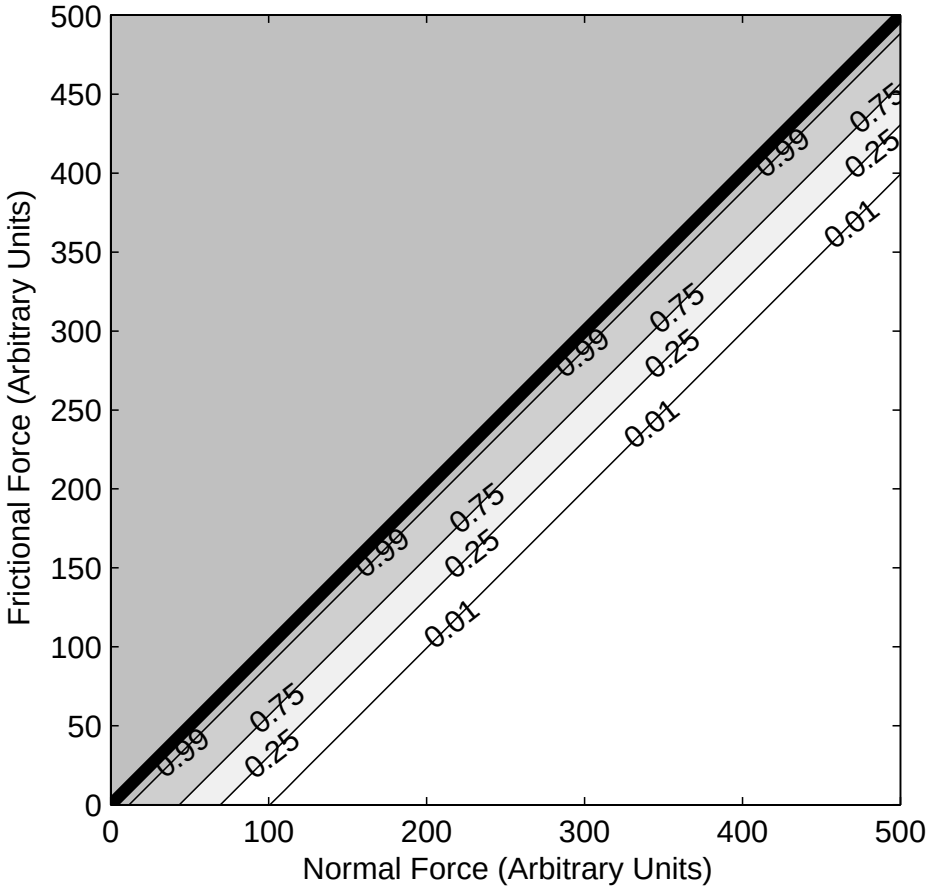

Figure 3.7: Coulomb-Amonton's normalization function contour plot.

The plastic shear deformation friction normalization function, N_p, contour plot in Figure 3.8 shows the normalization function values calculated at each frictional force and normal force combination. The N_p is 0.5 for force values 40 offset below the model line or a frictional force of 310. Above that offset the normalization function values increase to one, While below that offset the membership function decrease to zero.

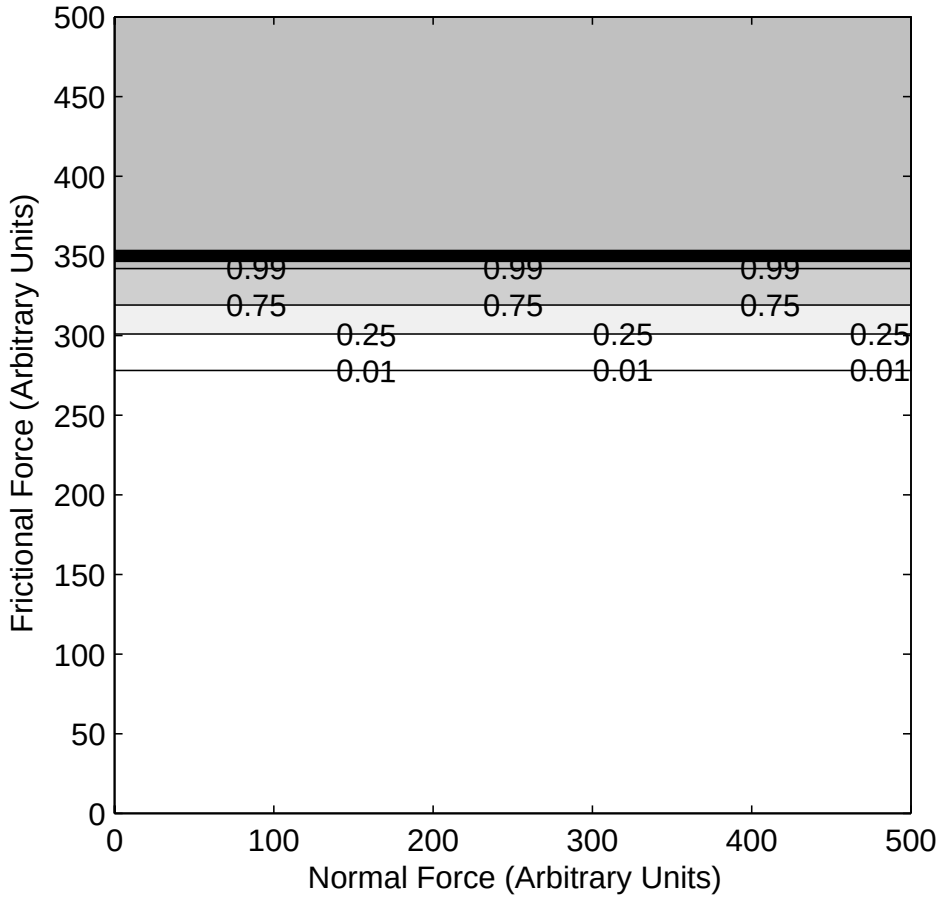

Figure 3.8: Plastic shear deformation friction normalization function contour plot.

The intersection force normalization function, N_I, contour plot in Figure 3.9 shows the normalization function values calculated at each frictional force and normal force combination. The N_I is 0.5 for force values at the intersection line. To the values to the right of this line increase to one. The values to the left of this line decrease to zero.

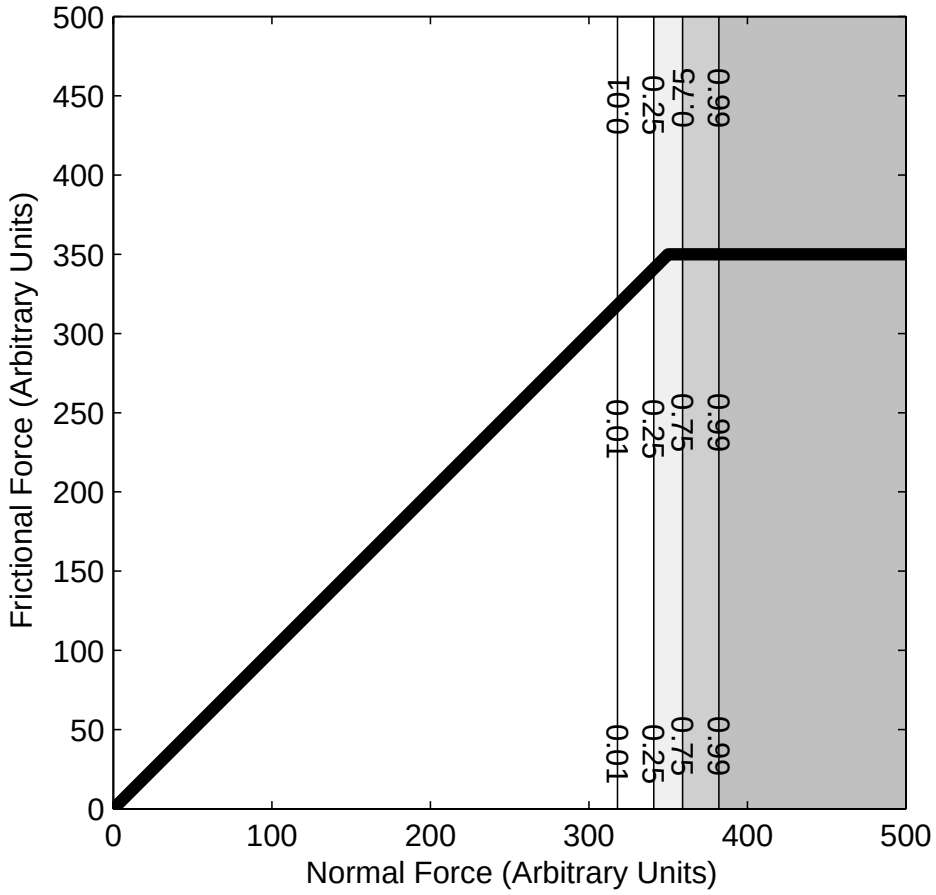

Figure 3.9: Intersection force intermediate membership function.

These normalization distances are used to create membership functions for both Coulomb-Amonton's and plastic friction membership functions shown in Equations 3.20 and 3.21.

$$M_{cj} = (N_{cj}) \cdot (1 - N_{Ij}) \tag{3.20}$$

$$M_{pj} = (N_{pj}) \cdot (N_{Ij}) \tag{3.21}$$

Figures 3.10 and 3.11 show the resulting membership functions for Coulomb-Amonton's and plastic shear deformation friction respectively. Points near the coulomb line and above and to the left of the intersection point typically indicate Coulomb Friction, while those near and above the plastic line and to the right of the intersection point indicate plastic friction. Figures 3.10 and 3.11 show the same trend with the membership functions. These membership functions are used as regression weights (w)

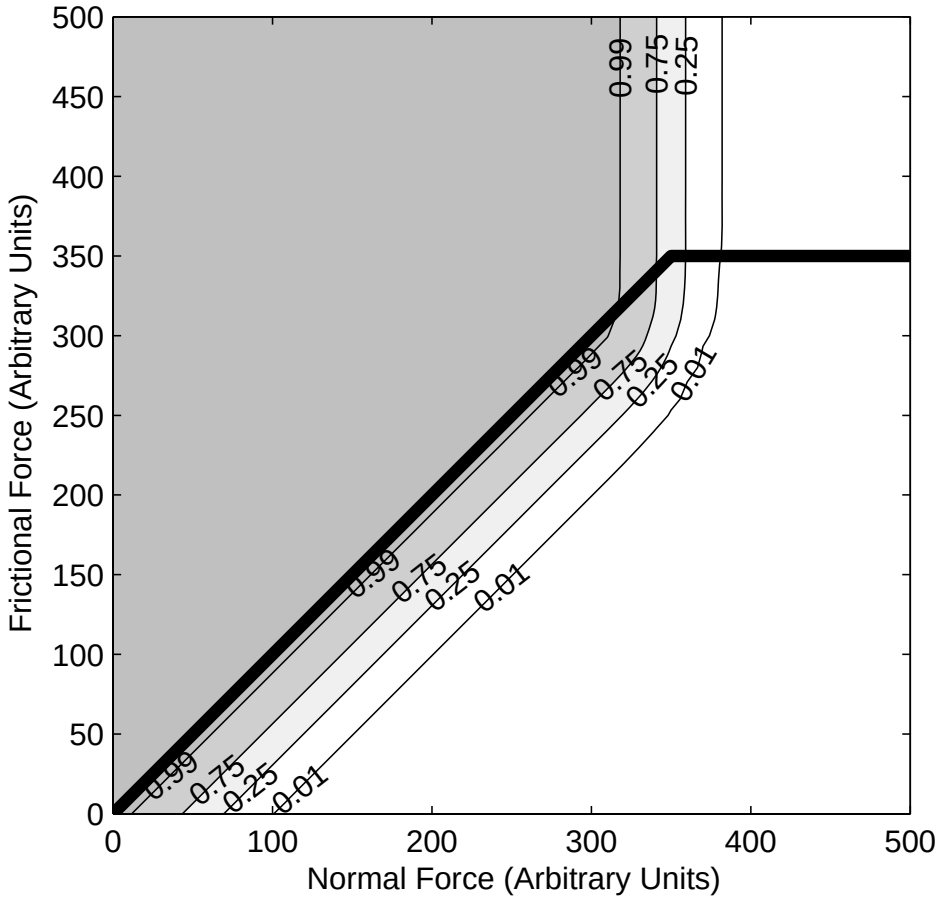

Figure 3.10: Coulomb-Amonton's Membership function contour plot.

as shown in Equations 3.22 and 3.23.

$$w_{cj} = M_{cj} \tag{3.22}$$

$$w_{pj} = M_{pj} \tag{3.23}$$

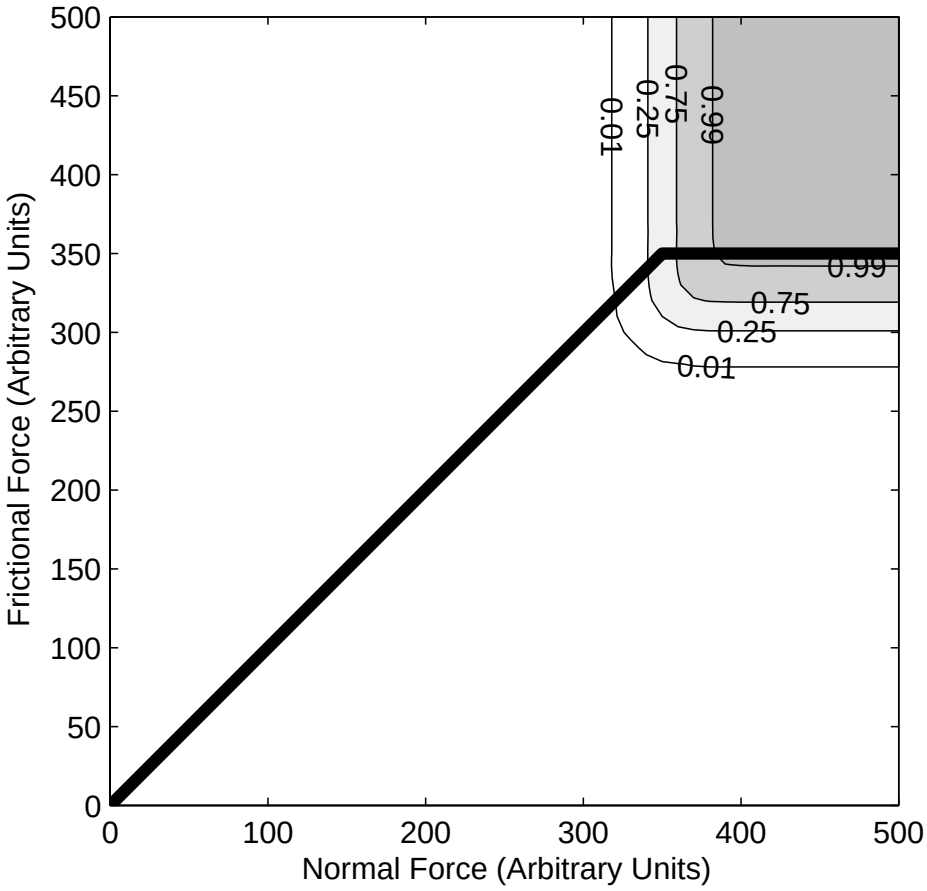

Figure 3.11: Plastic shear deformation friction membership function contour plot.

Table 3.1: Variable ranges for F_n and T.

variable	variable name	Low	High
F_n	Normal Force	400 N (100 lbf)	3000 N (600 lbf)
T	Temperature	100 ^{o}C	600 ^{o}C

The data's influence on the resulting models coefficients is based on the strength the data point contributes to the characteristics of the respective model. The values of the coefficients determined in one iteration are used to calculate the membership function values, M_c and M_p in the next iteration. The regression and recalculation of the membership functions continue until the decrease in SEE of the regression is less than a specified tolerance. An example of a couple of iterations using this algorithm are found in Appendix C.

3.5 Applying Membership Function Regression to the Data

There are three experimental variables in this experiment. None of the variables can be set. A classical factorial experiment was the goal, although some conditions were unachievable. F_n and T are treated as continuous variables because of the large amount of data over the entire range. The range for F_n and T is shown in Table 3.1. Due to deformation of the tool, V does have some variation. However, it could be considered a factored variable with three levels. These levels and the associated sample deviations can be seen in Table 3.2.

The levels have a variable number of data points. Table 3.3 shows the number of data points for each level of velocity. Since the number of data points at each level is not equal, there would be some bias toward the low velocity level data.

Table 3.2: Velocity variable levels

		mean $[\frac{m}{s}\ (\frac{ft}{min})]$	sample deviation $[\frac{m}{s}\ (\frac{ft}{min})]$
V_l	Low Velocity	0.3882 (76.42)	0.008738 (1.72)
V_m	Medium Velocity	1.292 (254.33)	0.03160 (6.22)
V_h	High Velocity	1.776 (349.61)	0.1386 (27.28)

Table 3.3: Number of data points at each level of V

Low	Medium	High	Total
23,453	2,138	7,896	33,487

To prevent this bias, the data was factored by velocity. Each velocity had its own model associated with it.

Membership function regression was performed where $MV_c = MV_p = 62$ and $MV_I = 0$. In addition, the SV_k was 0.001 so that the normal cumulative distribution function approximated a step function.

Two experiments were performed to evaluate the robustness of the method. A random subset of half the data was used to produce coefficients for the model. The change in parameters as the random subset is changed shows the robustness of the fit. A distribution of the coefficients is also produced.

Initially, the first experiment data was sampled to make sure that the same proportion of the data came from each velocity level. Half the data was randomly selected from each of the three velocity levels, and the regression algorithm was implemented. This process was repeated 10,000 times. The distribution of the coef-

ficients in this experiment are shown in Figure 3.12. Multiple maximum likelihood is shown in Figure 3.12 by multiple peaks on the distribution curves. This result is common for mixture models.

The multiple maximum likelihoods result is evidence that the model is biased by a differing number of data points at each level of velocity. An additional test was performed to see if these multiple maximum likelihoods can be eliminated. The two-linear-model form was modified so that there would be separated model for each of the velocity levels. These models are shown in Equations 3.24 through 3.29. A similar bootstrapping method and regression algorithm was implemented except with a factored velocity. The results from this bootstrapping method are shown in Figure 3.13. These plots appear to be more normal than was observed in the previous, unfactored bootstrapping algorithm. These normal distributions are desirable and show that the bias of the velocity levels has been eliminated.

$$F_{cl} = \gamma_{11l} \cdot F_n + \gamma_{12l} \cdot T \cdot F_n \tag{3.24}$$

$$F_{cm} = \gamma_{11m} \cdot F_n + \gamma_{12m} \cdot T \cdot F_n \tag{3.25}$$

$$F_{ch} = \gamma_{11h} \cdot F_n + \gamma_{12h} \cdot T \cdot F_n \tag{3.26}$$

$$F_{pl} = \gamma_{21l} + \gamma_{22l} \cdot T \tag{3.27}$$

$$F_{pm} = \gamma_{21m} + \gamma_{22m} \cdot T \tag{3.28}$$

$$F_{ph} = \gamma_{21h} + \gamma_{22h} \cdot T \tag{3.29}$$

In Figure 3.14, F_{cx} γs are plotted against velocity where velocity is spaced out to give some idea of the distribution of the coefficients. A variety of models could be drawn through these γs. Figure 3.14 also shows possible interpolations of the coefficients. The interpolation that was chosen was a linear interpolation between the median of the coefficients.

Table 3.4: Coefficient for the F_c model.

0	intercept (I)	V
γ_{11}	0.2561100	0.0001623
γ_{12}	1.266e-03	-3.996e-06

In addition, linear models were created to interpolate the coefficients for the F_{px} models. In this case, there is no good estimate for the medium level γ. The medium velocity level coefficients were neglected, and the coefficient model is an interpolation between the low and high velocity γs. The results for each of the coefficients for model F_c are shown in Table 3.4.

Equations 3.30 and 3.31 relate the gammas to F_n, V, T, F_c, and F_p. With some simplification, these equations are the same form of model as the form of the model proposed earlier.

$$F_c = (\gamma_{11I} + \gamma_{11V} \cdot V) \cdot F_n + (\gamma_{12I} + \gamma_{12V} \cdot V) \cdot F_n \cdot T \tag{3.30}$$

$$F_p = \gamma_{21I} + \gamma_{21V} \cdot V + (\gamma_{21I} + \gamma_{22V} \cdot V) \cdot T \tag{3.31}$$

3.6 Evaluation of Method

There are two ways of evaluating the models. The first is as a predictive model, shown in Equation 3.32.

$$F_f = min(F_c, F_p) \tag{3.32}$$

Figure 3.15 shows the relation between the actual and predicted values for frictional force where the transition point is enforced. These models have a correlation of 1.0445 and an R^2 value of 0.83.

A second was to evaluate the model is to be a non-predictive form where the data point follows the model that fits the best shown in Equation 3.33. This model is non-predictive because it uses the measured frictional force, y, to decide which of the predictive models should apply.

$$F_f = \begin{pmatrix} F_c, & \text{if } \left|F_c - y\right| < \left|F_p - y\right|); \\ F_p, & \text{else.} \end{pmatrix} \tag{3.33}$$

This model results in a better correlation as shown in Figure 3.16 show a better correlation. The relation between actual and predicted values for this non-predictive model have a correlation of 0.9775 and an R^2 value of 0.92. Both fits seem quite good with the amount of noise that is perceived. The model's improving suggests that the predictive model does not capture all the necessary information. There is some Coulomb friction data that is being interpreted as plastic shear deformation friction, and there is some Coulomb friction data above the plastic shear deformation friction force. One possible explanation for this is the contact area during friction measurement is not constant throughout the experiments. If the contact area was larger, higher forces would be observed before the transition to the plastic shear deformation frictional characteristic. Another possible explanation for this could be that there is no estimate for the F_p model at certain conditions because there is not enough data.

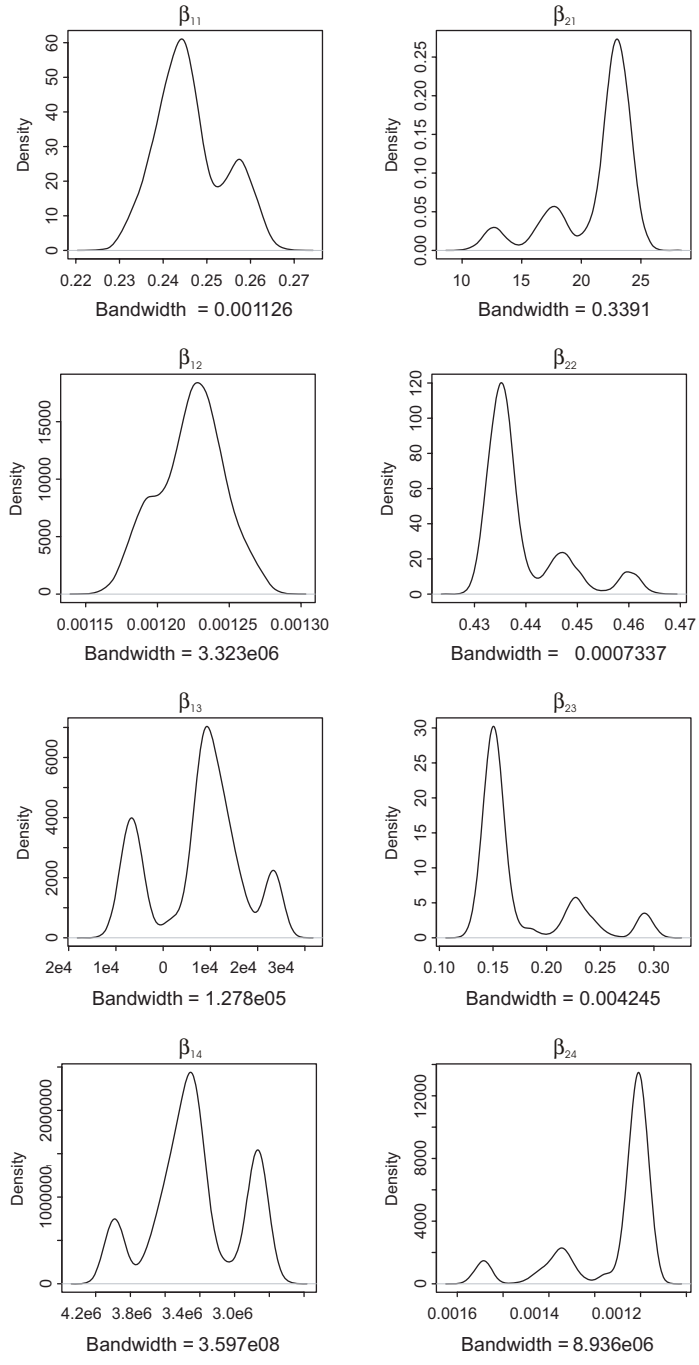

Figure 3.12. Beta distribution plots for the coefficients in Coulomb and plastic shear deformation friction models.

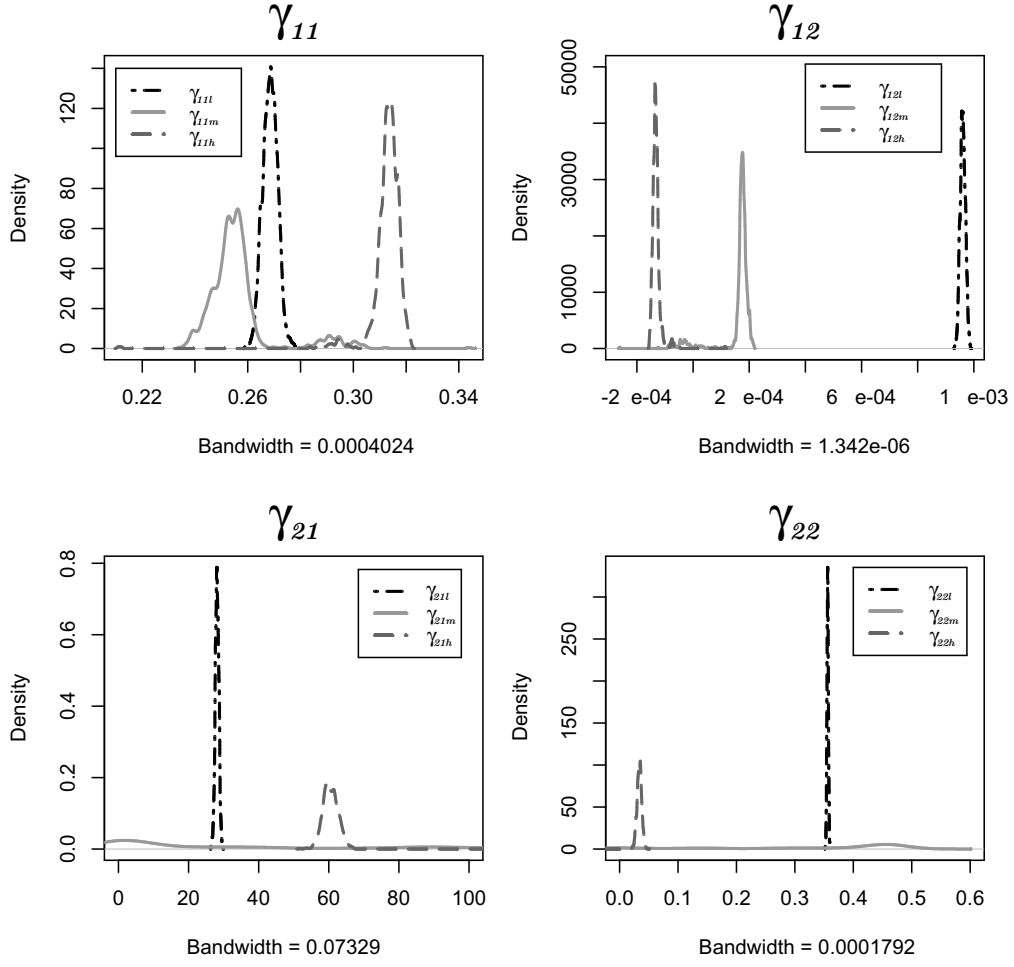

Figure 3.13: The gammas from the factored velocity bootstrapping method.

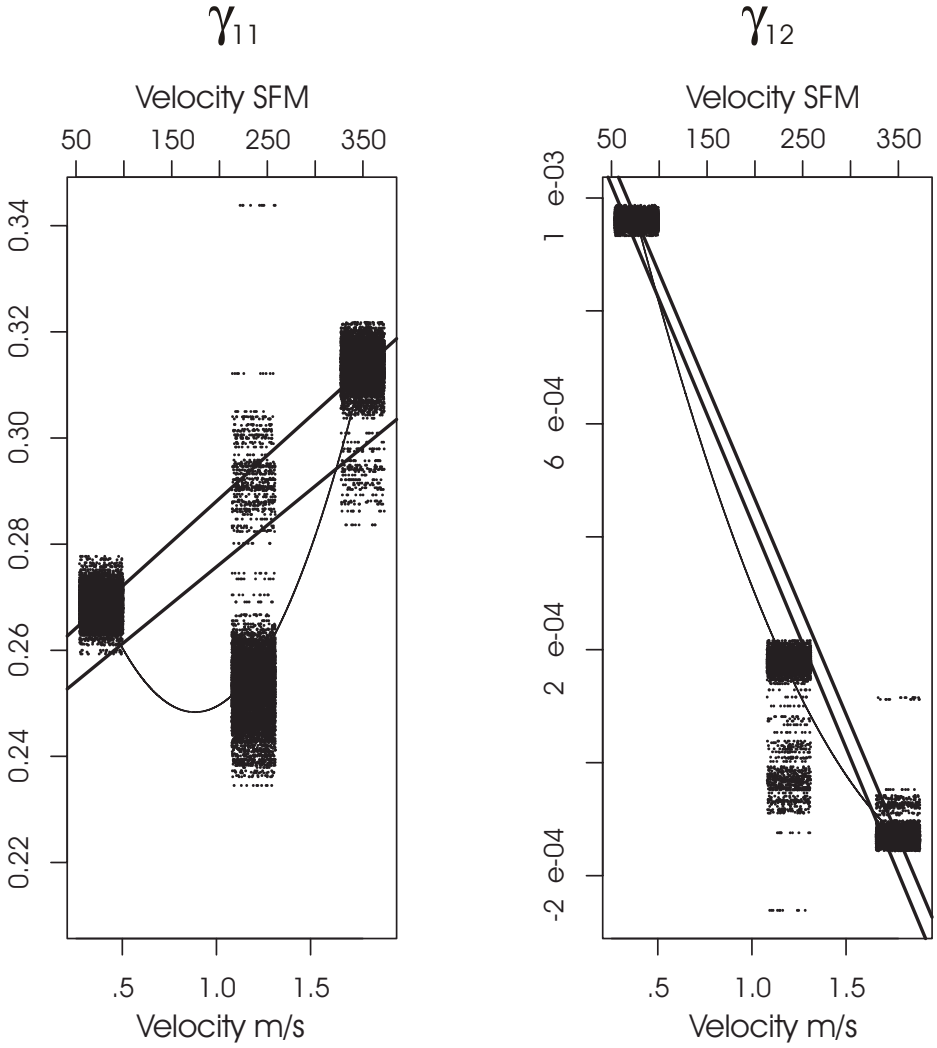

Figure 3.14: Possible interpolations of the gammas.

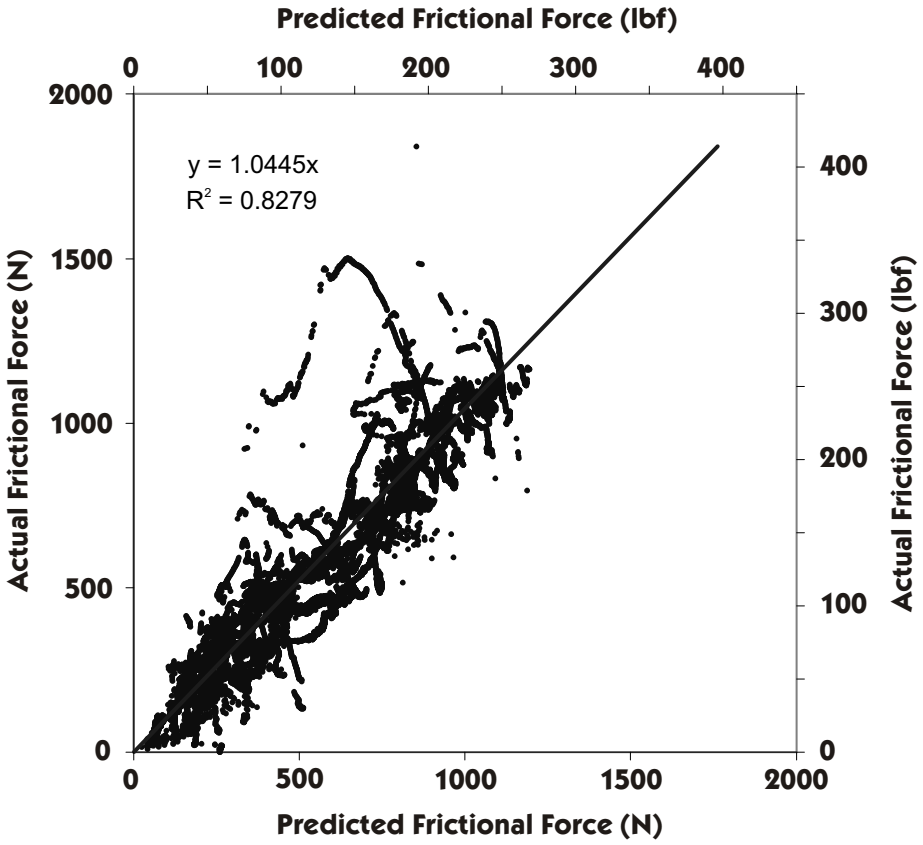

Figure 3.15: Correlation plot.

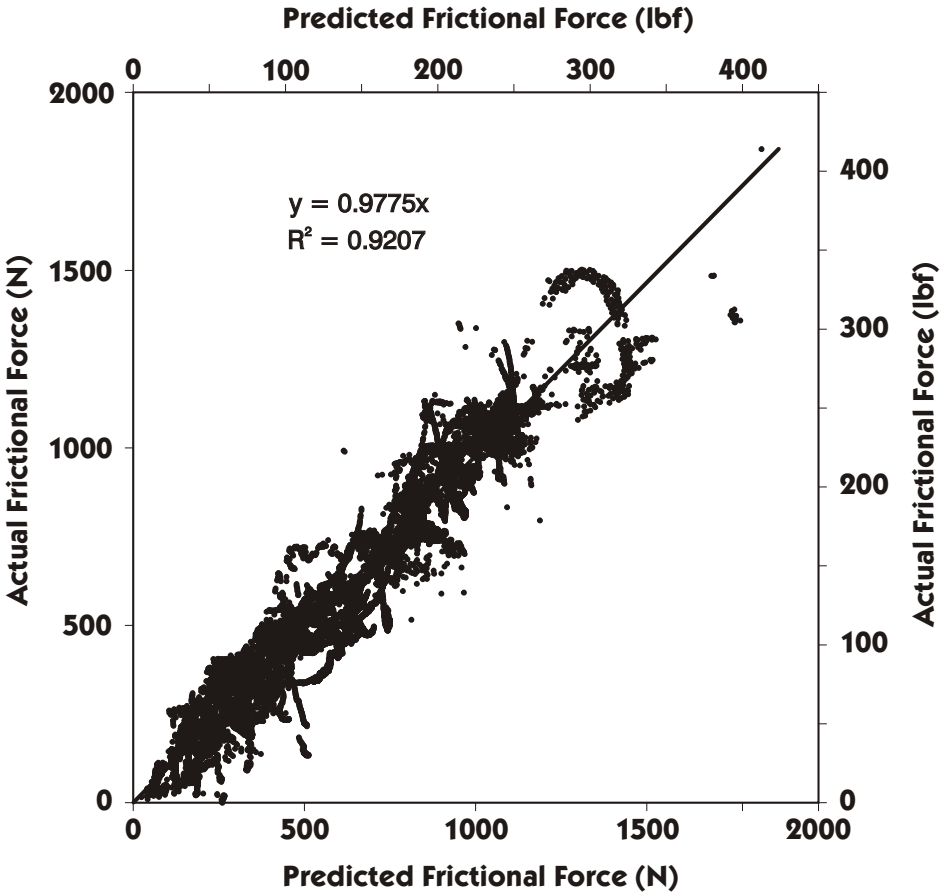

Figure 3.16: Non-predictive model correlation plot.

3.7 Conclusion

A model that represents the data from the experiment described by Stratton et al. [12] was determined to be the minimum of two linear models with interactions. These linear models represent the two types of friction. One model represents the Coulomb portion of the data. The other model represents the plastic shear deformation friction. These models have a correlation of 0.9775 and an R^2 value of 0.92 as a non-predictive model. These models have a correlation of 1.0445 and an R^2 value of 0.83 as a predictive model. Membership function regression performs well when a single data set has data that represents two characteristics. The membership function regression enabled this data to be analyzed where traditional regression techniques would have failed. In addition, this regression technique can be modified to applications where data portrays more than one pattern that can not be described by a single model. Also, this method allows model forms to be simpler and enable robust linear regression techniques to be used.

4 Evaluating a Cylinder on Disk Method of Measuring Friction

4.1 Abstract

A quantitative understanding of frictional phenomena between the tool and the workpiece is essential for accurate modelling of the Friction Stir Welding (FSW) process. This experiment uses a disk on a plate friction measuring technique. Equipment is instrumented to measure normal force, torque, RPM, and temperature.

A method of measuring the tool-workpiece interface is proposed that allows frictional measurements to be made under extreme conditions. Precession of the tool on the workpiece caused any plastic shear deformation friction measurements to be invalid. There is no significant evidence that the interface reached plastic shear deformation friction conditions. For this data, an effective Coulomb friction is about 0.4, regardless of the temperature, velocity, or force.

4.2 Introduction

4.2.1 Friction Stir Welding

Friction Stir Welding (FSW) is a solid-state joining process where a nonconsumable tool deforms two workpieces along the interface to form a union between the two workpieces. This welding process has gained popularity over the past decade due to the superior material properties it produces. The advantages of this process include the following: no filler material, no fumes, no solidification cracks, low porosity,

low weld distortion, the ability to weld dissimilar metals, and greater strength and corrosion properties [1, 2].

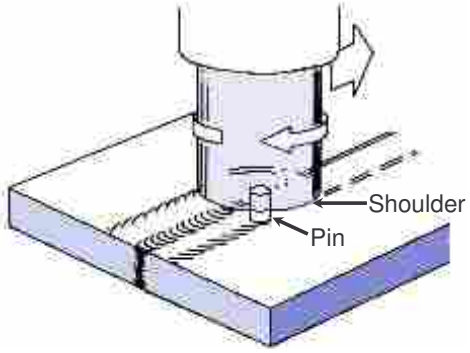

Figure 4.1: Friction stir welding schematic [3].

The FSW process uses a tool that consists of a pin and a shoulder. The pin plunges into the seam between two workpieces until the shoulder reaches the workpiece surface. The tool dwells in place until sufficient heat is produced to traverse along the seam between the workpieces. As the tool traverses along the seam, a weld is produced. The weld is completed by extracting the tool from the workpiece. Figure 4.1 shows a schematic of the welding.

4.2.2 FSW Analytical Models

The FSW process is a complex process involving large gradients and complicated physical phenomena. Analytical models of FSW provide the key to greater understanding that cannot be achieved with experimental measurements alone. If an accurate FSW model could be developed, it could be used to improve process understanding and to further process development. One important physical phenomenon, the frictional interface between the tool and the workpiece during FSW, has not been adequately characterized for implementation in an FSW model. Current FSW models have either made simple assumptions about the frictional interface or ne-

glected the interface all together. Khandkar et al. and many others [4] assumed a constant coefficient of friction. Seidel et al. [5] assumed that there was zero relative velocity between the pin and the workpiece. Song et al. [6] recognized that the coefficient of friction could change during friction stir welding but did not have data, so they assumed an effective coefficient of friction. Frigaard et al. [7] used an effective coefficient of friction that changed during the simulation. Only when the conditions for local melting were met did the algorithm reduce the coefficient of friction to keep the temperature from exceeding the melting temperature; all other times the effective coefficient of friction was held constant. Doug et al. and Chen et al. [8, 9] recognized that the coefficient of friction depended on temperature; however, they did not specify the friction model used.

4.2.3 Previous Work

There is some work that has been done to explore the frictional interface over high normal loads. According to Shaw [10], at the sliding frictional interface, plastic regions form at asperity junctions. For Amonton's laws to apply, only the asperities are plastically deformed. As loads increase, the plastic region also increases. When loads are high enough plastic deformation of the bulk material occurs. As the loads continue to increase, eventually the frictional force is defined completely by material properties. Three different friction regions are formed depending on the plasticity state. The two extreme regions are characterized by either Amonton's laws or bulk material characteristics. The other friction region is a transition between these two opposing frictional characteristics. Figure 4.2 is a schematic representation of these three friction regimes.

Maekawa et al. [11] developed a frictional model for free-machining steels. This model preserved the characteristics of Amonton's laws and the plateau defined by

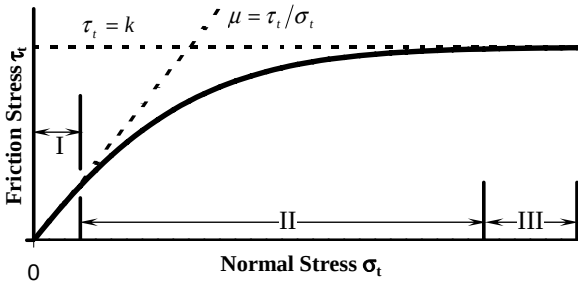

Figure 4.2: Schematic of the three friction regimes [11].

material characteristics. The measured data parameters,normal stress, and friction shear stress are represented in Equation 4.1 as σ_t and τ_t respectively where n' is a constant.

$$\tau_t = R \cdot k \cdot [1 - e^{\{-(\frac{\mu\sigma_t}{k})^{n'}\}}]^{\frac{1}{n'}}. \tag{4.1}$$

This model is shown in Equation 4.1. The model has three model fit parameters: a proportional constant that relates the material to the reference material (R), the coefficient of Coulomb-Amonton's friction (μ), and the shear flow stress of the material (k).

However, this friction model is not sufficient for FSW modelling, because it does not include dependence on temperature or surface velocity, which may be significant factors determining frictional shear. Stratton et al. [12] measured the frictional interface between PCBN and 1018 steel by rotating the curved surface of the cylinder against a flat plate. In their experiment, they found that Coulomb frictional force depended on temperature, velocity, and normal force. Plastic shear deformation friction depends only on temperature and velocity. The friction model they propose consists of one linear statistical model for each of the two friction types shown in Equations 4.2 and 4.3; the frictional force would be the minimum of these two equations, shown in Equation 4.4.

$$F_c = (\beta_{c1} + \beta_{c2}T + \beta_{c3}V + \beta_{c4}TV)F_n. \tag{4.2}$$

$$F_p = \beta_{p1} + \beta_{p2}T + \beta_{p3}V + \beta_{p4}TV \tag{4.3}$$

$$F_f = min(F_c, F_p) \tag{4.4}$$

One of the main disadvantages to their experiment was that it did not have a measurable contact area. Therefore, the models could not be expressed in terms of normal and shear stresses. Measurable contact area matters in plastic shear deformation friction because the shear force of a material depends on the area being sheared.

4.2.4 Objective

The objective of this research is to evaluate the cylinder on disk method of measuring both coulomb and plastic shear deformation friction. This method will be used to experimentally investigate the PCBN–304 stainless steel frictional interface for a range of temperatures, velocities, and normal pressures. This configuration has a measurable contact area so that normal pressure and frictional shear stress can be calculated. In addition, the experimental method allows the frictional interface to be studied at a variety of temperatures, normal pressures, and velocities.

4.3 Experimental Procedure

4.3.1 Overview

The goal of the experiment is to measure frictional shear at a variety of temperatures, velocities, and normal pressures. This is done by rotating a flat PCBN surface against a cylindrical stainless steel tool with a concentric cylindrical pocket. Figure 4.3 shows the type of frictional measurement performed in this study. The geometric form that could be chosen is limited by the size of PCBN. The PCBN

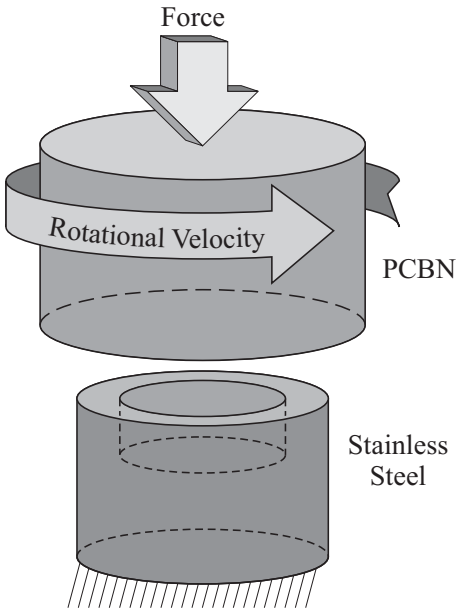

Figure 4.3. The type of frictional measurement for this experiment is a rotating cylinder on a stationary workpiece.

tools are made from a PCBN cylinder that is about 22 mm (0.87 inches) in diameter. In addition, the geometry needed to resist buckling and collapse due to large normal and torque loads. Furthermore, a cylinder with a pocket on a disk is similar in form to FSW. Unlike FSW there is an estimate of relative linear velocity of the contact surface. However, the velocity does vary across the contact surface. The amount the velocity varies is reduced by making the thickness of the contact area small. The decrease in accuracy due to variation in velocity is a necessary trade-off to have a measurable contact area.

While the PCBN surface is rotating against the flat stainless steel surface, the visible surface temperature, torque, and normal force are measured. These quantities determine the interface temperature, the frictional shear, and the normal pressure.

Figure 4.4: FSW machine

The experimental equipment used consisted of an FSW machine, a PCBN tool, a stainless steel workpiece, a friction-measuring apparatus, DATAQ A/D equipment, a FLIR infrared camera, and three computers.

The FSW machine is shown in Figure 4.4. This machine is a computer controlled, three axis FSW machine. The machine uses a PLC to control the machine processes. Some of the quantities that are controlled on the machine are the displacement of the tool in the Z direction, the X directions, and revolutions per minute. The Z direction is parallel to the axis of the rotating tool. The X and Y directions are perpendicular to that axis. The machine can also measure forces in all three axes using piezoelectric load cells. The load cells are shown in Figure 4.5. The machine uses a feedback loop to control the Z position and maintains a constant, given Z load. This machine also samples the process data measurements approximately at ten times per second.

A PCBN tool, shown in Figure 4.6, was mounted in the spindle of the FSW machine. The tool has a length of about 95 mm ($3\frac{3}{4}$ inches). The last 6.4 mm (0.25

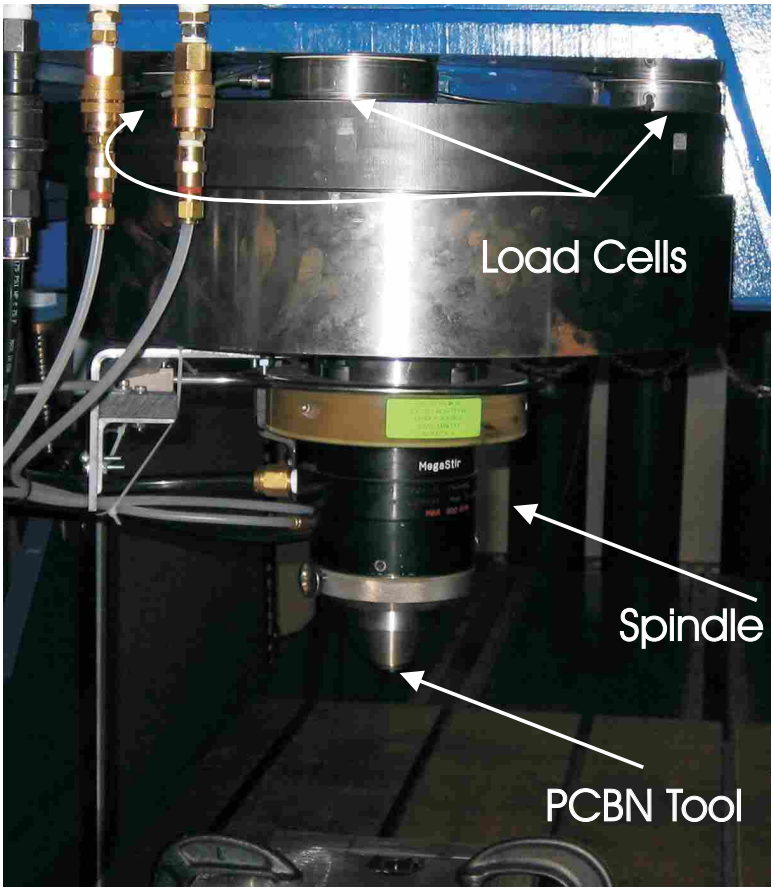

Figure 4.5: FSW machine spindle

Figure 4.6: PCBN tool

inches) of the tool is the visible portion of the PCBN blank. The MS80 grade blank is about one inch in diameter.

The stainless steel workpiece, shown in Figure 4.7, is a one-inch diameter rod two inches in length. The last 0.4 inches has a slightly smaller diameter with a concentric pocket. This results in a flat ring of stainless steel material, which is where the PCBN tool rubs against the workpiece in this friction study.

The stainless steel workpiece is held and supported in a measurement apparatus, shown in Figure 4.8. This measurement apparatus consists of a chuck, a liquid heat exchanger, and a reaction torque meter. The stainless steel workpiece is clamped in a lathe scroll chuck. Below the chuck is a liquid heat exchanger and a reaction torque meter. The reaction torque meter is a Himmelstein and Company Model RTM 2050(6-3) torque meter with a range of 678 N-m (6000 lbf-in). Below the

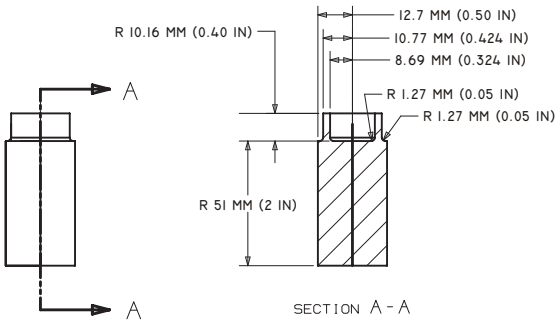

Figure 4.7: Workpiece drawing

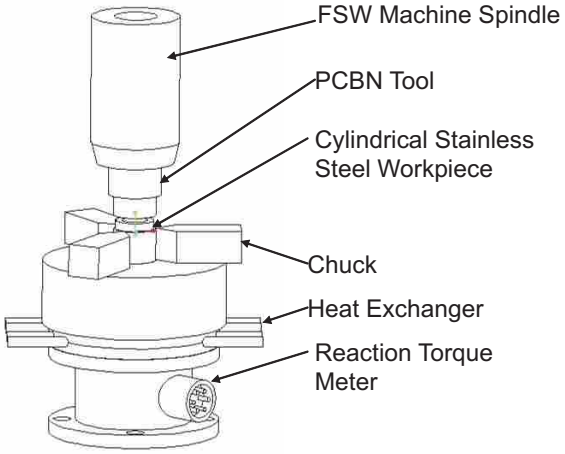

Figure 4.8: Measurement apparatus.

reaction torque meter is steel block to mount the measurement apparatus to the friction stir welding machine.

The A/D equipment is a DATAQ DI-722-32-USB. This equipment allows the load cells to be measured 1,000 times per second.

The FLIR infrared camera can be used to estimate the interface temperature. An infrared camera is used to measure the surface temperature of the tool in a line of sight from the camera. Figure 4.9 is an image taken with the infrared camera. Using software provided with the camera, each pixel of the infrared image is converted to a temperature. Only data along a line segment along the length of the center

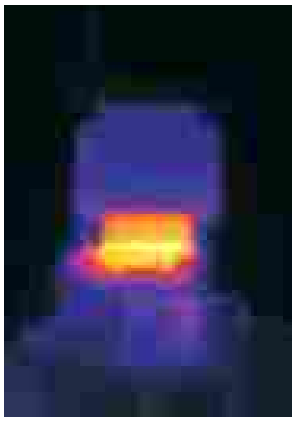

Figure 4.9: Infrared image of the tool and workpiece during an experiment.

of the tool and workpiece is needed. The temperature measurement is calibrated on the portion of the image that has PCBN. All other portions of the image have a lower emissivity than the PCBN and therefore have a lower temperature than their actual temperature. The data acquired on the line is written to a text file each second. Figure 4.10 shows the temperature profile of this image. The interface temperature is the only temperature needed. The interface temperature is the maximum temperature of the temperature profile. In the case of Figure 4.10, the interface temperature is about 500 ^{o}C.

4.3.2 Coordination of Instrumentation

The FSW machine computer does not have enough computing capabilities to control the FSW machine PLC, record the PLC's data, acquire data 1,000 times per second, and record thermal images of the process. Sufficient computing capabilities are ensured by dividing computation tasks among three computers: the FSW machine computer, the high speed data acquisition computer, and the infrared camera computer. Figure 4.11 shows a schematic of the signal flow and coordination of the computers.

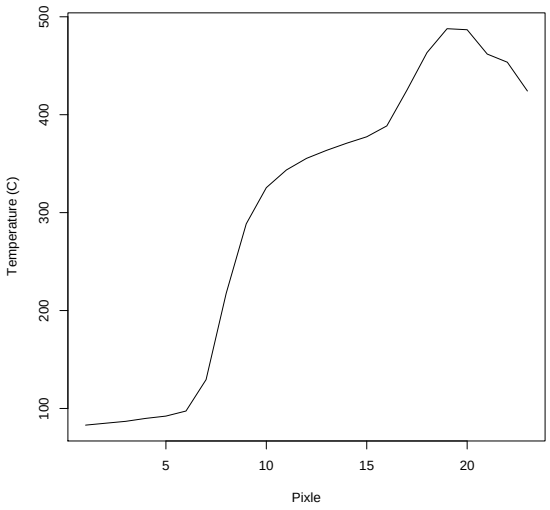

Figure 4.10. Temperature profile of a line down the center of the tool and the workpiece.

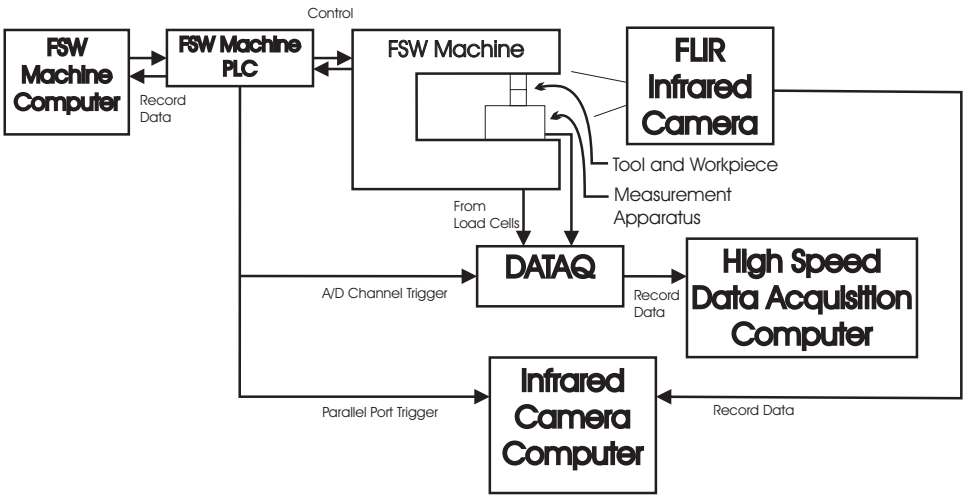

Figure 4.11: Schematic showing signal flow and coordination of three computers.

The FSW machine computer downloads the chosen program to the PLC and also records the signals that the PLC acquires from instrumentation.

The PLC acquires data at 10 times per second and also controls the FSW machine. When the experimental process initiates, the PLC produces a voltage that triggers the other two computers to record data.

The high speed data acquisition computer monitors all channels. When a high level voltage is measured on the trigger channel, the computer records the instrumentation signals. When the signal goes back down to low, the computer stops recording data.

Likewise, the thermal camera computer records data when the PLC signal is high and stops recording data when the PLC signal is low. However, this is done through the parallel port of the computer.

4.4 Converting Measured to Practical Quantities

4.4.1 Converting Torque to Frictional Shear Stress and Force to Normal Stress

The measured quantities, torque and force, need to be converted to practical quantities, shear, and normal pressure. Equations that relate torque to shear are developed, starting with the definition of torque in Equation 4.5. Torque, force, and radius are T, F, and r respectively. Since magnitudes are sufficient, this paper will only use scalar values for the rest of the derivation.

$$\overrightarrow{T} = \overrightarrow{F} \times \overrightarrow{r} \tag{4.5}$$

An equation was developed that relates torque with frictional shear stress for the geometry used in this experiment. The geometry related to this experiment is shown in Figure 4.12 with $F = \tau A$ substitution result in Equation 4.6.

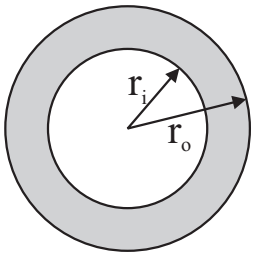

Figure 4.12: Rubbing surface area of the stainless steel workpiece.

$$T = \tau r A \tag{4.6}$$

τ and A are frictional shear stress and area respectively. The radius over the cross section is not constant, so the differential version of Equation 4.6, where $dA = 2\pi r dr$, is shown in Equation 4.7. The resulting equations are shown in Equations 4.7, 4.8, and 4.9.

$$dT = 2\pi\tau r^2 dr \tag{4.7}$$

$$T = \int_{r_i}^{r_o} 2\pi\tau r^2 dr \tag{4.8}$$

$$T = \frac{2}{3}\pi\tau(r_o^3 - r_i^3) \tag{4.9}$$

Solving for τ results in Equation 4.10.

$$\tau = \frac{3}{2}\frac{T}{\pi(r_o^3 - r_i^3)} \tag{4.10}$$

Another way to convert the torque to shear is using a thin-walled version of the equation. The thin-walled approximation is used for this paper. This approximation equation is shown in Equation 4.11, where mean radius and thickness are r_m and t respectively.

$$\tau = \frac{T}{2\pi r_m^2 t} \tag{4.11}$$

The variance propagation equations for τ are shown in Equation 4.12.

$$\begin{aligned} Var(\tau) &= \left(\frac{1}{2\pi r_m^2 t}\right)^2 Var(T) \\ &+ \left(\frac{T}{\pi r_m^3 t}\right)^2 Var(r_m) \\ &+ \left(\frac{T}{2\pi r_m^2 t^2}\right)^2 Var(t) \end{aligned} \tag{4.12}$$

This variance propagation equation for τ approximation do not inappropriately scale the variances when measurements are not known precisely.

Similarly, equations that relate force to normal pressure are developed, starting with the definition of stress in Equation 4.13.

$$\sigma = \frac{F}{A} \tag{4.13}$$

Using $A = 2\pi r_m t$ results in Equation 4.14.

$$\sigma = \frac{F}{2\pi r_m t} \tag{4.14}$$

Applying the variance propagation formula results in Equation 4.15.

$$\begin{aligned} Var(\sigma) &= \left(\frac{1}{2\pi r_m t}\right)^2 Var(F) \\ &+ \left(\frac{F}{2\pi r_m^2 t}\right)^2 Var(r_m) \\ &+ \left(\frac{F}{2\pi r_m t^2}\right)^2 Var(t) \end{aligned} \tag{4.15}$$

4.4.2 Converting RPM to Velocity

Traditionally the velocity of a point on a rotating cylinder is computed by Equation 4.16. The velocity at a radius of zero would be zero. The velocity of a point on that cylinder would increase proportionably with the radius.

$$V = 2\pi r(RPM) \tag{4.16}$$

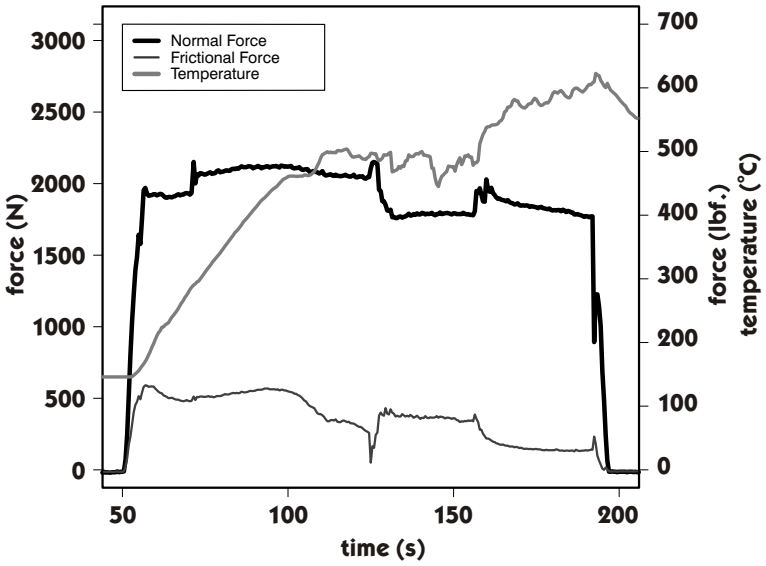

Figure 4.13: Time series data from a typical high temperature run.

This experimental design reduces the range of velocity by making a cylindrical pocket in the workpiece. An average velocity is used as a approximation of the velocity of the surface shown in Equation 4.17.

$$V_m = 2\pi \left(\frac{r_o + r_i}{2} \right) (RPM) \tag{4.17}$$

4.5 Results and Discussion of Results

4.5.1 Experimental Data

Results similar to Stratton et al. [12] were expected. Figure 4.13 shows typical data gathered in their experiment. Their data is relatively well behaved.

Five runs were performed. There were no significant differences in the five runs, so only the last run will be discussed. All five runs shared unexpected loud, audible vibrations and visible tool precession. The first initial goal was to just look at the data to determine what was going on with the experiment. Figure 4.14 shows the

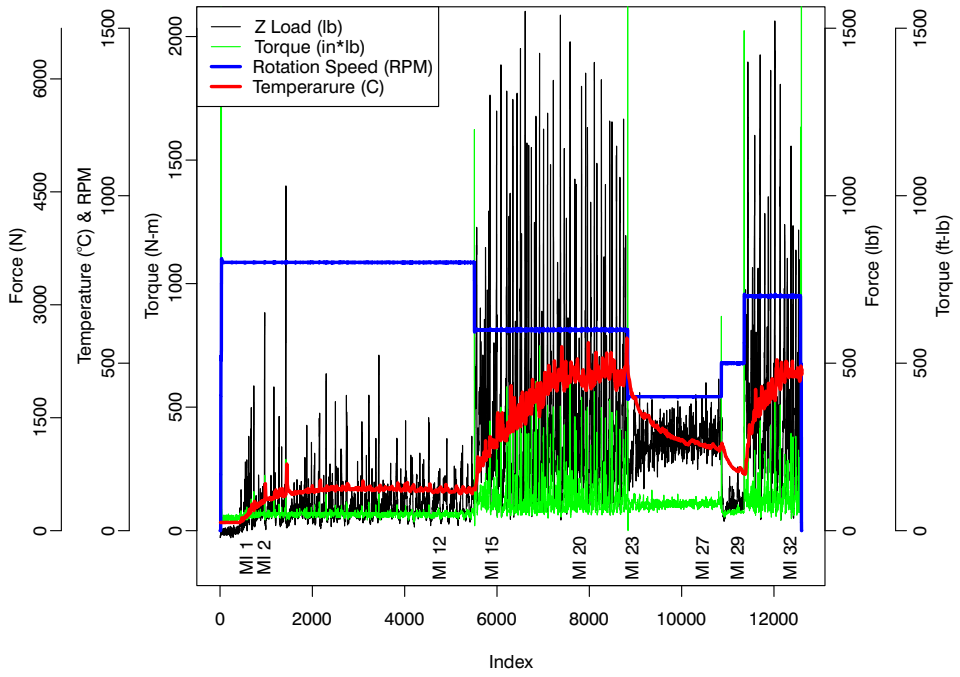

Figure 4.14: Experimental data gathered in a single run.

data from run five at a 10 Hz sample frequency. The vertical axis represents the measured units shown in the legend while the horizontal axis represents an index of each data point in the data file. The most surprising observation about this data is that there are large fluctuations in Z force. In some parts of the experiment, there were fluctuations on the order of 6600 N (1500 pounds). At other times in the experiment, fluctuations were 400 N (100 pounds) or less. The reason this result is surprising is that the machine was run on force control. However if the fluctuations are too fast, the machine would not be able to keep the force constant. The rotational frequencies of this experiment started at 800 RPM, reduced to 600 RPM, reduced again to 400 RPM, increased temporarily to 500 RPM, and ended at 700 RPM. In addition, temperature varied based on frictional heating. There were only a few spots where the time gradient of temperature was less than 20^{o}C per

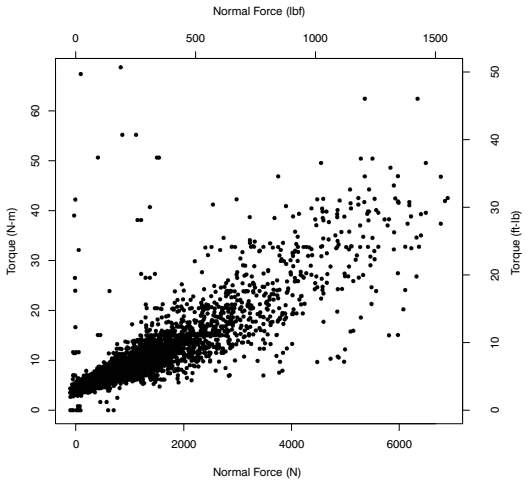

Figure 4.15: Friction preview for data gathered in a single run.

second. The maximum temperature the system reached was about 500^{o}C. However, it seems correlated with Z force.

A quick test was performed to tell if the experiment has valid frictional data. This was done by plotting torque versus normal force, shown in Figure 4.15. This figure shows a lot of noise. Any regression done on this data would lead to very unreliable results. Since the data does not seem to be valid, frictional data analysis was focused on trying to understand the cause of these large fluctuations.

4.5.2 Precession Model

These large fluctuations in forces and visual observations indicate precession was occurring. A precession model was created to determine what evidence would lead us to the conclusion that precession was occurring and if precession was occurring what data would be useable.

To describe the precession, a precession angle and a tool tilt are needed. Figure 4.16 is a pictorial definition of ϕ and β. The precession angle is ϕ and the angle of the tool tilt is β.

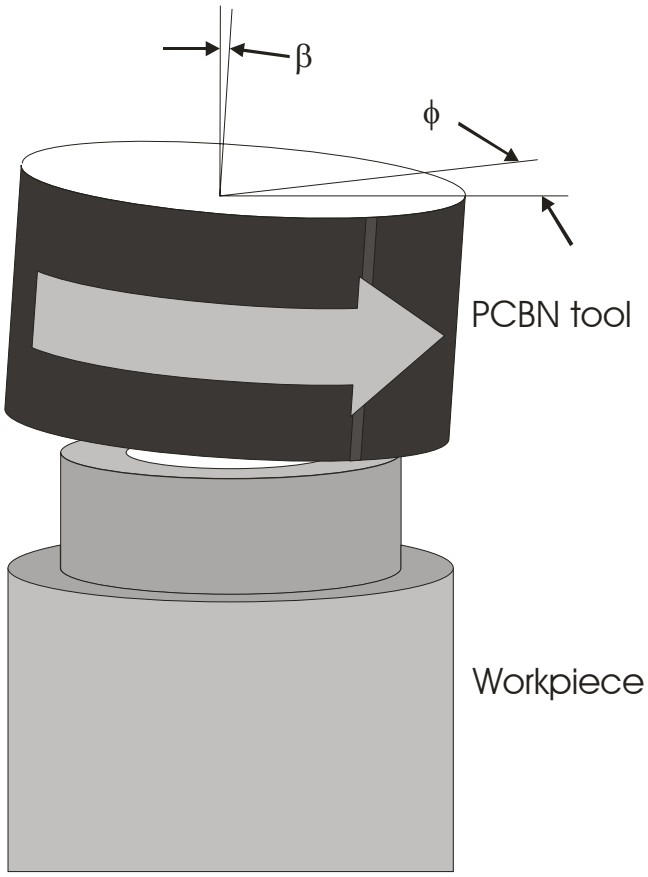

Figure 4.16: Precession model definitions.

When precession is occurring ϕ would be continually increasing. As the tool continually precesses around the workpiece, there would be a component of the force in the same direction as ϕ because the tool would be pushing the workpiece off axis. This would result in sinusoidal X and Y forces where. The magnitude of these forces would be equal in magnitude and 90 degrees out of phase. The model of the forces are shown in Equation 4.18 and 4.19 where $F_{\perp}$ is the magnitude of the

precession force in the X-Y plane and F_x and F_y are the components of the forces in the X and Y direction respectively.

$$F_x = F_\perp cos(\phi) \tag{4.18}$$

$$F_y = F_\perp sin(\phi) = F_\perp cos(\phi + \frac{\pi}{2}) \tag{4.19}$$

Inverting Equations 4.18 and 4.19 result in Equation 4.20.

$$\phi = atan2(F_y, F_x) \tag{4.20}$$

The amount of tool tilt is β. This model is created by assuming that the entire workpiece is in close contact with the tool. This means as the tool tilts, there is enough force to keep the surface of the tool in contact with the workpiece. It is also assumed that the deflection in the workpiece is entirely contained in the concentric cylinder portion of the workpiece. The stress at any given radius on the cylinder is given by Equation 4.21, where E, r, θ , β and l are modulus of elasticity, radius, angle from the positive x direction, tool tilt angle, and length of concentric cylinders respectively.

$$\sigma = \frac{Er \cdot cos(\theta)tan(\beta) + r_o \cdot tan(\beta)}{l} \tag{4.21}$$

Substituting Equation 4.21 into Equation 4.22 and integrating results in Equation 4.23.

$$F_z = 2\int_0^\pi \int_{r_i}^{r_o} \sigma(r, \theta, \beta) r dr d\theta \tag{4.22}$$

$$F_z = \frac{E \cdot tan(\beta)\pi(r_o^3 - r_o ri^2)}{l} \tag{4.23}$$

According to this model the Z force would increase as β increases. Solving for β results in Equation 4.38.

$$\beta = arctan\left(\frac{F_z l}{Etan(\beta)\pi(r_o^3 - r_o ri^2)}\right) \tag{4.24}$$

4.5.3 Implication

There are some significant implications based in this model. One of the most significant implications is that there is not uniform pressure across the surface. There is a potential for both plastic shear deformation friction and Coulomb-Amonton's friction to exist at the same instant on the workpiece interface surface. If the workpiece exhibits both types of friction, analysis of the data would be difficult. To see if this analysis is necessary, the minimum yield strength for 304 stainless steel is compared to the maximum normal pressure and frictional shear. The minimum yield strength for 304 is 206 MPa (30,000 psi) while the maximum normal pressure and frictional shear are 12 MPa (1800 psi) and 5.12 MPa (742 psi) respectively. Based on these numbers, the stainless steel is not yielding if the entire workpiece surface is in contact with the tool. However, there is evidence that the workpiece is yielding. This means that the workpiece surface is not entirely in contact with the tool, which reduces the contact area and increases the normal stress and frictional shear to a point where yielding can occur. Because of the difficulty in doing this and not having data that exhibits plastic shear deformation friction to validate it, this analysis will not be done.

The normal pressure varying across the frictional interface when the interface is entirely Coulomb-Amonton's friction does not influence the value of the coefficient of friction. This is shown by the following derivation. This derivation starts with the normal pressure precession model shown in Equation 4.25 and the normal force where the stress is integrated of the entire area, shown in Equation 4.26.

$$\sigma = \frac{E(rcos(\theta)tan(\beta) + r_o tan(\beta))}{l} + \sigma_{mean} \tag{4.25}$$

$$F = 2\int_0^{\pi}\int_{ri}^{ro} \frac{E(rcos(\theta)tan(\beta) + r_o tan(\beta))}{l} + \sigma_{mean} r dr d\theta \tag{4.26}$$

The evaluation of this integral is shown in Equation 4.27.

$$F = \frac{\pi(Er_o^3 sin(\beta) - Er_o r_i^2 sin(\beta) + \sigma_{mean} r_o^2 lcos(\beta) - \sigma_{mean} r_i^2 lcos(\beta))}{lcos(\beta)} \tag{4.27}$$

Substituting Equation 4.25 into the formula for Coulomb-Amonton's friction, $\tau = \mu\sigma$, results in Equation 4.28.

$$\tau = \mu \left(E \left(\frac{rcos(\theta)tan(\beta) + r_o tan(\beta)}{l} \right) + \sigma_{mean} \right) \tag{4.28}$$

In this Equation τ and μ are the frictional shear stress and the coefficient of friction respectively. The torque would be Equations 4.29 and 4.30 in integral and evaluated forms respectively.

$$T = 2 \int_0^{\pi} \int_{r_i}^{r_o} \tau r^2 dr d\theta \tag{4.29}$$

$$T = \frac{2}{3} \frac{\mu\pi(-Er_o r_i^3 sin(\beta) + Er_o^4 sin(\beta) - \sigma_{mean} lr_i^3 cos(\beta) + \sigma_{mean} lr_o^3 cos(\beta))}{lcos(\beta)} \tag{4.30}$$

Applying Equation 4.27 to Equation 4.14 results in the normal pressure that would be calculated for a given β angle. This is shown in Equation 4.31.

$$\sigma = \frac{\frac{\pi(Er_o^3 sin(\beta) - Er_o r_i^2 sin(\beta) + \sigma_{mean} ro^2 lcos(\beta) - \sigma_{mean} r_i^2 lcos(\beta))}{lcos(\beta)}}{2\pi \left(\frac{ri+ro}{2}\right)(r_o - r_i)} \tag{4.31}$$

Applying Equation 4.30 to Equation 4.11 results in the frictional shear stress that would be calculated for a given beta angle. This is shown in Equation 4.32.

$$\tau = \frac{\frac{2}{3}\frac{\mu\pi(-Er_o r_i^3 sin(\beta) + Er_o^4 sin(\beta) - \sigma_{mean} lr_i^3 cos(\beta) + \sigma_{mean} lr_o^3 cos(\beta))}{lcos(\beta)}}{2\pi \left(\frac{r_i+r_o}{2}\right)^2 (r_o - r_i)} \tag{4.32}$$

To determine the coefficient of friction, μ, Equations 4.31 and 4.32 are substituted into the definition of the coefficient of friction, $\mu = \frac{\tau}{\sigma}$. After some simplification this results in Equation 4.33.

$$\approx \mu = \frac{4(r_o^2 + r_i r_o + r_i^2)}{3(r_i + r_o)^2} \mu \tag{4.33}$$

The μ approximation does not depend on the angle β. It does appear that the approximate coefficient of friction is scaled by a constant that depends on the radii of the concentric cylinders. Redefining the outside diameter to $r_o = r_i + t$ and simplifying the constant results in Equation 4.37. As long as t is small, the constant is approximately 1.0. This shows that the Coulomb-Amonton's coefficient of friction can be approximated by this experiment whether or not there is precession.

$$C = \frac{4r_i^2}{(2r_i+t)^2} + \frac{4r_i t}{(2r_i+t)^2} + \frac{4t^2}{3(2r_i+t)^2} \tag{4.34}$$

$$= \frac{4}{(2+\frac{t}{r_i})^2} + \frac{4\frac{t}{r_i}}{(2+\frac{t}{r_i})^2} + \frac{4\frac{t^2}{ri^2}}{3(2+\frac{t}{r_i})^2} \tag{4.35}$$

$$\approx \frac{4}{(2)^2} \tag{4.36}$$

$$\approx 1 \tag{4.37}$$

4.5.4 Evidences of Precession

Using this precession model evidences of precession are identified in the experiment. The experiment was separated into measurement intervals (MI), each of which represents about a minute's worth of data. The measurement intervals at the bottom of Figure 4.14 label the nine intervals chosen to represent the data set. Since the calculation is the same for each of the MIs, only one is used as an example in this paper, but final results from all MIs will be shown later. MI 20 was chosen because it describes precession the best. Analysis of the precession was done by first, performing a time series analysis of the data, second, frequency analysis of the data, and third applying the precession model to the data.

Figure 4.17 shows one minute of measured data from MI 20. A periodic signal is observed in X, Y, and Z forces and torque. In the case of Z force, the periodic signal increases and suddenly drops. This is evidence that the β angle is also oscillating on this measurement interval. For X and Y forces, there are oscillations around a

mean value. At this magnitude it is difficult to see the details of the oscillations. To further analyze this data, a small subset was chosen. A sample size of 8192 (2^{13}) data points was chosen. This is a little over eight seconds of data. The portion of the data surrounded by the black line in Figure 4.17 is the data selected. Figure 4.18 is a zoomed-in plot of the selected data. At this scale, the X and Y Forces in Figure 4.18 are approximately equal in magnitude. This data were filtered so that only high frequency component is shown. Figure 4.19 shows this filtered data at an even larger scale. At this scale it is evident the two signals that are 90 degrees out of phase with each other; however, the signals do have different magnitudes. The difference in magnitude could be due to precession that is not exactly circular. This could be caused by different stiffness in the machine in the X and Y directions.

In this time series analysis all three evidences of precession are observed, a changing Z force, X-Y forces are relatively equal in magnitude, and X-Y force signals are 90 degrees out of phase from one another.

A frequency analysis was performed using the csd function in MATLAB. The same sample of 8192 (2^{13}) data points shown in Figure 4.18 was used for this function. The data were filtered so only the high frequency component of the signal remained and the low frequency signals would not influence the FFT. A hamming window of 2048 data points is used, where each window overlapped 512 data points in the FFT. This gives a resolution of 0.49 Hz in the frequency spectrum. Figure 4.20 shows the frequency content of the forces measured with the load cells. The frequencies that exhibit the strongest power of the load cell data signal are consistently located less than 30 Hz. A better view of this frequency spectrum is shown in Figure 4.21. This figure shows the normalized frequency power for the load cell signal in the range from 0 to 30 Hz. The load cell signal only has a few dominant

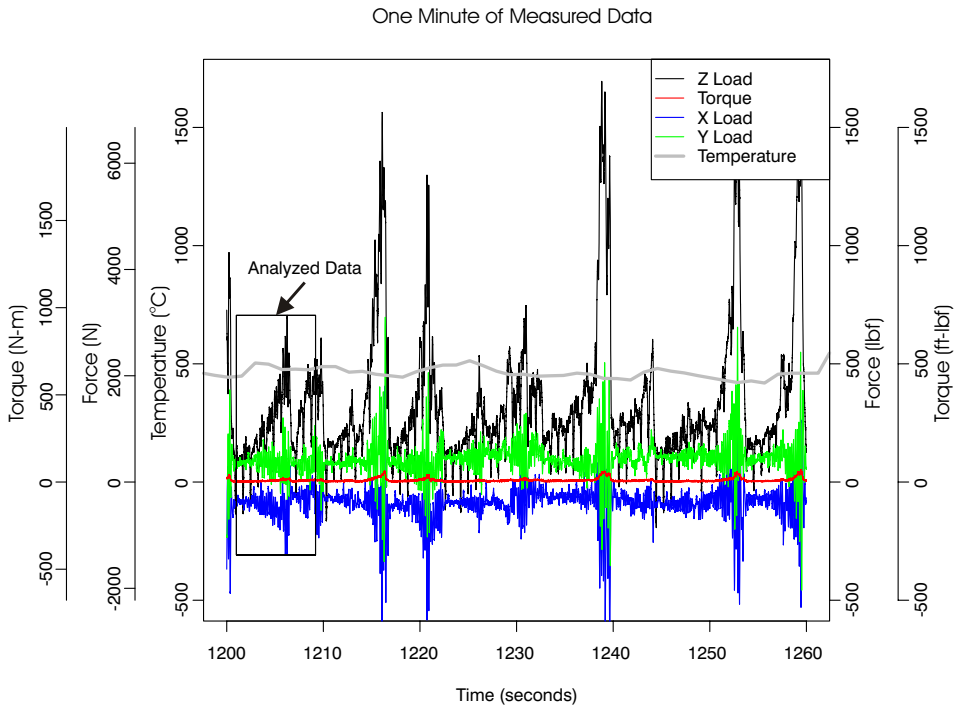

Figure 4.17. Data from MI 20. The black box surrounds the portion of the data used in a closer examination of data.

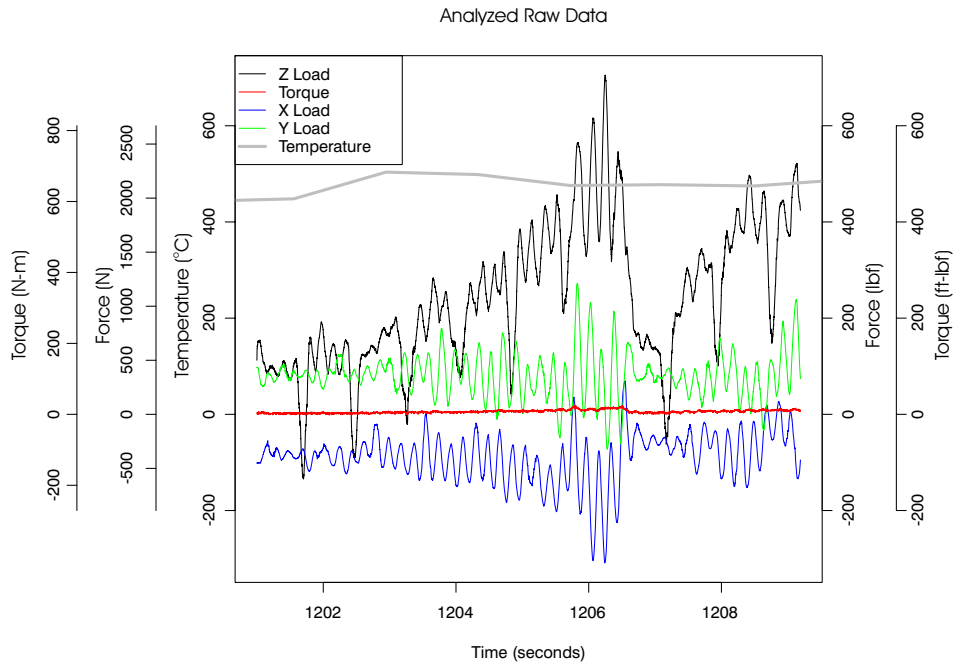

Figure 4.18: Interval 20 is the boxed region from Figure 4.17.

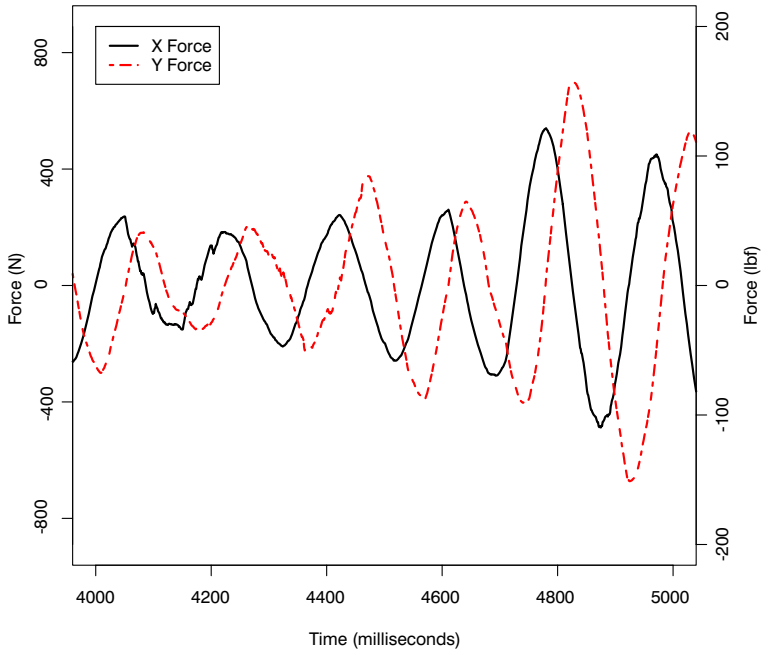

Figure 4.19: High pass filtered X Y load cell signal for MI 20.

frequencies. The Z load signal has a dominant frequency around 2.5 Hz. This observation is consistent with all the MI. This means that the β is oscillating with a frequency of 2.5Hz. In addition, the X and Y load frequency spectra are very similar as expected for precession. In Figure 4.21 the X and Y signals' frequency spectra are difficult to distinguish. This correlation between X and Y force signals was investigated by measuring coherence. Figure 4.22 shows the coherence between X, Y, and Z load cell signal measurement taken two at a time. X and Y load signal coherence is above 0.9 for a range on frequencies between 1 and 7 Hz. At these frequencies the phase angle between X and Y is about 88 degrees, which is consistent with Equation 4.18 and 4.19.

Because evidence of precession has been found for MI20, the precession model is applied to the data. The X and Y forces were filtered to leave the high frequency component of the data and Equation 4.20 is used to determine ϕ. Figure 4.23 shows

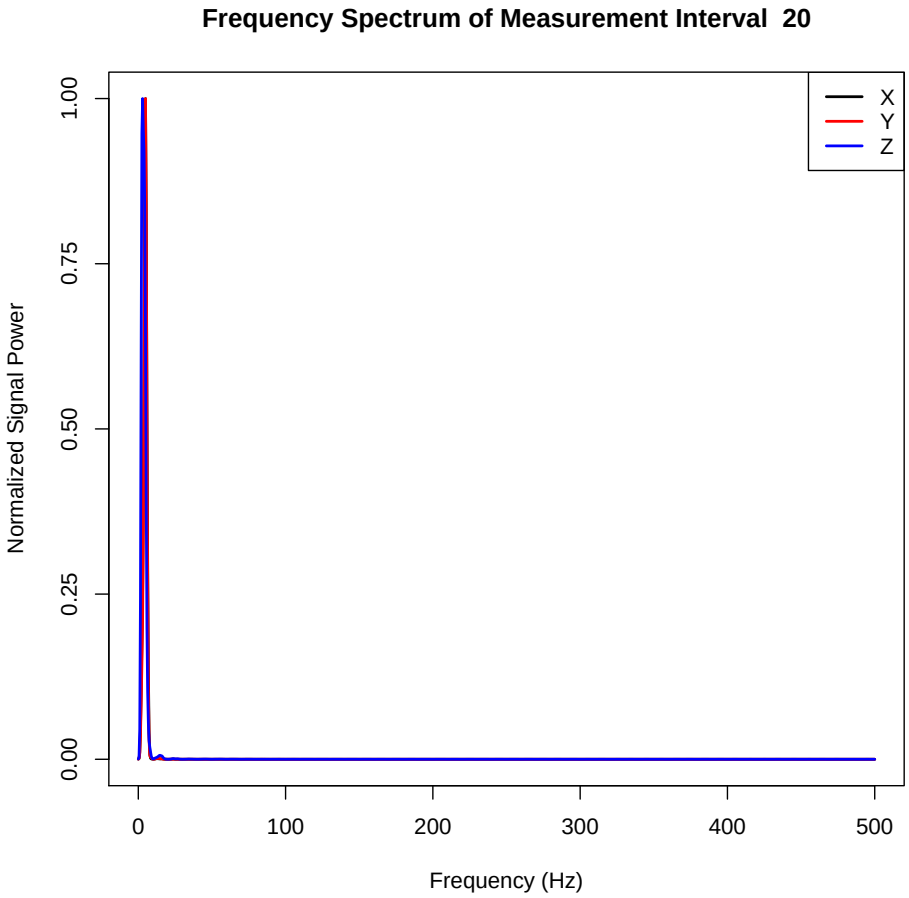

Figure 4.20: Load cell signal frequency spectrum.

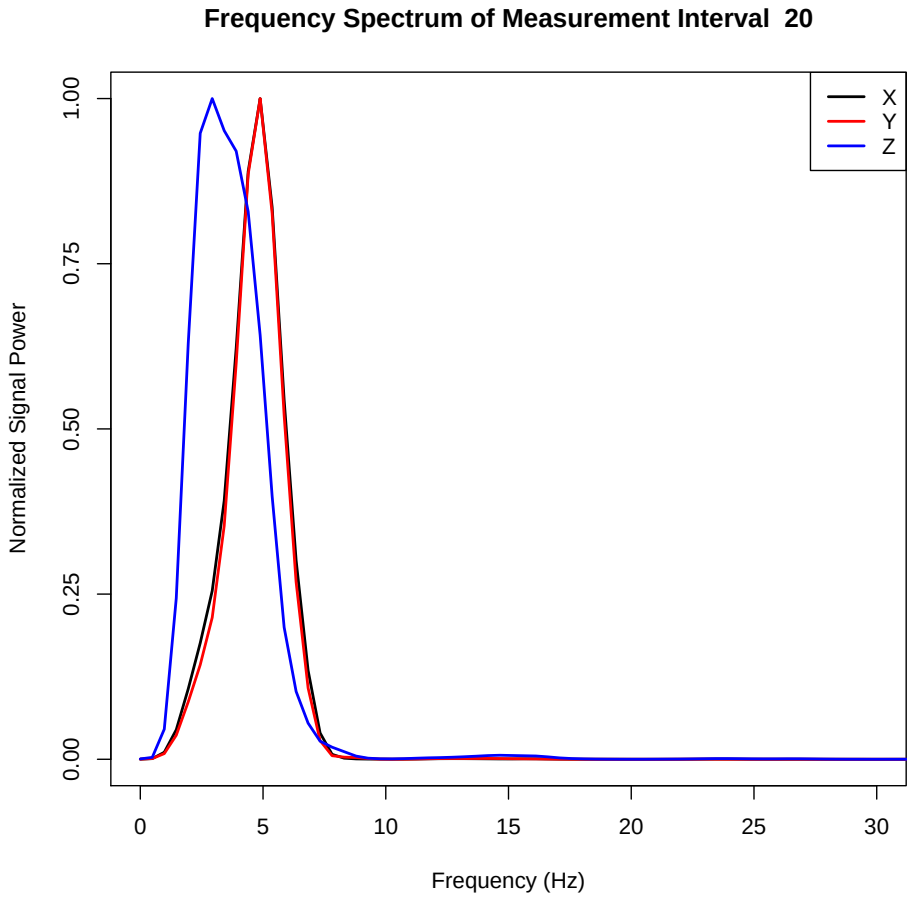

Figure 4.21: Load cell signal frequency spectrum from 0 to 30 Hz.

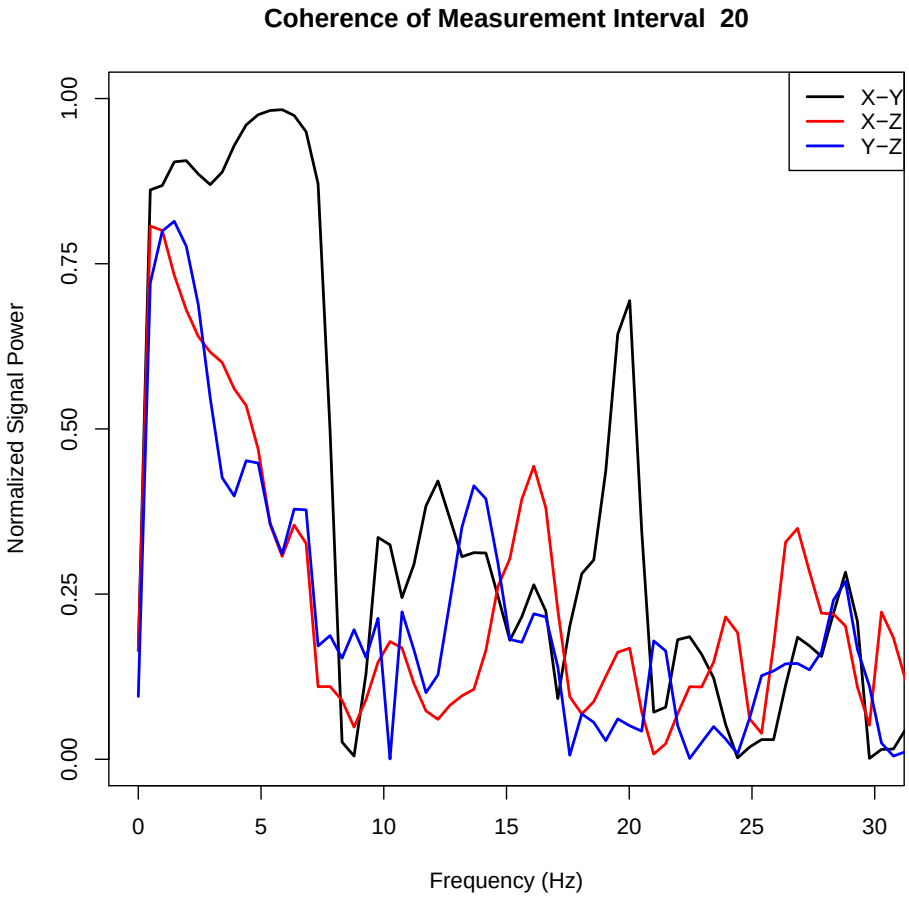

Figure 4.22: Frequency spectrum of the measurement made with the load cell.

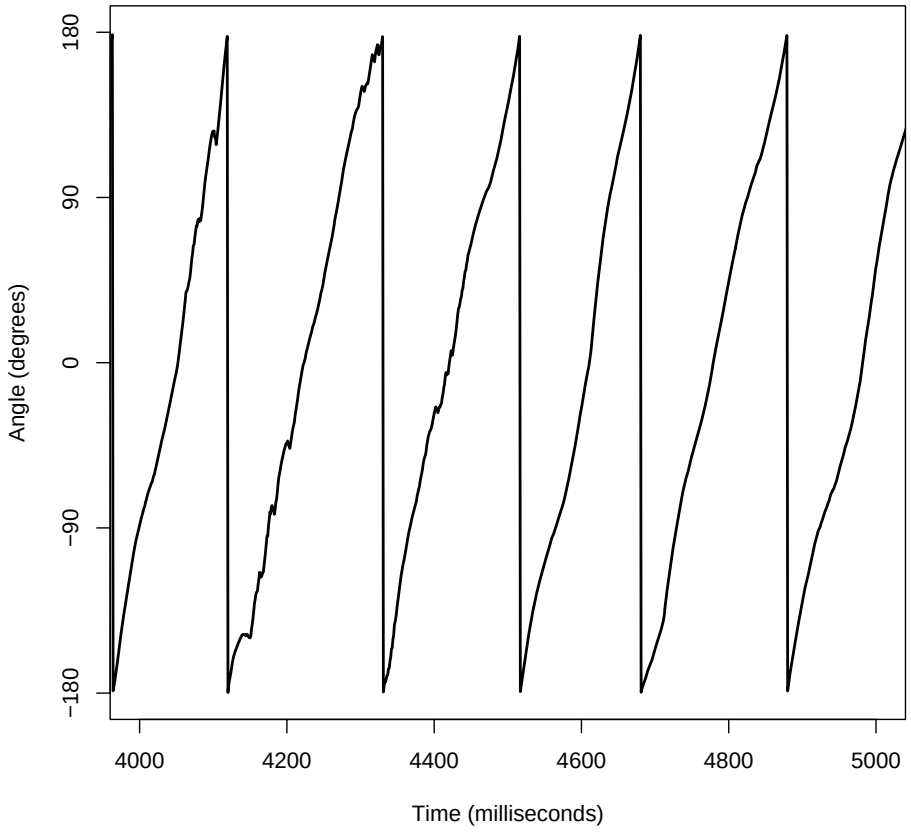

Figure 4.23: Phi precession angle for MI 20.

the ϕ angle for MI 20. This figure shows a ϕ that is continually increasing. This observation is what is expected in precession.

A high pass filter was also used on Z force. Using this filtered force and Equation 4.38 the β is calculated Figure 4.24 shows the calculated β for MI 20.

$$\beta = arctan\left(\frac{Fl}{Etan(\beta)\pi(r_o^3 - r_o ri^2)}\right) \tag{4.38}$$

Using these ϕ and β calculations, the precession path of the center of the tool projected on the X-Y plane throughout the measurement interval is calculated. The

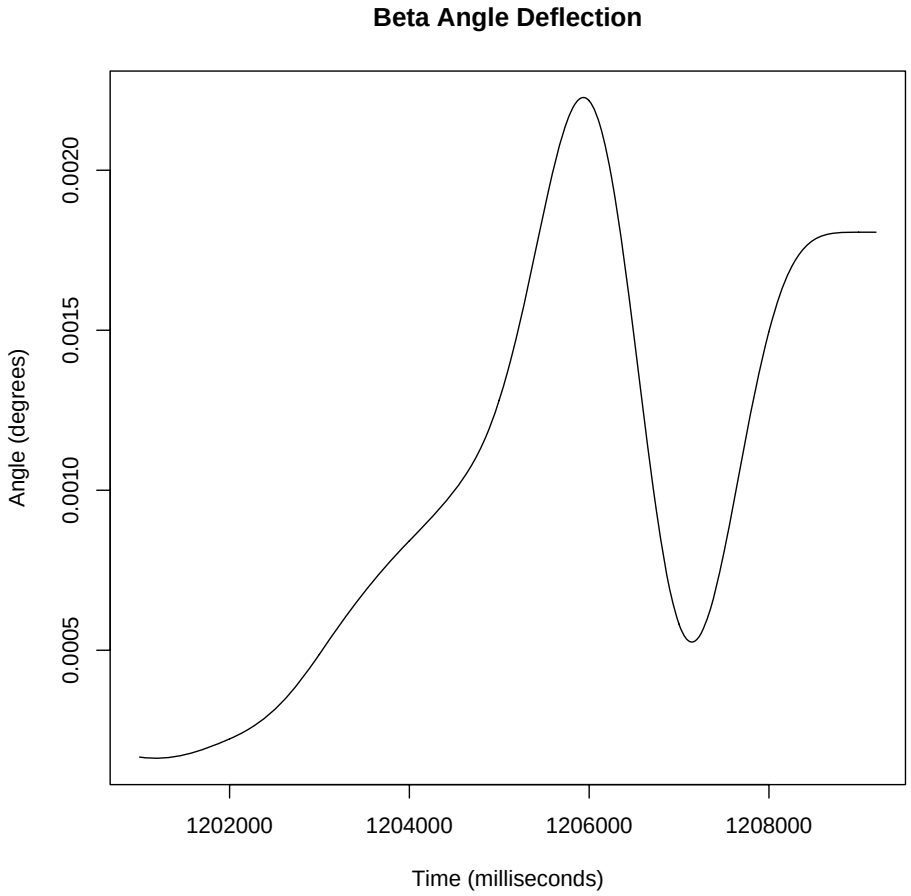

Figure 4.24: Beta precession angle for MI 20.

precession pattern is plotted in Figure 4.25. Note that the path is largely circular, but there appears to be a spiraling component as well. This is consistent with oscillatory β.

4.5.5 Measurement Interval Comparison

The analysis of section 4.55 was applied to each of the 9 MIs selected for analysis. Although they share some common features, there are also significant differences in this section we compare the various MIs.

Time Series Data

Unlike MI 20, MIs 1 and 29 do not show strong precession evidence int a time series analysis. MI 1 and 29 are shown in Figures 4.26 and 4.27.

MI 1 and 29 show signals that are about 180 degrees out of phase at for part of the time and be in phase at another point in time. This does not agree with the precession model. However, the amplitudes of these signals are small and precession is weak.

Coherence Data

The coherence spectra are compared by using Table 4.1. This table shows frequencies from the various MI that have high X-Y coherence. A full listing of five frequencies in each MI with the highest coherence is found in Appendix D. Those MIs where the coherence is high, above 0.9, and have a phase shift near 90 degrees are measurement intervals 15, 20, and 32. MI 1, 2, 12, 15, 29, and 32 have dominant frequencies less than 8 Hz. However, measurement intervals 23 and 27 have dominant correlated frequencies between 50 and 75 Hz.

In an attempt to determine what causes the high correlation between X and Y load cell signals, the coherence spectrum from all the MIs is plotted against the spindle frequency shown in Figure 4.28. Some MI's coherence spectrums could

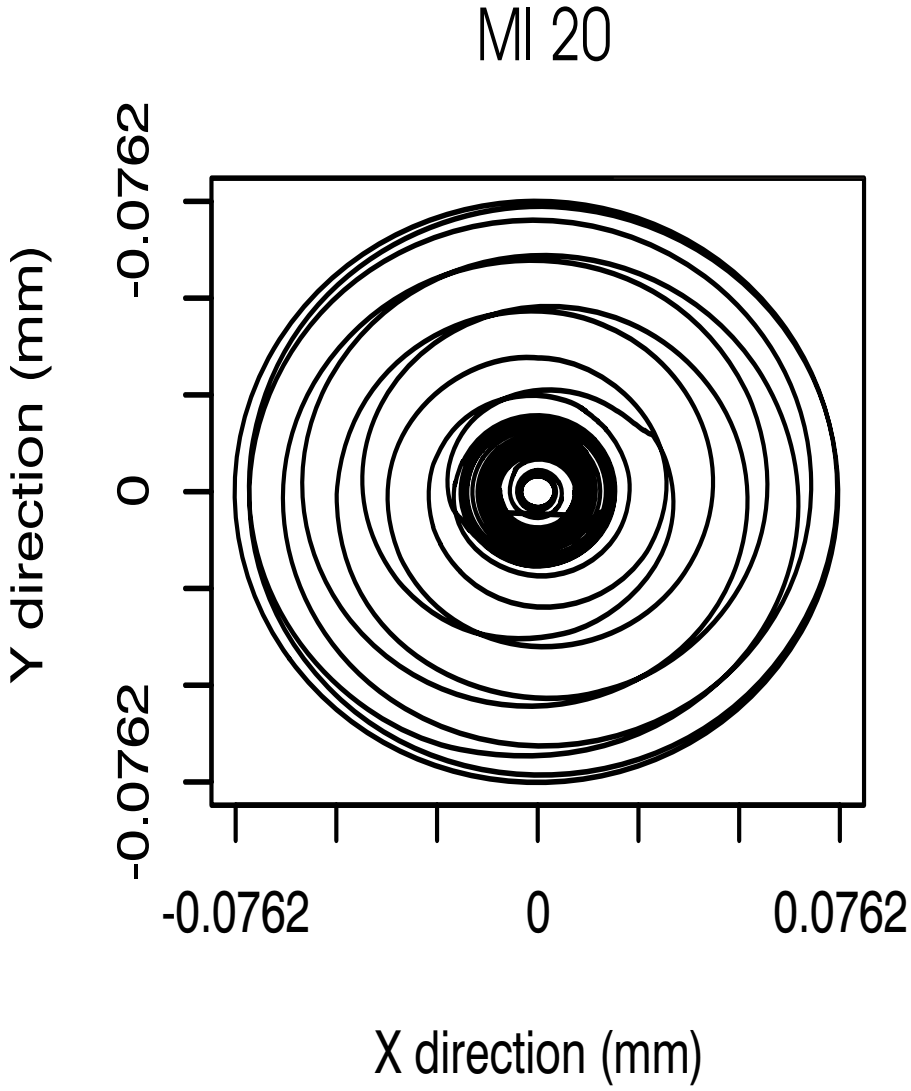

Figure 4.25: Precession model for MI 20.

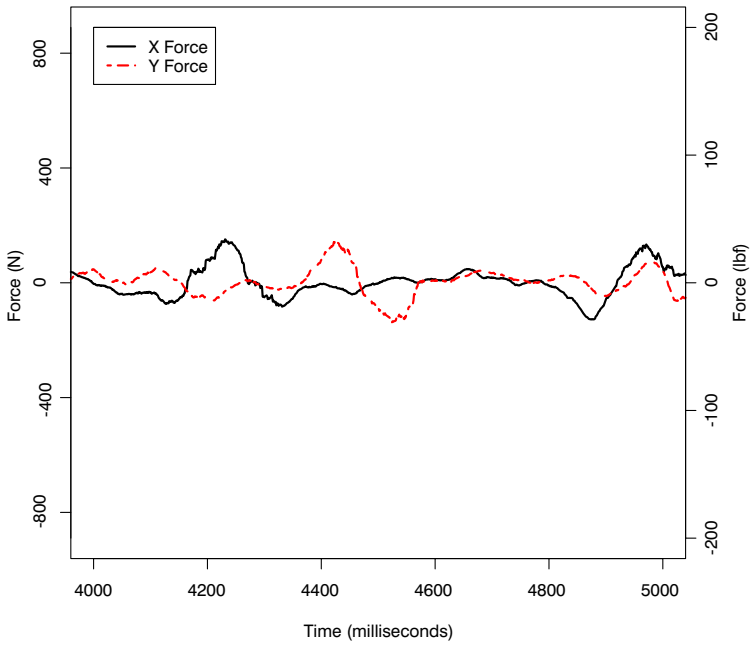

Figure 4.26: High pass filtered X Y load cell signal for MI 1.

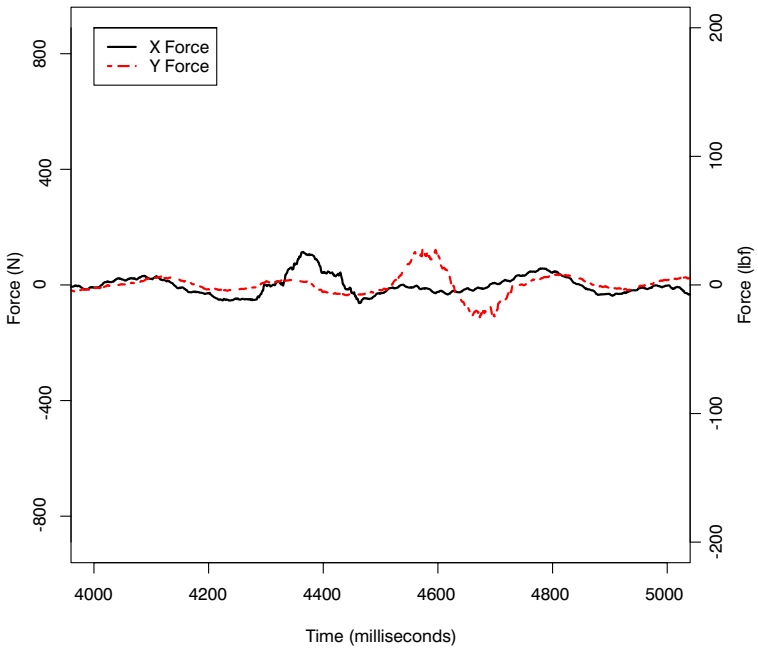

Figure 4.27: High pass filtered X Y load cell signal for MI 29.

Table 4.1: Average top coherent frequencies for each MI.

MI	Frequency	Coherence	Phase
MI 1	7.08	0.73	83
MI 2	4.64	0.54	140
MI 12	3.29	0.45	144
MI 15	5.37	0.97	93
MI 20	5.37	0.97	88
MI 20	4.64	0.97	85
MI 23	73.73	0.66	71
MI 23	47.37	0.63	-143
MI 27	74.71	0.68	60
MI 27	48.58	0.65	-153
MI 29	1.95	0.6	134
MI 32	6.35	0.93	96

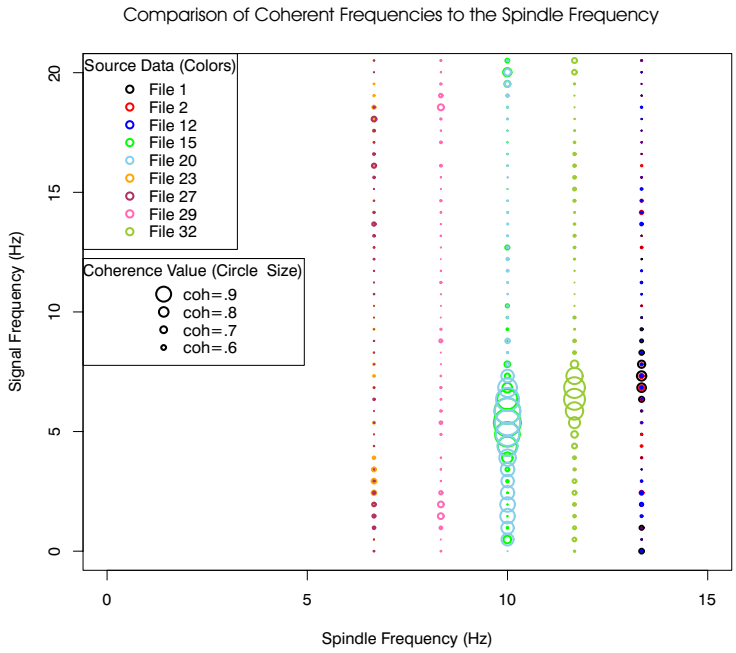

Figure 4.28: Coherence of the X Y load cell signal related to spindle rotation.

have dominant frequencies about half the spindle frequency. This hypothesis is not validated because this relationship does not account for all the dominant coherent frequencies.

A more likely explanation is that certain spindle frequencies excite resonances in the system which cause the dynamic precession of machine. The spindle speeds nearer 600 RPM (10 Hz) and 700 RPM (11.7 Hz) are associated with high coherence. Measurement intervals 15, 20, and 32 have 600, 600, and 700 RPM respectively. As the spindle frequency moves away from this region, precession is less significant.

Maximum Tool Tilt Angle

Figure 4.29 shows the maximum angle of the tool tilt during that measurement interval. The angle of tool tilt is the angle that the tool deviates from the spindle axis. MIs 15, 20 and 32 again show that the maximum precession angle is higher, around 10 and 11.7 Hz.

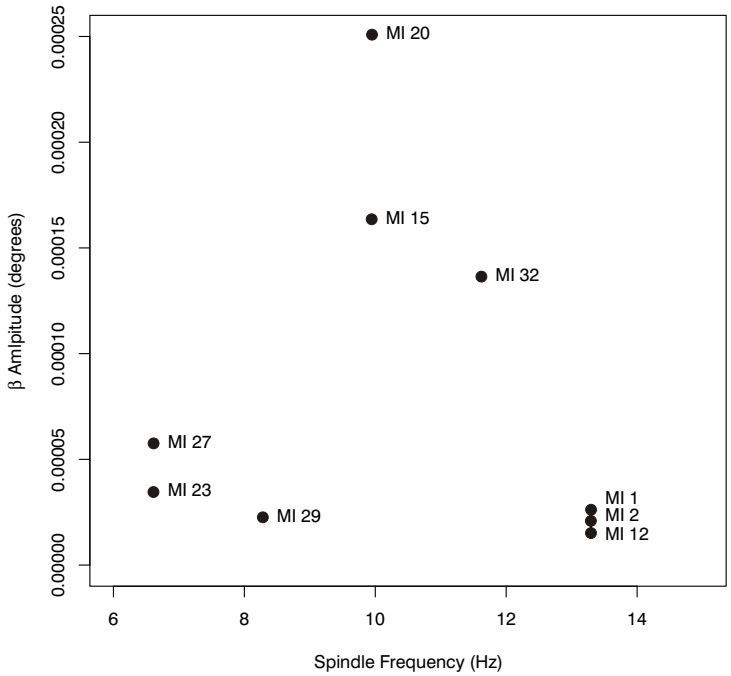

Figure 4.29: The maximum angle of precession at various spindle frequencies.

Precession Paths

The different precession patterns can be seen by plotting the path of the center point of the tool. Using Equations 4.20 and 4.38 and data from each MI, the precession pattern is plotted in Figure 4.30. Figure 4.30 represents a path of the center of the tool projected on the X-Y plane throughout the measurement interval. All measurement intervals exhibit precession. There are tree types of precession. The first type of precession has a small β angle. This type of precession can be seen in MI 1 and 2. The second type of precession is is an unstable precession. This type of precession has relatively large fluctuations in the β angle with time. MI 15, 20, and 32 show this type of precession. The third type of precession is a constant β angle. This type of precession can be seen in MI 12, 32, 27, 29.

4.5.6 Frictional Quantities

Some of the assumptions used in the precession model are not accurate to what is happening in this experiment. The command force for all these experiments is 2240 N (500 lbf) or less. However, because of the precession of the tool, some of the measured forces were 4000 N (1000 lbf) higher than that, especially for MI 20. There is a good chance that some portion of the tool is not in contact with the workpiece. This prevents stress based friction calculations because there is no measurable apparent contact area, but force based friction can be calculated.

After analyzing the precession in the signal and filtering the data with a low pass filter, an attempt was made to identify usable data and meaningful relationships by converting the data to frictional quantities. Figure 4.31 shows the relation between frictional shear and normal pressure. The relation between frictional shear and normal pressure appears linear. All the data seems to be related to normal pres-

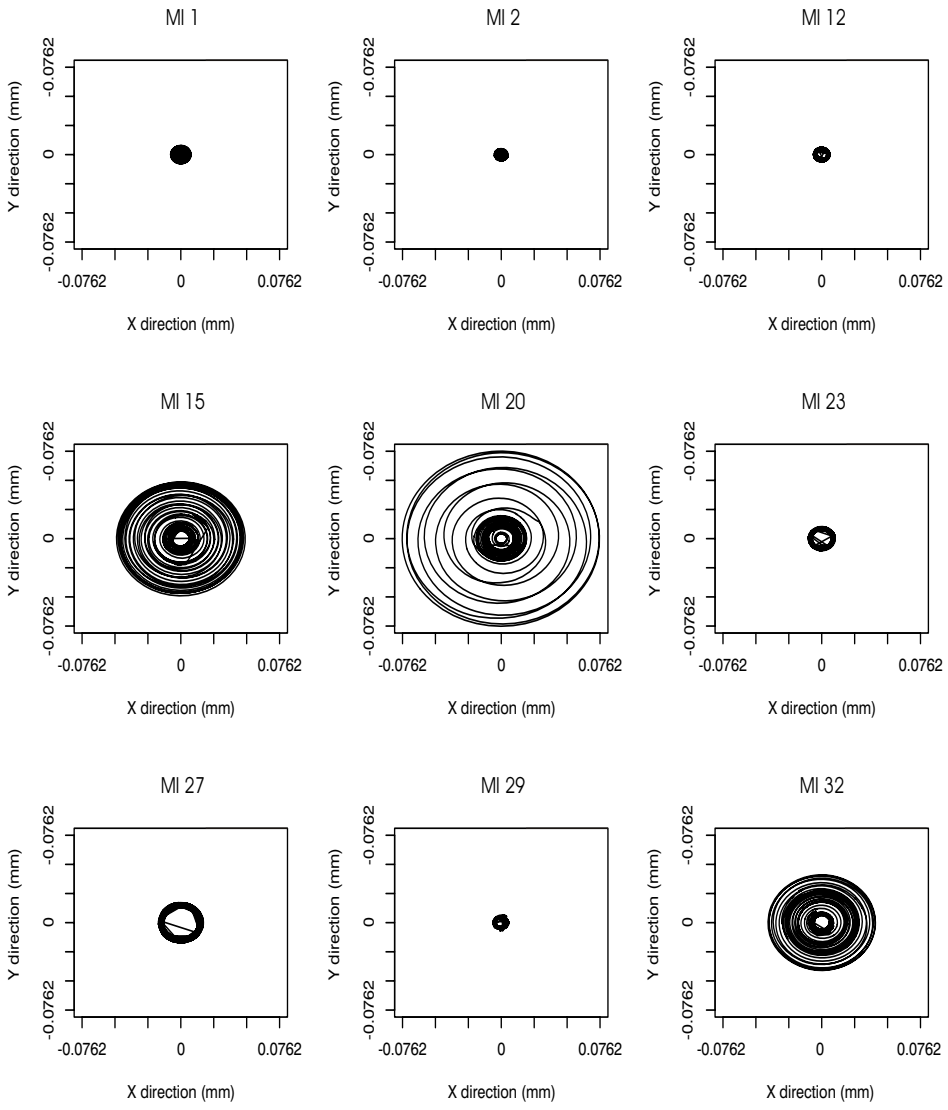

Figure 4.30: Precession model for each MI.

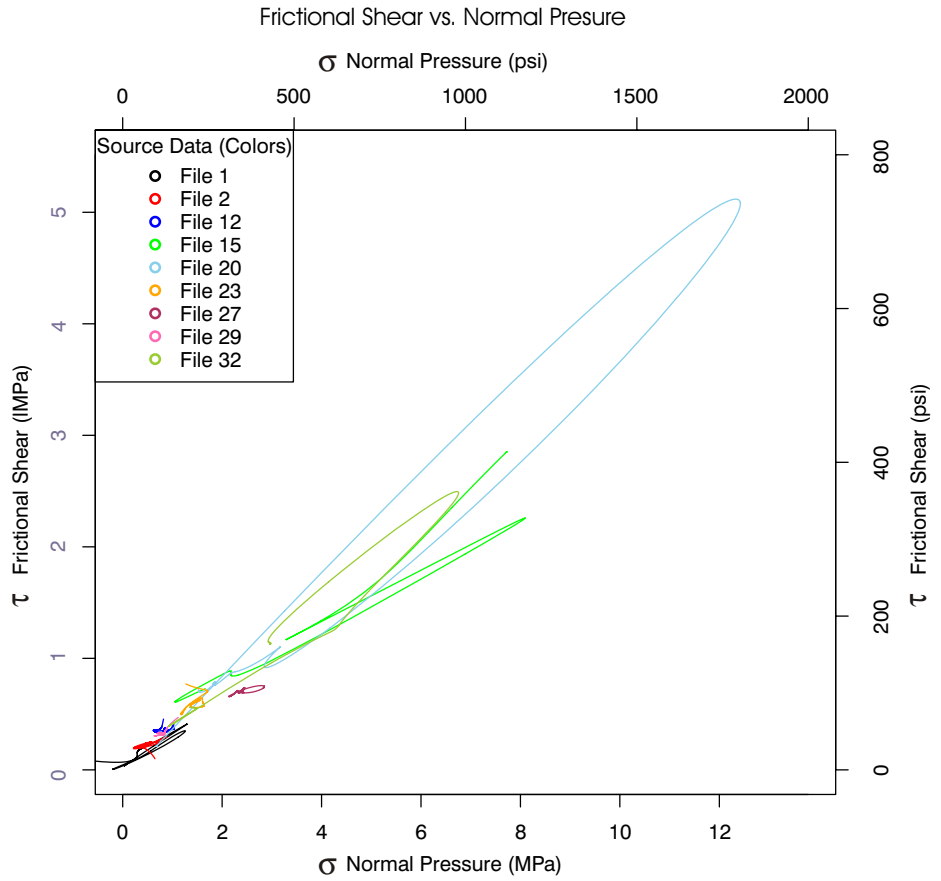

Figure 4.31: High pass filtered frictional shear and normal pressure.

sure, which means there is no data that exhibits plastic shear deformation friction characteristics.

Another observation is that the coefficient of friction is not significantly affected by temperature, as shown in Figure 4.32. The large fluctuations in the coefficient of friction for temperatures lower than 150°C is likely caused by error in frictional measurement and low normal pressure measurement. Any error in measurement is amplified when forces are low, because the normal pressure is in the denominator of the fraction, $\mu = \frac{frictionalshear}{normalpressure}$. It is also interesting to note that at temperatures

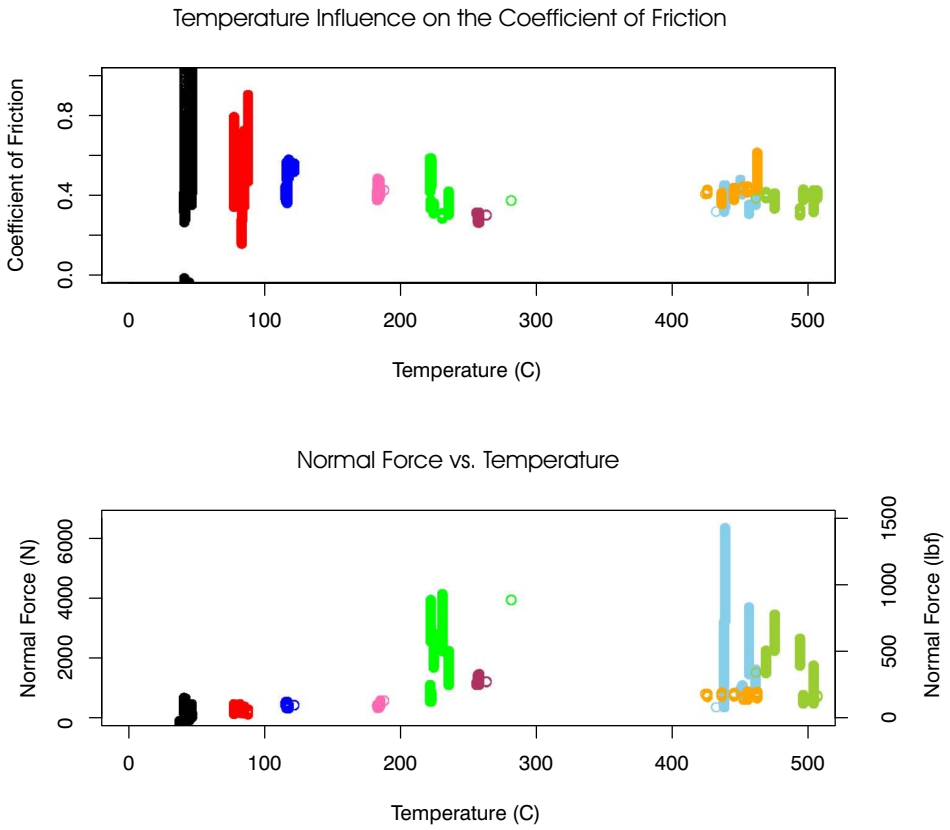

Figure 4.32: Temperatures influence on the coefficient of friction

greater than 400^{o}C there is a large range of normal force values measured, yet the coefficient of friction remains relatively constant around 0.4.

4.6 Recommendations and Conclusions

One of the main objectives of this work is to evaluate cylinder on disk method of measuring both Coulomb-Amonton's and plastic shear deformation friction. This method is not appropriate to measure both Coulomb-Amonton's and plastic shear deformation friction. The main reason that this method is inappropriate is that precession occurs. Unexpected precession was observed which appears to be caused by unbalanced forces, and is largest at resonant frequencies of the machine. Due to precession of the tool, plastic shear deformation friction cannot be calculated because of nonuniform normal pressure. Spindle frequencies between 10 and 12 Hz exhibited precession with dynamic tilt angle. All measurement intervals showed a tilt angle frequency of about 2.5 Hz. Coulomb-Amonton's friction can be measured with this method because the actual area is not important to the calculation . Coulomb-Amonton's friction appears to be about 0.4 at higher forces. Future work should address the problem of precession and determine a suitable way to measure friction. Future experiments should increase the maximum normal pressure so that interface exhibits plastic shear deformation friction. In addition, future work should use a designed experiment to determine if temperature, velocity, and normal pressure influence the frictional interface between PCBN and stainless steel.

5 Conclusions and Recommendations for Future Work

A friction measuring mechanism is used to measure the frictional force at a variety of temperatures, velocities, and normal forces for the PCBN–1018 steel interface. Significant factors influencing the frictional force are identified. Temperature, velocity, and normal force are all significant factors.

The coefficient of friction between these materials is about 0.35 at temperatures less than 200^{o}C, while around 550^{o}C and 1.93 m/s (380 SFM) the coefficient of friction decreases to about 0.2. The coefficient of friction around 550^{o}C and 0.40 m/s (78 SFM) is about 0.8. The plastic shear deformation plateau is about 979 N (220 lbf.) at 550^{o}C and .40 m/s (78 SFM), while it is 222 N (50 lbf.) at 550^{o}C and 1.93 m/s (380 SFM).

A statistical model describing the frictional behavior of the PCBN–1018 steel interface was developed that has a good correlation with measured data. This model is the minimum of two linear models with interactions. These linear models represent the two types of friction. One model represents the Coulomb-Amonton's portion of the data. The other model represents the plastic shear deformation friction. The regression technique worked well and had a correlation of 1.0445 and an R^2 value of 0.83.

A friction measuring mechanism is used to measure the frictional shear of the PCBN-stainless steel interface at a variety of temperatures, velocities, and normal pressures. Coulomb-Amonton's friction can be measured with this method for relatively high normal forces. Coulomb-Amonton's friction appears to be about 0.4 for

higher forces. Precession was observed which appears to be caused by a resonance in the machine. However, valid plastic shear deformation friction measurements cannot be measured because there is not a uniform normal pressure.

Based upon the results of the previous three chapters, it is recommended that the following work be performed:

- Develop a method of measuring frictional quantities over a large range of temperatures, velocities, and normal pressures that has a measurable contact area and has a uniform normal pressure.
- Develop and perform an experimental plan to measure frictional shear over a variety of conditions.
- Create a model that represents the data.

References

[1] S. M. Packer, T. W. Nelson, and C. D. Sorensen. Tool and equipment requirements for friction stir welding ferrous and other high melting temperature alloys. In *Proceedings of the 3rd International Symposium on Friction Stir Welding*, Kobe, Japan, 27–28 September 2001.

[2] K. Yoshikawa. A joining criterion for lap joining of dissimilar metal materials of aluminum and stainless steel by friction stir. In *Proceedings of the 4th International Symposium on Friction Stir Welding*, Park City. Utah, May 2003.

[3] TWI Website. Friction stir welding, 2003. Technology File http://www.twi.co.uk/j32k/unprotected/band_1/tffricst.html.

[4] M. Zahedul, H. Khandkar, and J. A. Khan. Thermal modeling of overlap friction stir welding for al-alloys. *International Journal of Machine Tools and Manufacture*, 10:91–105, 2001.

[5] T. U. Seidel and A. P. Reynolds. Two-dimensional friction stir welding process model based on fluid mechanics. *Science and Technology of Welding and Joining*, 8(3):175–183, 2003.

[6] M. Song and R. Kovacevic. A coupled heat-transfer model for workpiece and tool in friction stir welding. In *Proceedings of the 4th International Symposium on Friction Stir Welding*, Park City. Utah, May 2003.

[7] ϕ. Frigaard, ϕ. Grong, and O. T. Midling. A process model for friction stir welding of age hardening allumunum alloys. *Metallurgical and Materials Transactions A Physical Metallurgy and Materials Science*, 32A:1189–2000, 2001.

[8] P. Dong, F. Lu, J. K. Hong, and Z. Cao. Coupled thermomechanical analysis of friction stir welding process using simplified models. *Science and Technology of Welding and Joining*, 6:281–287, 2001.

[9] C. M. Chen and R. Kovacevic. Finite element modeling of friction stir weldingthermal and thermomechanical analysis. *International Journal of Machine Tools and Manufacture*, 43:1319–1326, 2003.

[10] M. C. Shaw. The role of friction in the deformation processing. *Wear*, 6:140–158, 1963.

[11] K. Maekawa, A. Kubo, and T.H.C. Childs. A friction model for free-machining steels and its applicability to machinability analysis. *Key Engineering Materials*, 196:79–90, 2001.

[12] D. Stratton and C. Sorensen. Characterizing the frictional interface between pcbn and 1018 steel for friction stir welding numerical models. In *Computational Methods and Experiments in Materials Characterisation II*, Portland, Main, November 2005.

[13] D. Stratton. Private communication, 2004. Brigham Young University.

[14] D. Stratton. Private communication, 2003. Brigham Young University.

[15] D. Eggett, C. Sorensen, N. Stephens, and D. Stratton. Private communication, 2004. Brigham Young University.

[16] D. Eggett and N. Stephens. Private communication, 2004. Brigham Young University.

APPENDIX

Appendix A: Possible Models for Frictional Interface

A.1 Goals of the Model

The model developed from this data has engineering applications and needs to be a valid statistical model. Engineers value models that relate to physical quantities and that are interpretable. In addition, regression quality, regression robustness, and model simplicity are important. Yet, the model needs to describe the data sufficently. Model evaluation was based on these ideas. The model is evaluated based on these criteria:

- Interpretability
- Number of coefficients
- Robust method of determining coefficients

The model form needs to be interpretable because engineers will be using this model. In addition,the model needs to represent physical phenomena. The model also needs to be as simple as possible. As complexity increases, there is a greater chance that the model will represent noise instead of signal. Furthermore, as the complexity of the model increases, the difficulty in determining coefficients also increases.

In addition, there needs to be a robust method of determining coefficients. Robust method of determining coefficients refers to the regression will produce a good answer regardless of the *a priori* guess of the coefficients. The closer that the *a priori* guess has to be to the actual value in order for the model to converge, the more cumbersome the model becomes and produces a less reliable answer.

A.2 Possible Model Forms

The obvious model choice would be to take the Maekawa et al. [11] model and add temperature and velocity terms to each of the terms that could be dependent on temperature and velocity. Equation A.1 shows the resulting model.

$$\tau_t = k(T,V) \cdot [1 - e^{\{-(\frac{\mu(T,V)\sigma_t}{k(T,V)})^{n'(T,V)}\}}]^{\frac{1}{n'(T,V)}}. \tag{A.1}$$

This model is very interpretable and appropriate because it builds on previous work. The $\mu(T,V)$ represents the coefficient of friction and the $k(T,V)$ represents the plastic flow shear stress. Both of these quantities are related to physical phenomena that engineers understand. However there are twelve coefficients. In addition, the

model does not have a robust method of determining coefficients because the model includes powers and fractions.

Another possible model was proposed by Stratton [14], shown in Equation A.2.

$$F_f = \frac{F_n}{M(T,V) + L(T,V)F_n} \tag{A.2}$$

Where M and L relate to physical phenomena. M relates to the coefficient of friction shown in Equation A.3.

$$\mu = \frac{1}{M(T,V)} \tag{A.3}$$

The coefficient of friction, μ, is the inverse of $M(T,V)$. In addition, L relates to the plastic shear deformation friction value shown in Equation A.4.

$$F_p = \frac{1}{L(T,V)} \tag{A.4}$$

This model is interpretable, and it has eight coefficients to estimate. However, the methods needed to determine the coefficients need some reasonable initial guesses of coefficients. The initial guesses are not difficult to estimate from the data through a method similar to a factorial experiment. This model for the purpose of this paper will be classified as semi-robust. This model converges.

Another model proposed by Eggett et al. [15] is shown in Equation A.5, where α is shown in Equation A.6.

$$\mu_{eff} = \alpha\mu_c(T,V) + \frac{(1-\alpha)\mu p, eff(T,V)}{F_n} \tag{A.5}$$

$$\alpha = \frac{e^{\Omega(T,V)}}{1 + \Omega(T,V)} \tag{A.6}$$

This model represents the transition between two coefficients of friction. The plastic shear deformation friction is represented here as an effective coefficient of friction. This model is interpretable. However, the model has twelve coefficients and it is not robust. This model did not converge.

Another model proposed by Eggett et al. [16] is shown in Equation A.7 where α is the same as in Equation A.6.

$$\mu_{eff} = \alpha\gamma_l(T,V) \tag{A.7}$$

This model is not interpretable because it does not relate to any physical phenomena. This model has eight coefficients and is robust. This model did converge.

Stratton [13] proposed two linear statistical models shown in Equation A.8 and A.9. The frictional force would be the minimum of the two models shown in Equation A.10.

$$F_c = (\beta_{c1} + \beta_{c2}T + \beta_{c3}V + \beta_{c4}TV)F_n. \tag{A.8}$$

$$F_p = \beta_{p1} + \beta_{p2}T + \beta_{p3}V + \beta_{p4}TV. \tag{A.9}$$

$$F_f = min(F_c, F_p). \tag{A.10}$$

This model fits all the criteria. This model is interpretable, it has eight coefficients to estimate, and it is robust. This model would use linear statistical techniques to determine the coefficients. However there are no statistical methods to determine coefficients of two linear models on one data set. To solve this problem, membership function regression was developed. Using the developed method the regression did converge.

Appendix B: Membership Function Regression

This program was written in R v 2.3.1

```
MF<-function(Fn,Ff,V,T,NoI,filename){

"start"
 Matrix<-matrix(0,NoI,44) Fn<-Fn V<-V T<-T

ii=1
mean_mu=.75
mean_L=.75
X_spread=.04
ni=40
spread_mu=200
spread_L=200
X_spread<-X_spread
flag<-0
flag2<-0
flag3<-0
ifianal=0

# there are the parameters to define the cutoff
spread_mu<-spread_mu mean_mu<-mean_mu

spread_L<-spread_L mean_L<-mean_L

while(ii<(NoI+1)){

rand<-rnorm(length(V),0,100)

LV<-ifelse(V<=100,1,0) HV<-ifelse(V>=275,1,0) MV<-(1-LV-HV)

V_div<-LV*1+HV*3+MV*2 V_factor<-factor(V_div)

RLV<-ifelse(rand<median(split(rand,LV)[[2]]),1,0)*LV
RMV<-ifelse(rand<median(split(rand,MV)[[2]]),1,0)*MV
RHV<-ifelse(rand<median(split(rand,HV)[[2]]),1,0)*HV

#subset<-RLV+RMV+RHV subset<-c(1:length(Fn))
```

```
subset<-subset/subset

n<-length(split(subset,ifelse(subset==0,0,1))[[1]])

w<-c(1:length(Fn)) w<-w/w

#"LM" # This creates a linear model of the data.
CM<-lm(Ff~(T*V_factor):Fn+Fn-1,weight=w*subset)

#Stores the results for next iteration

mu__ave<-ifelse(is.na(CM[[1]][[1]]),0,CM[[1]][[1]])

mu__T  <- ifelse(is.na(CM[[1]][[2]]),0,CM[[1]][[2]])

mu_LV  <- ifelse(is.na(CM[[1]][[3]]),0,CM[[1]][[3]])

mu_MV  <- ifelse(is.na(CM[[1]][[4]]),1,CM[[1]][[4]])

mu_HV  <- ifelse(is.na(CM[[1]][[5]]),0,CM[[1]][[5]])

mu_TMV <- ifelse(is.na(CM[[1]][[6]]),0,CM[[1]][[6]])

mu_THV <- ifelse(is.na(CM[[1]][[7]]),0,CM[[1]][[7]])


#Creates a Limiting Force Linear model
LFM<-lm(Ff~T*V_factor,weight=w*subset)

#Stores results for next iteration #

L__ave<- ifelse(is.na(LFM[[1]][[1]]),0,LFM[[1]][[1]])

L__ave<-c(1:length(V))/c(1:length(V))

L__T  <- ifelse(is.na(LFM[[1]][[2]]),0,LFM[[1]][[2]])

L_MV  <- ifelse(is.na(LFM[[1]][[3]]),0,LFM[[1]][[3]])

L_HV  <- ifelse(is.na(LFM[[1]][[4]]),0,LFM[[1]][[4]])

L_TMV  <- ifelse(is.na(LFM[[1]][[5]]),0,LFM[[1]][[5]])

L_THV <- ifelse(is.na(LFM[[1]][[6]]),0,LFM[[1]][[6]])
```

```
mu_ave<-ifelse(V_div==1,
                mu__ave+mu_LV,ifelse(V_div==2,
                   mu__ave+mu_MV,ifelse(V_div==3,
                      mu__ave+mu_HV,0)))

mu_T<-ifelse(V_div==1,
                mu__T,ifelse(
                  V_div==2,mu__T+mu_TMV,ifelse(V_div==3,
                      mu__T+mu_THV,0)))


L_ave<-ifelse(V_div==1,
              L__ave,ifelse(V_div==2,
                L__ave+L_MV,ifelse(V_div==3
                   ,L__ave+L_HV,0)))

L_T<-ifelse(V_div==1,
            L__T,ifelse(V_div==2,
               L__T+L_TMV,ifelse(V_div==3,
                  L__T+L_THV,0)))



FF_Modle_mu<-mu_ave*Fn+mu_T*Fn*T

FF_Modle_L<-L_ave+L_T*T

FF_Modle<-ifelse(FF_Modle_mu<FF_Modle_L,
                 FF_Modle_mu,FF_Modle_L)

FF_Error<-sum((FF_Modle-Ff)*(FF_Modle-Ff)*subset)/
                (length(subset)-n)

F_intersection<-((L_ave+L_T*T)/(mu_ave+mu_T*T))

w<-pnorm(Fn,F_intersection,1/(3*X_spread),TRUE,FALSE)

FF_Error_Prev<-c() FF_Error_Prev<-FF_Error

"for loop" i=0 while(i<ni) {

#This computes the predicted coefficient of
```

```
#friction for each
#point.

mu_p<-mu_ave+mu_T*T

#this computes the perpendicular distance
#between the theoretical

#coeffecent line and the point. dis_mu<-(Fn*mu_p-Ff)/
                                (1+mu_p^2)^.5

#This calculates the percent colomb Friction

Coulomb_per<-ifelse(dis_mu<0,1,1-(abs(dis_mu)/
                    max(dis_mu))^2)

#This calculates the coulomb Membership Function

Coulomb_MF<-pnorm(Coulomb_per,mean_mu,1/
                    (3*spread_mu),TRUE,FALSE)

#"LM" # This creates a linear model of the data.

CM<-lm(Ff~(T*V_factor):Fn+Fn-1,weight=
                ((1-w)*Coulomb_MF*subset))

#Stores the results for next iteration
#Stores the results for
#next iteration

mu__ave<- ifelse(is.na(CM[[1]][[1]]),0,CM[[1]][[1]])

mu__T  <- ifelse(is.na(CM[[1]][[2]]),0,CM[[1]][[2]])

mu_LV  <- ifelse(is.na(CM[[1]][[3]]),0,CM[[1]][[3]])

mu_MV  <- ifelse(is.na(CM[[1]][[4]]),0,CM[[1]][[4]])

mu_HV  <- ifelse(is.na(CM[[1]][[5]]),0,CM[[1]][[5]])

mu_TMV <- ifelse(is.na(CM[[1]][[6]]),0,CM[[1]][[6]])

mu_THV <- ifelse(is.na(CM[[1]][[7]]),0,CM[[1]][[7]])
```

```
mu_ave<-ifelse(V_div==1,
                mu__ave+mu_LV,ifelse(V_div==2,
                    mu__ave+mu_MV,ifelse(V_div==3,
                        mu__ave+mu_HV,0)))

mu_T<-ifelse(V_div==1,
             mu__T,ifelse(V_div==2,
                mu__T+mu_TMV,ifelse(V_div==3,
                    mu__T+mu_THV,0)))

#this computes the predicted Limiting force
#for each data point.

L_p<-L_ave+L_T*T

#Computes the distance between the Theoretical
#Line and the
point.

dis_L<- (L_p-Ff)

#Computes the Percent Limiting Force

Limiting_Force_per<-ifelse(dis_L<0,1,1-(abs(dis_L)/L_p)^2)

#Converts the percentage to Membership function

LimitingForce_MF<-pnorm(Limiting_Force_per,mean_L,1/
                            (3*spread_L),
                            TRUE,FALSE)


#Creates a Limiting Force Linear model

LFM<-lm(Ff~(T+V_factor+T:V_factor),
                weight=(w*LimitingForce_MF*subset))

#Stores results for next iteration

L__ave<- ifelse(is.na(LFM[[1]][[1]]),0,LFM[[1]][[1]])

L__T  <- ifelse(is.na(LFM[[1]][[2]]),0,LFM[[1]][[2]])
```

```
L_MV  <- ifelse(is.na(LFM[[1]][[3]]),0,LFM[[1]][[3]])

L_HV  <- ifelse(is.na(LFM[[1]][[4]]),0,LFM[[1]][[4]])

L_TMV  <- ifelse(is.na(LFM[[1]][[5]]),0,LFM[[1]][[5]])

L_THV <- ifelse(is.na(LFM[[1]][[6]]),0,LFM[[1]][[6]])



L_ave<-ifelse(V_div==1,L__ave,
               ifelse(V_div==2,L__ave+L_MV,ifelse(V_div==3,
                   L__ave+L_HV,0)))

L_T<-ifelse(V_div==1,L__T,
            ifelse(V_div==2,L__T+L_TMV,ifelse(V_div==3,
                L__T+L_THV,0)))

sum(F_intersection)/length(F_intersection)

F_intersection<-((L_ave+L_T*T)/(mu_ave+mu_T*T))

w<-pnorm(Fn,F_intersection,1/(3*X_spread),TRUE,FALSE)


FF_Modle_mu<-mu_ave*Fn+mu_T*Fn*T

FF_Modle_L<-L_ave+L_T*T

FF_Modle<-ifelse(((FF_Modle_mu-Ff)*(FF_Modle_mu-Ff))<
                   ((FF_Modle_L-Ff)*(FF_Modle_L-Ff)),
                   FF_Modle_mu,FF_Modle_L)

FF_Error<-sum((FF_Modle-Ff)*(FF_Modle-Ff)*subset)/
                           (length(subset)-n)


FF_Error_Alternate_Set<-(sum((FF_Modle-Ff)*
                       (FF_Modle-Ff)*(1-subset))/n)

FF_Error_Current<-FF_Error

#print(i)
```

```
i=i+1

ifinal=i

de=abs(FF_Error_Prev-FF_Error_Current)

ifelse(de<1,flag<-1,flag<-0)

ifelse(de<.1,flag2<-1,flag2<-0)

ifelse(de<.01,flag3<-1,flag3<-0)

ifelse(de<.001,i<-ni,1)

FF_Error_Prev<-FF_Error_Current


}

CMA<-anova(CM)

LFMA<-anova(LFM)

DOF_Fn_mu<-CMA[[1]][[1]]

DOF_TFn_mu<-CMA[[1]][[2]]

DOF_VFn_mu<-CMA[[1]][[3]]

DOF_TVFn_mu<-CMA[[1]][[4]]

DOF_R_mu<-CMA[[1]][[5]]

P_Fn_mu<-CMA[[5]][[1]]

P_TFn_mu<-CMA[[5]][[2]]

P_VFn_mu<-CMA[[5]][[3]]

P_TVFn_mu<-CMA[[5]][[4]]

Msq_Fn_mu<-CMA[[3]][[1]]

Msq_TFn_mu<-CMA[[3]][[2]]
```

```
Msq_VFn_mu<-CMA[[3]][[3]]

Msq_TVFn_mu<-CMA[[3]][[4]]

Msq_R_mu<-CMA[[3]][[5]]


DOF_T_L<-LFMA[[1]][[1]]

DOF_V_L<-LFMA[[1]][[2]]

DOF_TV_L<-LFMA[[1]][[3]]

DOF_R_L<-LFMA[[1]][[4]]

P_T_L<-LFMA[[5]][[1]]

P_V_L<-LFMA[[5]][[2]]

P_TV_L<-LFMA[[5]][[3]]

Msq_T_L<-LFMA[[3]][[1]]

Msq_V_L<-LFMA[[3]][[2]]

Msq_TV_L<-LFMA[[3]][[3]]

Msq_R_L<-LFMA[[3]][[4]]



#----------------

plot(Ff~Fn) points(Ff~Fn, col="red")
points((FF_Modle_L)~Fn, col =
"blue", type = "p")
points((FF_Modle_mu-1)~Fn, col = "red", type =
"p")
```

```
F_intersection<-((L_ave+L_T*T)/(mu_ave+mu_T*T))


#------------------

Betas<-c(flag,flag2,flag3,ifinal,mu__ave,mu__T,mu_LV,
            mu_MV,mu_HV,mu_TMV,mu_THV,L__ave,L__T,L_MV,
            L_HV,L_TMV,L_THV,FF_Error,FF_Error_Current,
            DOF_Fn_mu,DOF_TFn_mu,DOF_VFn_mu,DOF_TVFn_mu,
            DOF_R_mu,P_Fn_mu,P_TFn_mu,P_VFn_mu,P_TVFn_mu,
            Msq_Fn_mu,Msq_TFn_mu,Msq_VFn_mu,Msq_TVFn_mu,
            Msq_R_mu,DOF_T_L,DOF_V_L,DOF_TV_L,DOF_R_L,
            P_T_L,P_V_L,P_TV_L,Msq_T_L,Msq_V_L,Msq_TV_L,
            Msq_R_L)

Matrix[ii,]<-Betas


print("number of loops") print(i)
print("number of iterations")
print(ii) ii=ii+1


}

BetasNames<-c("flag_1","flag_.1","flag_.01",
              "number_of_iterations","mu__ave",
              "mu__T","mu_LV","mu_MV","mu_HV",
              "mu_TMV","mu_THV","L__ave","L__T",
              "L_MV","L_HV","L_TMV","L_THV",
              "FF_Error","FF_Error_Current",
              "DOF_Fn_mu","DOF_TFn_mu",
              "DOF_VFn_mu","DOF_TVFn_mu",
              "DOF_R_mu","P_Fn_mu","P_TFn_mu",
              "P_VFn_mu","P_TVFn_mu","Msq_Fn_mu",
              "Msq_TFn_mu","Msq_VFn_mu","Msq_TVFn_mu",
              "Msq_R_mu","DOF_T_L","DOF_V_L","DOF_TV_L",
              "DOF_R_L","P_T_L","P_V_L","P_TV_L",
              "Msq_T_L","Msq_V_L","Msq_TV_L","Msq_R_L")

save(Matrix,BetasNames, file = filename)

return(Matrix)
```

```
}
```

Appendix C: Membership Function Regression Example

C.1 Membership Function Algorithm Example

This is an example of the membership function algorithm in a two dimensional case. The models used for this example do not depend on temperature and velocity. These models are shown in Equations C.1 through C.3. The coefficient of friction for the Coulomb model is β_{11}. The plastic shear deformation frictional force is a constat, β_{21}.

$$F_c = \beta_{11} \cdot F_n \tag{C.1}$$

$$F_p = \beta_{21} \tag{C.2}$$

$$F_f = min(F_c, F_p) \tag{C.3}$$

For explanation purposes, only one point will be shown. However, this algorithm requires other data points to work. These data points are not shown. All the calculations to determine the membership function for that data point will be shown. The calculations for determining the coefficients will not be shown.

The point that is chosen has a normal force of 300 and a frictional force of 200. In addition, arbitrarily values are chosen. Both the Coulomb and plastic shear deformation friction MV and SV are 40 and 0.025 respectively. The intersection SV is 0.025.

Initially, this point and all other points in the data set are given a membership function value of one for both coulomb and plastic shear deformation friction membership functions. These membership function values are used as weights in the regression. Initial coefficients to the model are determined. The coefficient for the coulomb model, β_{11}, is 0.5. The coefficient for the plastic shear deformation model, β_{21}, is 100.

C.1.1 First Iteration

The initial guesses of the coefficients are used in this iteration. The first step of the first iteration is to determine the perpendicular distances are determined. The perpendicular distance and intermediate membership function calculations are shown graphically in Figures C.1 through C.3. These figures can be refered to throughout the following discussion of iteration one.

The first step is to find the perpendicular distance from the data point to the model lines. Using Equation 3.10 the perpendicular distance between the point and

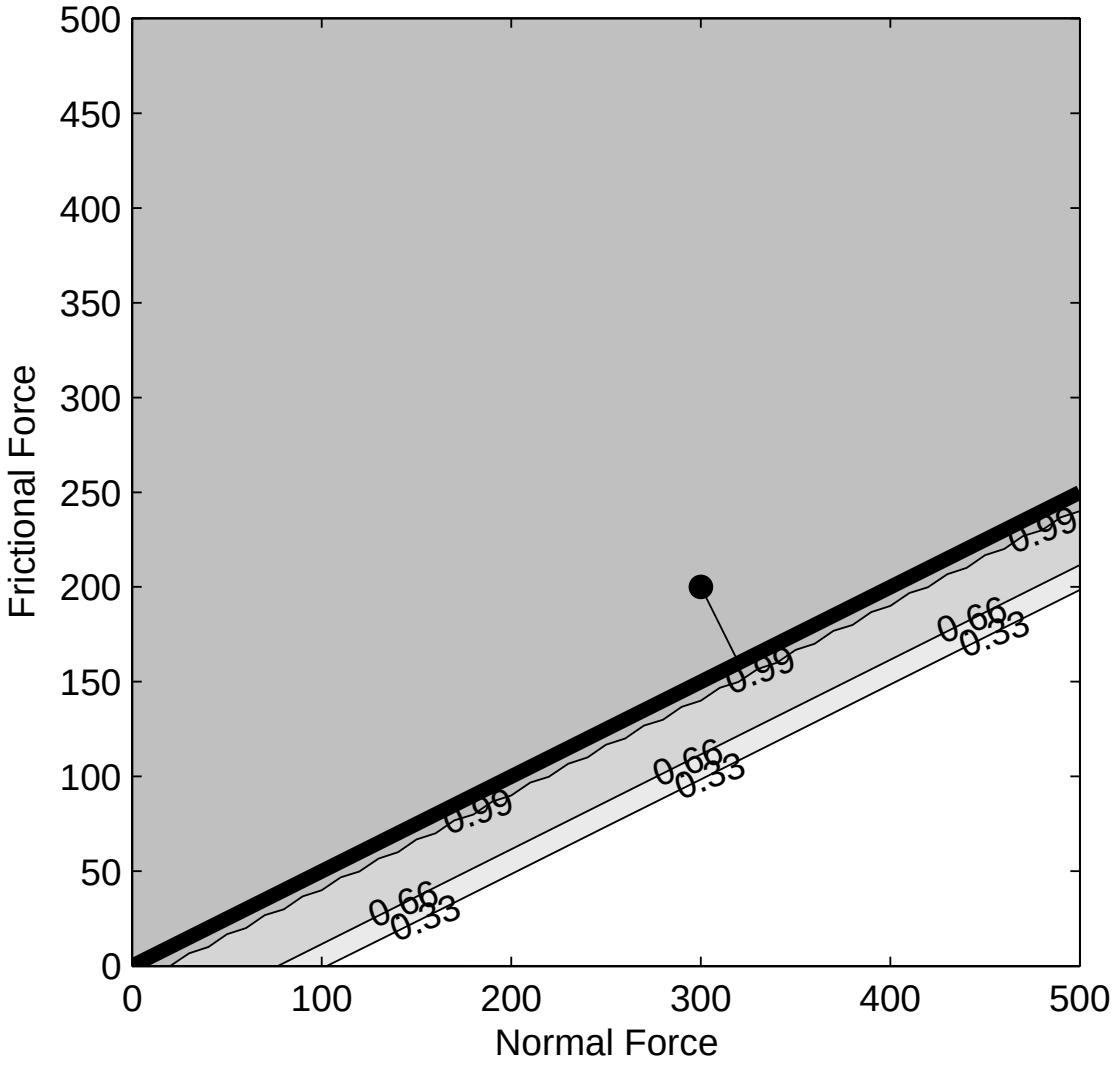

Figure C.1: Coulomb intermediate membership function for iteration one.

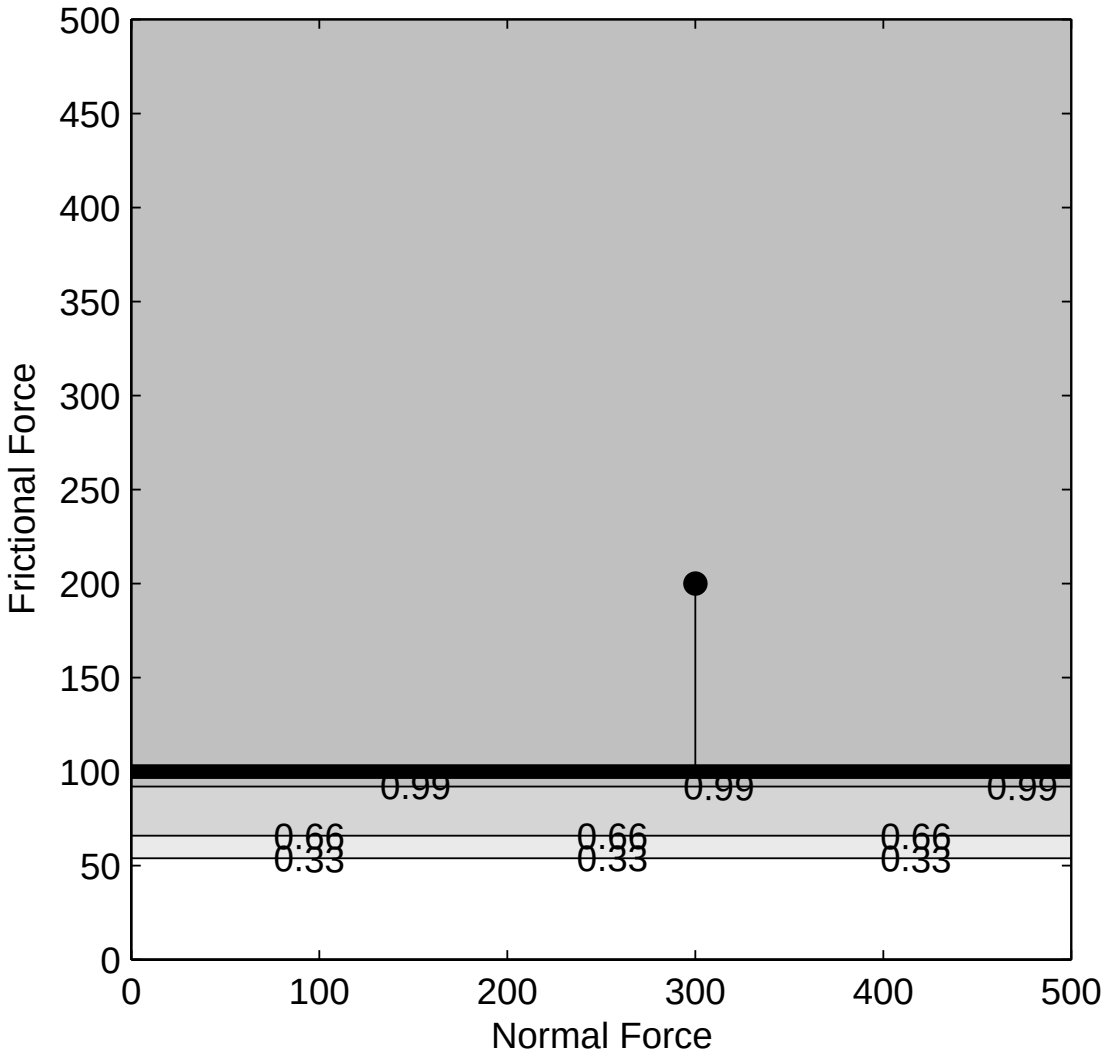

Figure C.2. Plastic shear deformation friction intermediate membership function for iteration one.

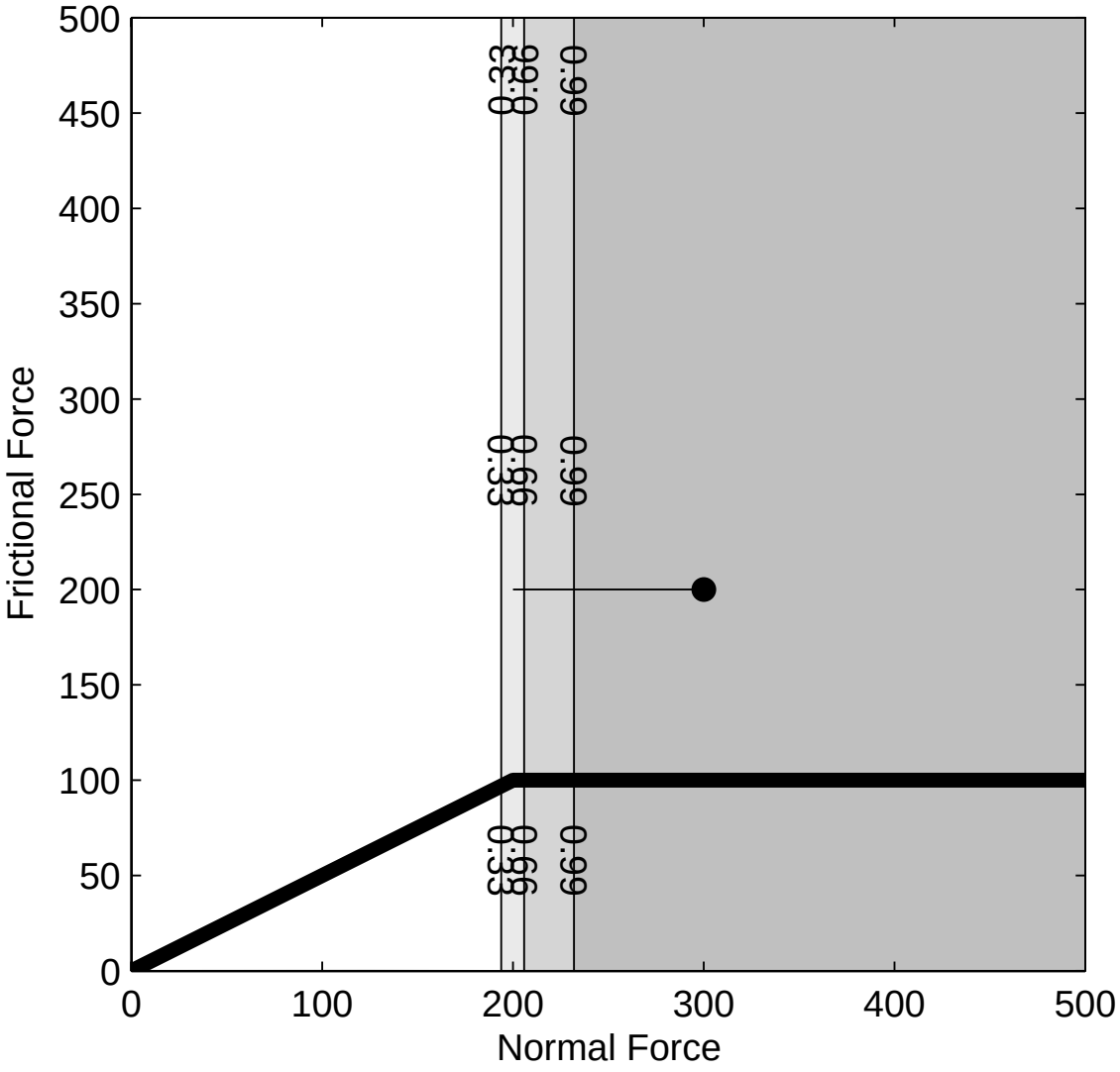

Figure C.3: Intersection intermediate membership function for iteration one.

the coulomb line is calculated as shown in equation C.6.

$$\perp_{distF_c} = \frac{x_n \cdot (\mu|_{X_n}) - y_n}{(1 + (\mu|_{X_n})^2)^{\frac{1}{2}}} \tag{C.4}$$

$$= \frac{300 \cdot 0.5 - 200}{(1 + (0.5)^2)^{\frac{1}{2}}} \tag{C.5}$$

$$= -44.721 \tag{C.6}$$

Likewise, the distance from the point to the plastic shear deformation line is calculated using Equation 3.12 shown in Equation C.9.

$$\perp_{distF_p} = F_p|_{X_n} - y_n \tag{C.7}$$

$$= 100 - 200 \tag{C.8}$$

$$= -100 \tag{C.9}$$

The distance from the point to the intersection of the two models is not calculated at this point. This calculation is performed inherently in the intersection intermediate membership function step. However the intersection force is calculated by Equation C.12

$$F_I = \frac{\beta_{21}}{\beta_{11}} \tag{C.10}$$

$$= \frac{100}{0.5} \tag{C.11}$$

$$= 200 \tag{C.12}$$

The second step is that the intermediate membership functions are calculated. Each of the intermediate normalization functions, Equations 3.15 to 3.17, are calculated as shown in Equations C.15 to C.21.

$$MF_{cI} = 1 - \phi(\perp_{distF_c i}, MV_{F_c}, \frac{1}{3 \cdot SV_{F_c}}) \tag{C.13}$$

$$= 1 - \phi(-44.721, 40, \frac{1}{3 \cdot 0.025}) \tag{C.14}$$

$$\approx 1 \tag{C.15}$$

$$MF_{pI} = 1 - \phi(\perp_{distF_p i}, MV_{F_p}, \frac{1}{3 \cdot SV_{F_p}}) \tag{C.16}$$

$$= 1 - \phi(-100, 40, \frac{1}{3 \cdot 0.025}) \tag{C.17}$$

$$\approx 1 \tag{C.18}$$

$$MF_{II} = \phi(x_n, F_I, \frac{1}{3 \cdot SV}) \tag{C.19}$$

$$= = \phi(300, 200, \frac{1}{3 \cdot 0.025}) \tag{C.20}$$

$$\approx 1 \tag{C.21}$$

The third step is to calculate the coulomb and plastic shear deformation friction membership functions. These equations are shown in Equations C.24 and C.27.

$$\begin{aligned} MF_c &= (MF_{cI}) \cdot (1 - MF_{II}) && \text{(C.22)} \\ &= 1 \cdot (1 - 1) && \text{(C.23)} \\ &\approx 0 && \text{(C.24)} \end{aligned}$$

$$\begin{aligned} MF_p &= (MF_{pI}) \cdot (MF_{II}) && \text{(C.25)} \\ &= 1 \cdot 1 && \text{(C.26)} \\ &\approx 1 && \text{(C.27)} \end{aligned}$$

These calculations are shown in Figures C.4 and C.5. According to the membership function calculations this data point belongs mostly to the plastic shear deformation friction set. This data point does not belong to the Coulomb friction set.

The final step for this iteration is to use these membership function values for each data point as weights in the regression calculation.

C.1.2 Second Iteration

The coefficients from the first iteration regression are used for the second iteration. The coefficient of friction, β_{11} is 0.75. The plastic shear deformation friction coefficient β_{21} is 250.

The perpendicular distance and intermediate membership function calculations are shown graphically in Figures C.6 through C.8. These figures can be used throughout the following discussion for iteration two.

The first step is to find the perpendicular distance from the data point to the model lines. Using Equation 3.10 the perpendicular distance between the point and the Coulomb model line is calculated as shown in equation C.30.

$$\begin{aligned} \perp_{distF_c} &= \frac{x_n \cdot (\mu|_{X_n}) - y_n}{(1 + (\mu|_{X_n})^2)^{\frac{1}{2}}} && \text{(C.28)} \\ &= \frac{300 \cdot 0.75 - 200}{(1 + (0.75)^2)^{\frac{1}{2}}} && \text{(C.29)} \\ &= 20 && \text{(C.30)} \end{aligned}$$

Likewise, the distance from the point to the plastic shear deformation line is calculated using Equation 3.12 shown in Equation C.33

$$\begin{aligned} \perp_{distF_p} &= F_p|_{X_n} - y_n && \text{(C.31)} \\ &= 250 - 200 && \text{(C.32)} \\ &= 50 && \text{(C.33)} \end{aligned}$$

The distance from the point to the intersection of the two models is not calculated at this point. This calculation is performed inherently in the intersection intermediate

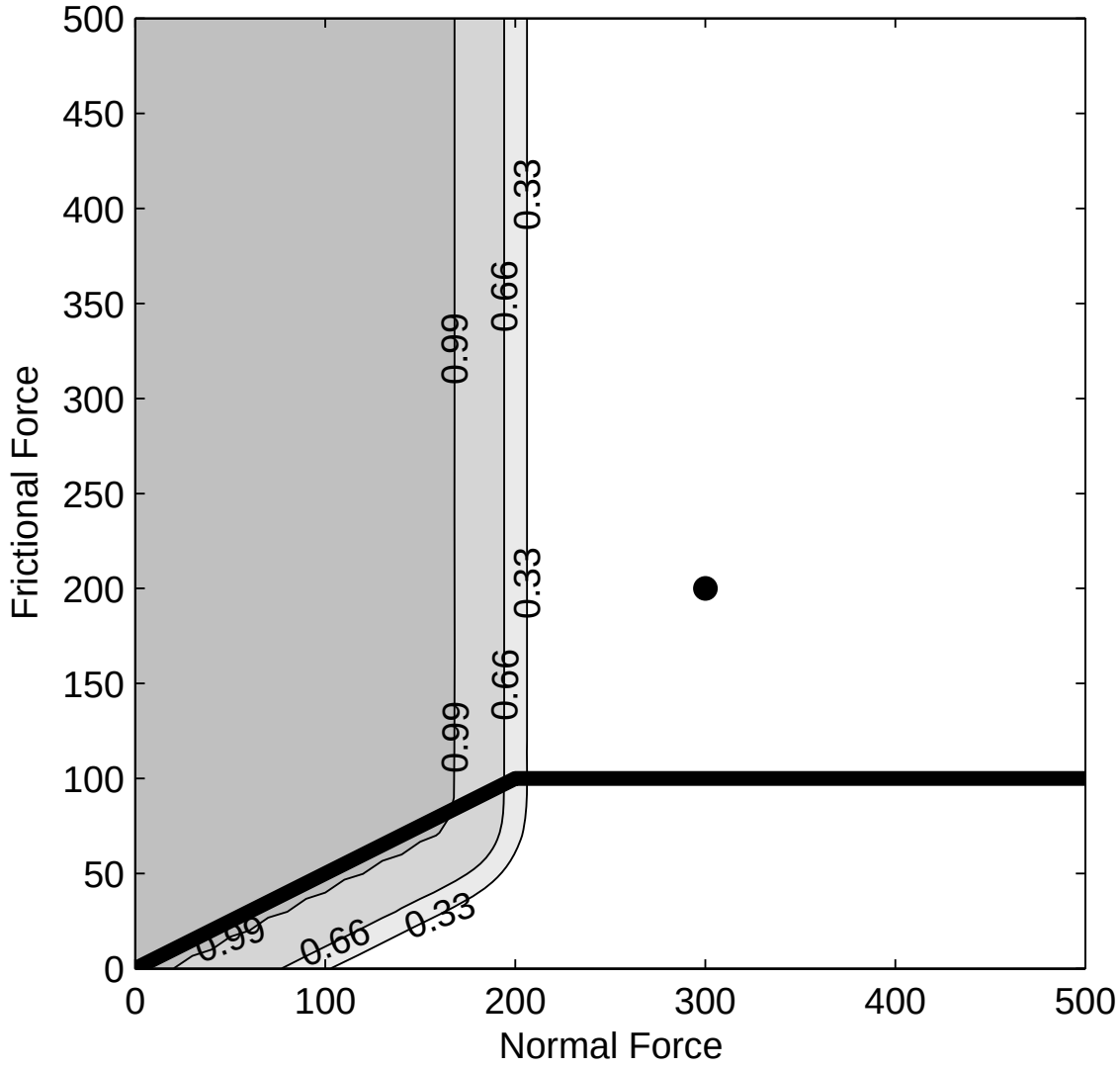

Figure C.4: Coulomb intermediate membership function for iteration one.

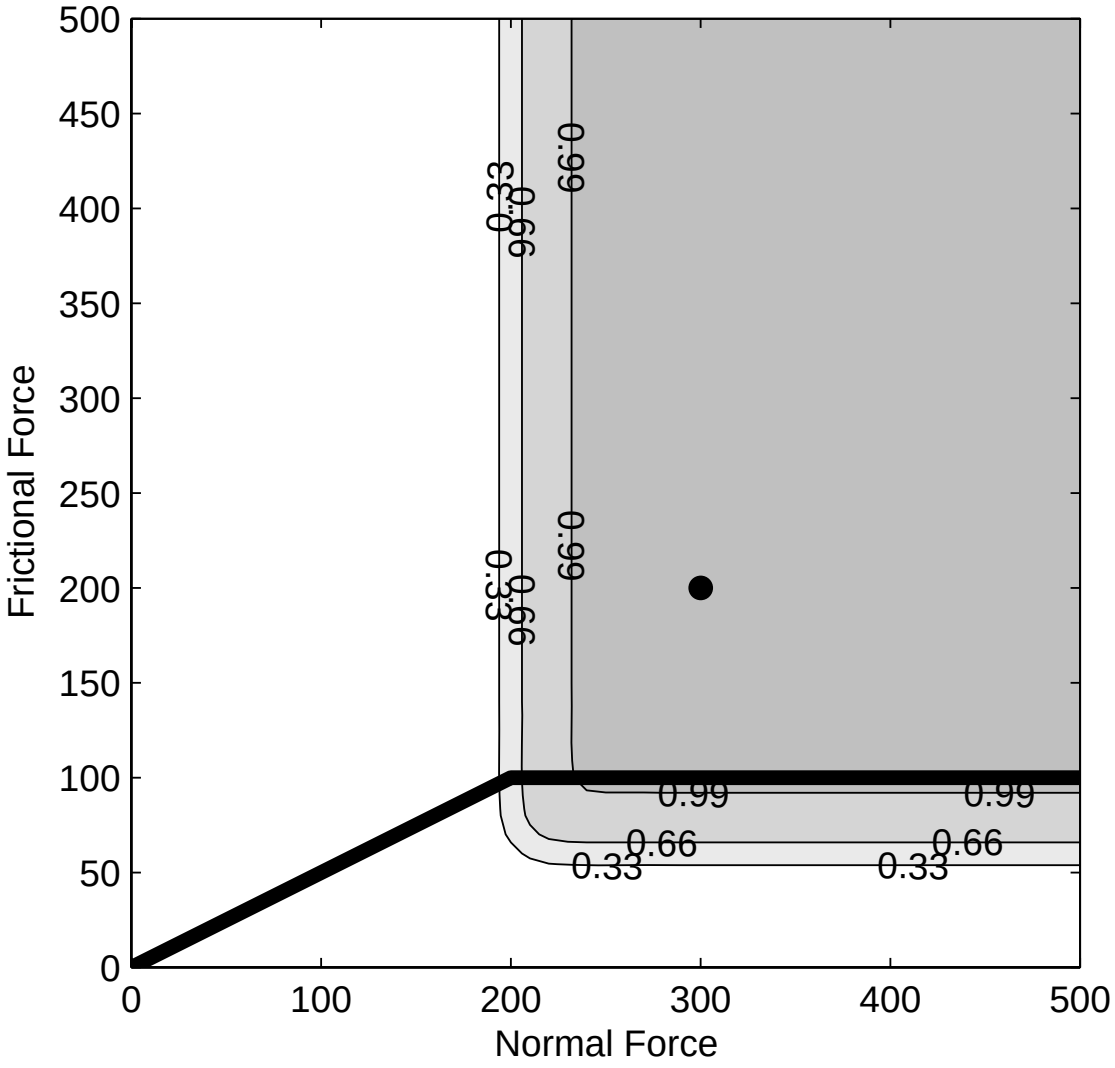

Figure C.5: Plastic shear deformation membership function for iteration one.

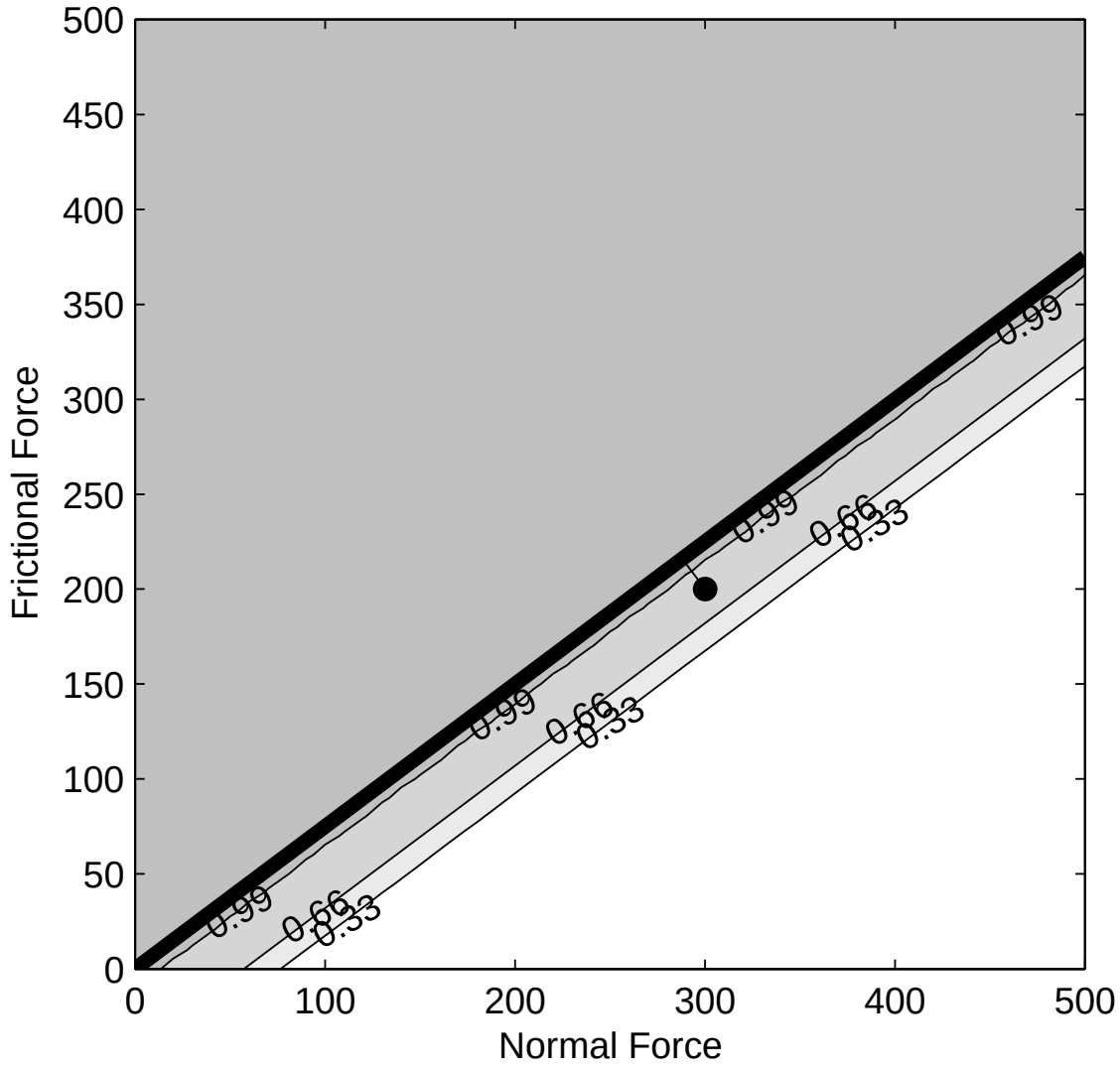

Figure C.6: Coulomb intermediate membership function for iteration twp.

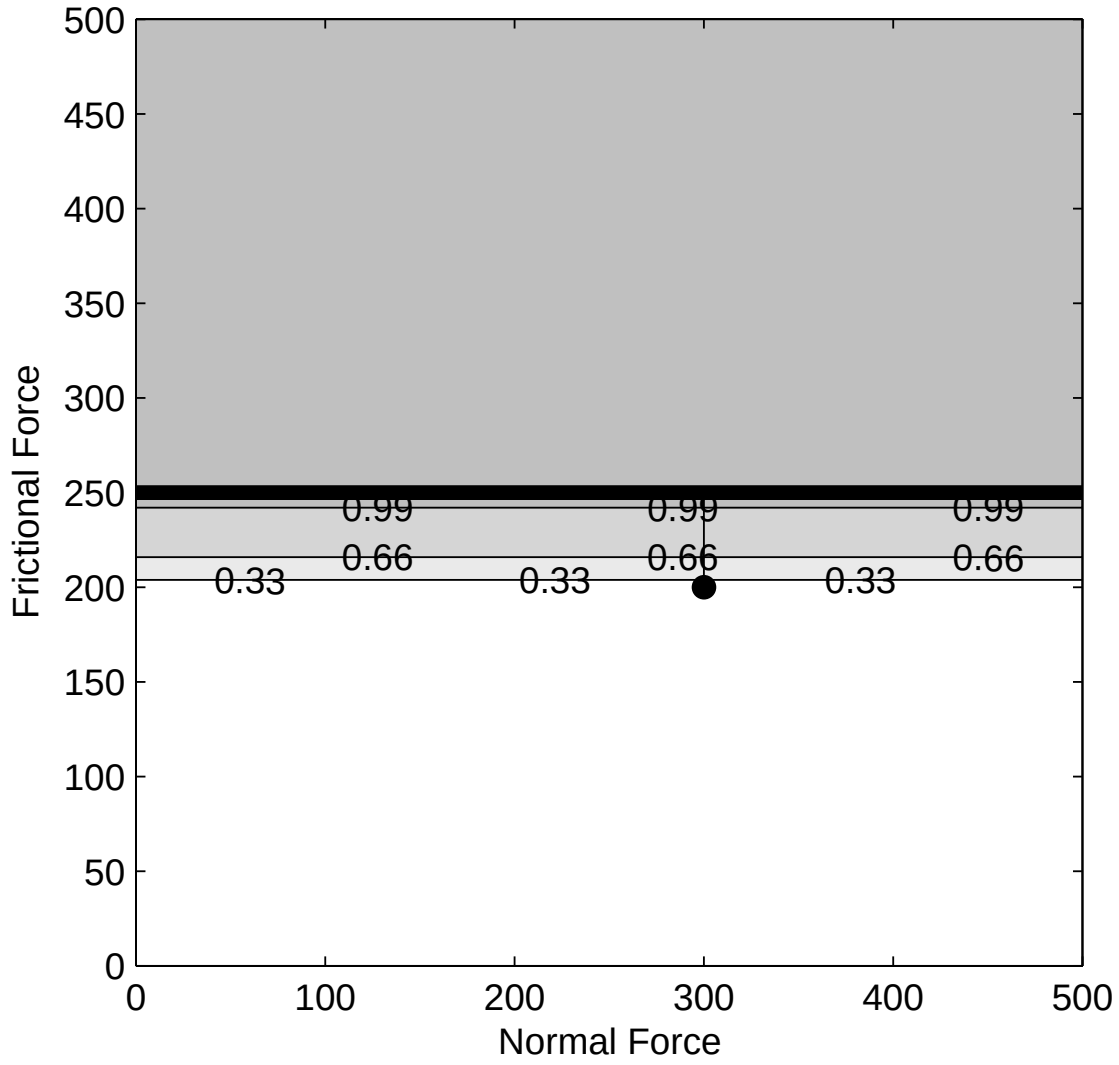

Figure C.7. Plastic shear deformation friction intermediate membership function for iteration two.

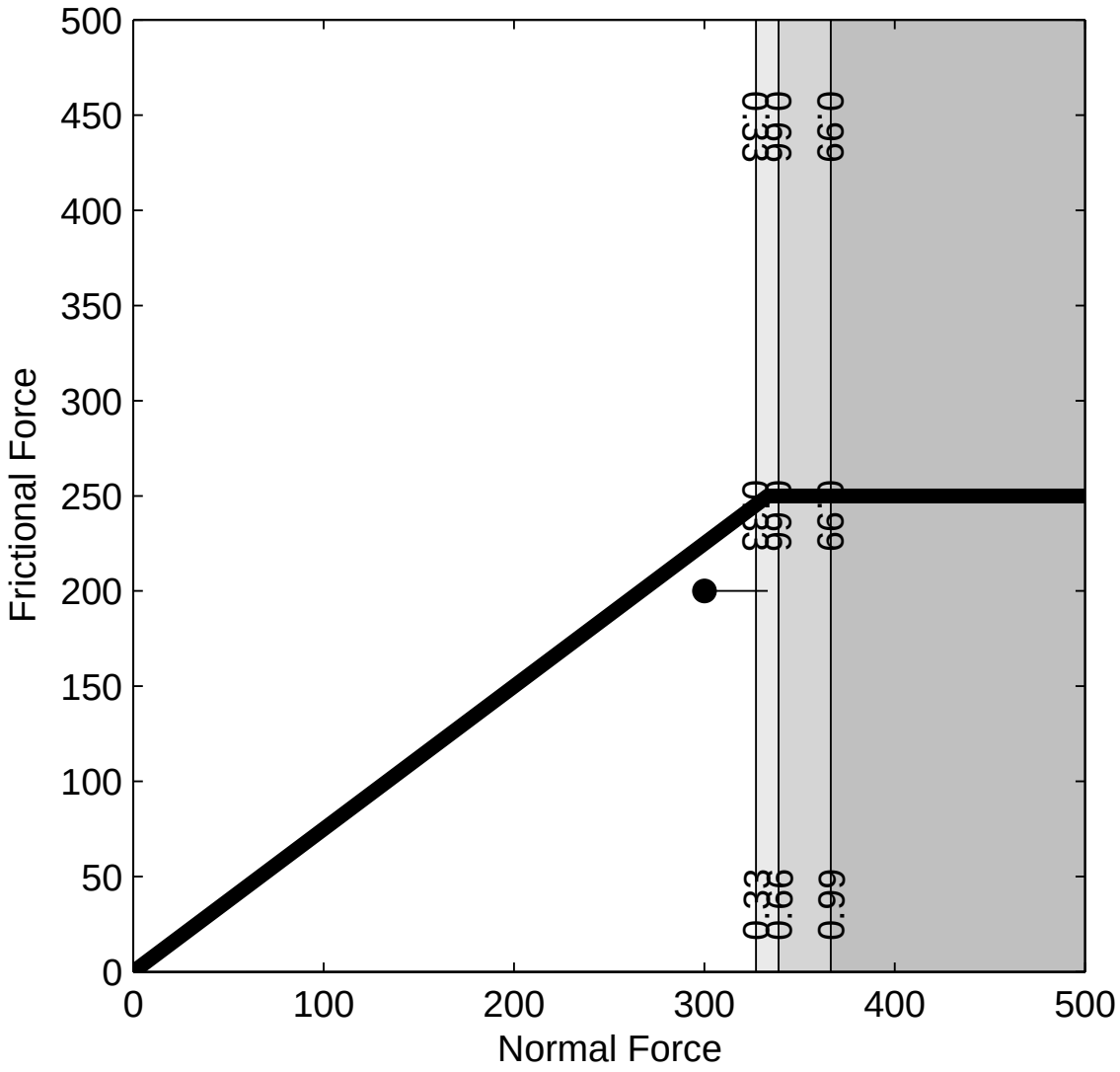

Figure C.8: Coulomb intermediate membership function for iteration two.

membership function step. The intersection force is calculated by Equation C.36.

$$F_I = \frac{\beta_{21}}{\beta_{11}} \tag{C.34}$$

$$= \frac{250}{0.75} \tag{C.35}$$

$$= 333.33 \tag{C.36}$$

The second step is to calculate the intermediate membership functions are calculated. Each of the intermediate membership functions, Equations **??** to 3.17, are calculated as shown in Equations C.39 to C.45.

$$MF_{cI} = 1 - \phi(\perp_{distF_ci}, MV_{F_c}, \frac{1}{3 \cdot SV_{F_c}}) \tag{C.37}$$

$$= 1 - \phi(20, 40, \frac{1}{3 \cdot 0.025}) \tag{C.38}$$

$$\approx 0.93 \tag{C.39}$$

$$MF_{pI} = 1 - \phi(\perp_{distF_pi}, MV_{F_p}, \frac{1}{3 \cdot SV_{F_p}}) \tag{C.40}$$

$$= 1 - \phi(50, 40, \frac{1}{3 \cdot 0.025}) \tag{C.41}$$

$$\approx 0.23 \tag{C.42}$$

$$MF_{II} = \phi(x_n, F_I, \frac{1}{3 \cdot SV}) \tag{C.43}$$

$$= = \phi(300, 333.33, \frac{1}{3 \cdot 0.025}) \tag{C.44}$$

$$\approx 0.0062 \tag{C.45}$$

The third step is to calculate the coulomb and plastic shear deformation friction membership functions and are shown in Equations C.48 and C.51.

$$MF_c = (MF_{cI}) \cdot (1 - MF_{II}) \tag{C.46}$$

$$= 0.93 \cdot (1 - 0.0062) \tag{C.47}$$

$$\approx 0.92 \tag{C.48}$$

$$MF_p = (MF_{pI}) \cdot (MF_{II}) \tag{C.49}$$

$$= 0.23 \cdot 0.0062 \tag{C.50}$$

$$\approx 0.0014 \tag{C.51}$$

These calculations are shown in Figure C.9 and C.10. According to the membership function calculations this data point belongs mostly to the Coulomb friction set. This data point belongs slightly to the plastic shear deformation friction set.

The final step for this iteration is to use these membership function values for each of the data points as weights in the regression calculation.

The iterations follow the same algorithm as these two iteration until the change in residual error reaches a threshold value or a maximum number of iterations is reached.

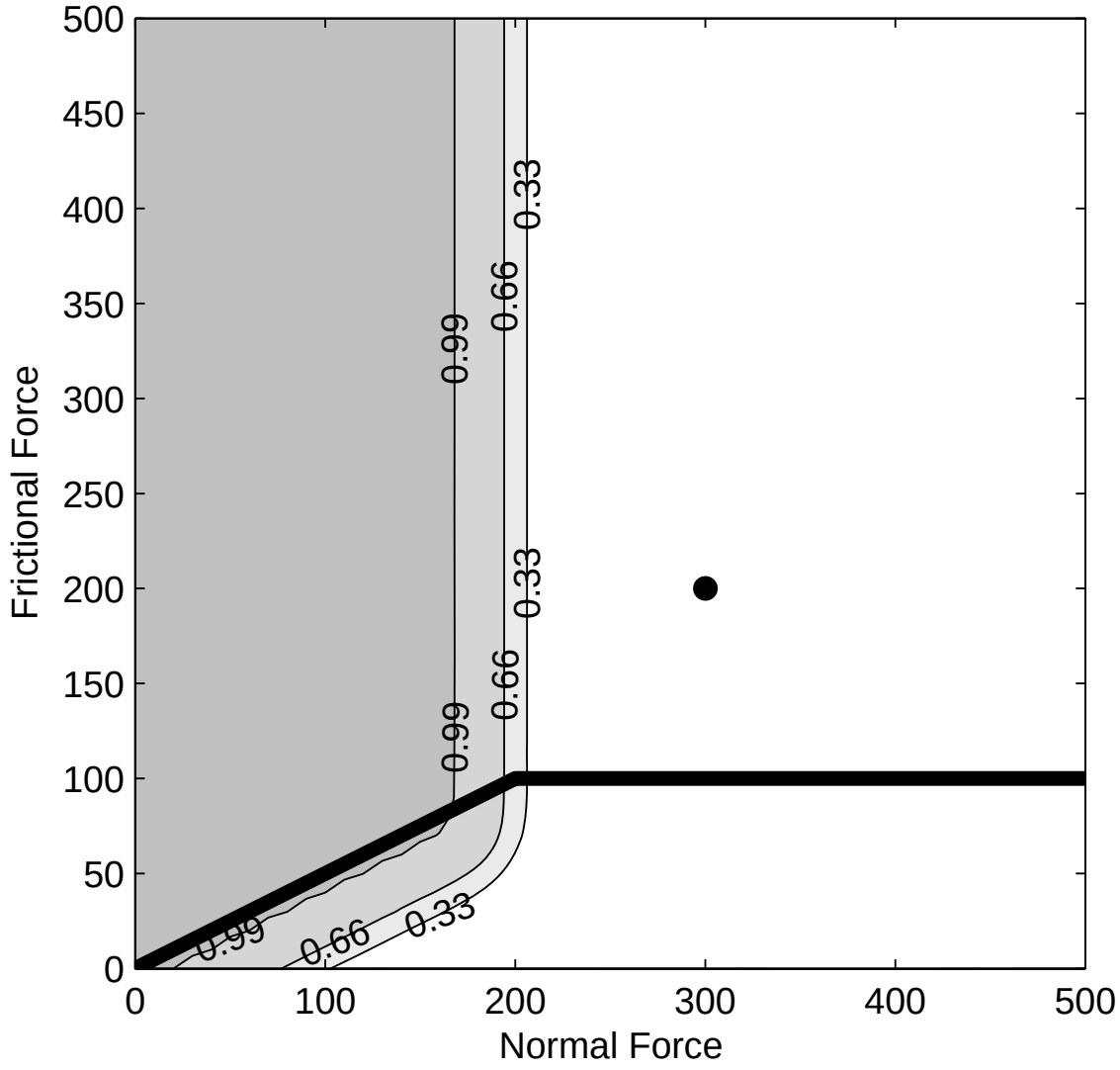

Figure C.9: Coulomb intermediate membership function for iteration two.

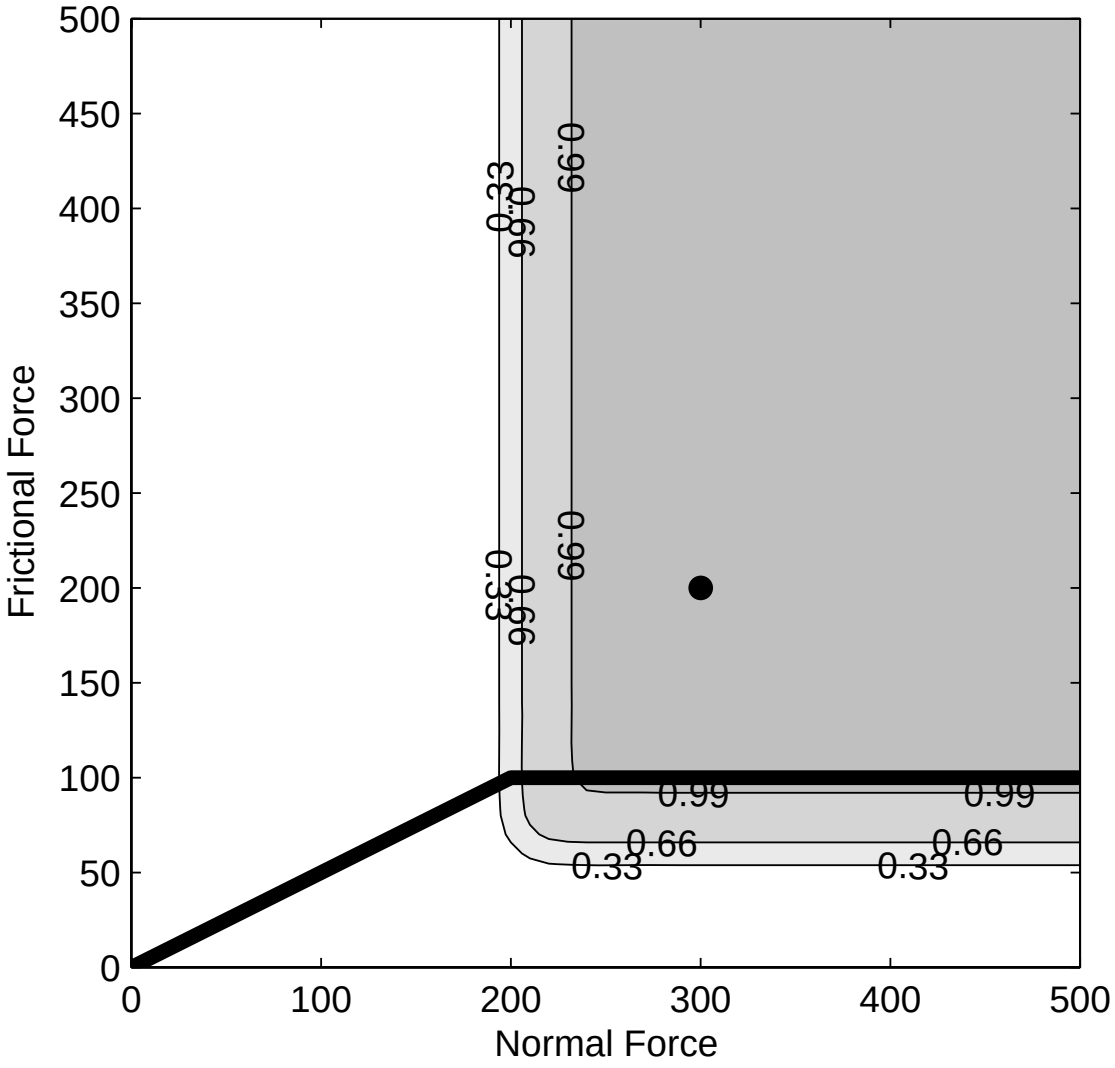

Figure C.10: Plastic shear deformation membership function for iteration two.

Appendix D: Coherence Tables

Table D.1: Top five coherent frequencies for measurement interval 1.

Frequency	Coherence	Phase
0.00	0.60	180.00
6.35	0.62	88.06
6.84	0.77	82.88
7.32	0.79	80.83
7.81	0.72	81.27

Table D.2: Top five coherent frequencies for measurement interval 2.

Frequency	Coherence	Phase
1.95	0.47	144.40
2.44	0.54	146.17
6.84	0.59	133.14
7.32	0.57	136.43
14.16	0.50	79.46

Table D.3: Top five coherent frequencies for measurement interval 12.

Frequency	Coherence	Phase
1.46	0.40	154.38
1.95	0.50	155.77
2.44	0.49	160.77
7.32	0.42	105.29
97.66	0.40	166.35

Table D.4: Top five coherent frequencies for measurement interval 15.

Frequency	Coherence	Phase
4.39	0.95	92.48
4.88	0.98	92.97
5.37	0.99	93.83
5.86	0.98	94.29
6.35	0.96	93.96

Table D.5: Top five coherent frequencies for measurement interval 20.

Frequency	Coherence	Phase
4.39	0.96	84.55
4.88	0.98	86.30
5.37	0.98	88.79
5.86	0.98	90.84
6.35	0.97	90.97

Table D.6: Top five coherent frequencies for measurement interval 23.

Frequency	Coherence	Phase
46.39	0.62	-149.62
48.34	0.63	-135.75
72.27	0.67	90.48
74.22	0.65	61.31
74.71	0.67	61.67

Table D.7: Top five coherent frequencies for measurement interval 27.

Frequency	Coherence	Phase
48.34	0.63	-152.43
48.83	0.67	-152.68
74.22	0.72	55.51
74.71	0.74	59.44
75.20	0.59	65.33

Table D.8: Top five coherent frequencies for measurement interval 29.

Frequency	Coherence	Phase
1.46	0.65	134.17
1.95	0.65	133.54
2.44	0.50	134.95
5.37	0.46	33.19
160.16	0.75	-4.87

Table D.9: Top five coherent frequencies for measurement interval 32.

Frequency	Coherence	Phase
5.37	0.84	98.97
5.86	0.94	98.96
6.35	0.96	97.18
6.84	0.96	94.93
7.32	0.93	91.66